The Henryk Niewodniczański Institute of Nuclear Physics
Polish Academy of Sciences

Thesis submitted for Degree of Doctor of Philosophy in Physics

Elastic and rheological properties of human bladder cancer cells: from single cells to spheroids

Kajangi Gnanachandran

Thesis supervisors:

Prof. dr hab. Małgorzata Lekka

Prof. Alessandro Podestà

Kraków 2022

This project has received funding from the European Union's Horizon 2020 research and Innovation programme under the H2020-MSCA-ITN-2018 Grant Agreement n. 812772.

Funded by the European Union

Phys2BioMed

கற்றது கை மண் அளவு
கல்லாதது உலகளவு

What is learned is the size of the hand
What is unlearned is the size of the world

Acknowledgements

Now that I have come to the end of my PhD, I would like to thank all the people who have always supported me, and whom I have shared this life-changing experience with.

I could not have undertaken this journey without the guidance of my supervisor Prof. Małgorzata Lekka. With her knowledge, patience, constructive criticism and encouragement she helped me complete this work successfully. I will forever be grateful for her kindness and moral support during these past three years.
I would like to extend my sincere thanks to Prof. Alessandro Podestà, who is not only my other thesis supervisor, but also the coordinator of the project *Phys2BioMed*, funded by the European Union's Horizon 2020 research and Innovation program under the Marie Skłodowska-Curie grant agreement n. 812772. I am thankful for giving me the opportunity to be part of this network.
Thanks should also go to the project manager Antonia Samorè for her care and support.

I would like to express my deepest gratitude to Dr. Arnaud Millet, Prof. Hermann Schillers and Dr. Massimo Alfano for giving me the opportunity to visit their labs, respectively in Grenoble, Münster and Milano. They made me feel part of their team, and I learned a lot from our interesting scientific discussions.

I am extremely grateful to Dr. Grażyna Pyka-Fościak and Mrs. Bożena Wójcik from the Department of Histology at Jagiellonian University, for their valuable help in the histological analysis presented in this thesis.

I would like to thank all my colleagues from IFJ PAN. Without you, it would not have been the same. Special thanks to Asia Pabijan for being the kind and helpful person she is. I was happy to share my PhD experience with Tomek and Andrzej. Thank you, guys, for all the laughs and fun we had together, and for taking me to the beautiful polish mountains. I am still waiting to go to Babia Góra together! Asia Z., Bartek, Marcin, Oliwia, Renata and Sara, thank you for your lovely company. I will miss our coffee room talks.
I had the pleasure of working with Basia only for a short time, but that was enough to create the sister bond that we have now. Thank you for your constant support and making Kraków feel like home.

I would be remiss in not mentioning the other members of the network. Laura, Constança, Javi and Massimiliano, the famous team of *Elastic cloud lab*, it was really funny to hang out with you guys and I will cherish those moments. Khaldoun, I would like to thank you for the good time spent together, and for being

the sweetest and kind-hearted person you are. Thanks to Felix for the good company, guidance, encouragement and scientific discussions we had during the network events. And Massi, I am glad to have worked with you and I also learned a lot from you. Thank you for everything.

Finally, I do not have enough words to express my gratitude to my family and my friends, who are my pillars.

My long-time friends, Arci and Greta, I can only say thanks for your continuous love and support. Then, Francesca and Veronica, thank you for always finding time for me. And, Fadwa, you are the gem that I found in Kraków and I could not have asked for a better friend and travel partner to visit Poland.

Linda, my backbone, my source of strength, I would not have taken this path without your consent, and now, I could not have come to its end without your help. Thank you.

My dearest cousins Keerthana, Priyanka, Thalir and Ladxi, thank you for all your support and for believing in me. To Saranga, Kiru, Thulasi and all my younger cousins, I hope someday I can be an inspiration to you.

Then, Gayathri, I am lucky to have you as a friend, and thank you for always encouraging and motivating me.

My beloved sister and brother in law, I know that I can always rely on you. Thank you for giving all the love and moral support I needed during these years.

My little ones, Varun and Yatra, with their smiles, always give me a reason to go on.

My mother and my grandmother are the ones who suffered the most in these years, being far away from me. But nothing was unbearable in front of my happiness. Thank you *amma* and *ammamma* for your unconditional love.

My father has always been proud of my achievements. For him, his daughters' education was the most important thing. He never failed to guide us with his wisdom and love. Thank you *appa* for respecting and supporting my decision to begin this long journey. I want to dedicate this thesis to him, hoping to make him more proud.

Last, but not least, I would like to thank uncle Karunanithy for being a huge inspiration for me.

Thank you.

List of publications

Papers:

1. **K. Gnanachandran**, S. Kedracka-Krok, J. Pabijan, M. Lekka, *Discriminating bladder cancer cells through rheological mechanomarkers at cell and spheroid levels*, Journal of Biomechanics, 144, 111346 (2022).

2. M. Berardi, **K. Gnanachandran**, J. Jiang, K. Bielawski, C.W. Visser, M. Lekka, B. I. Akca, *Dynamic Mechanical Analysis of Suspended Soft Bodies via Hydraulic Force Spectroscopy*, accepted in *Soft Matter* (2022).

3. M. Lekka, **K. Gnanachandran**, A. Kubiak, T. Zieliński, J. Zemła, *Traction force microscopy – Measuring the forces exerted by cells*, Micron, 150, 103138 (2021).

4. P.N. Osuchowska, P. Wachulak, A. Nowak-Stępniowska, A. Bartnik, **K. Gnanachandran**, M. Lekka, J. Czwartos, H. Fiedorowicz, E.A. Trafny, *Imaging of Cell Structures Using Optimized Soft X-ray Contact Microscopy*, Apllied Science, 10, 6895 (2020).

Papers that are under preparation:

1. **K. Gnanachandran**, M. Berardi, J. Pabijan, G. Pyka- Fościak, B.I. Akca, M. Lekka, *Mechanical and microrheological properties of aging spheroids*, under preparation.

2. **K. Gnanachandran** & M. Berardi, K. Bielawski, B.I. Akca, M. Lekka, *Effects of docetaxel on mechanical properties of bladder spheroids*, under preparation.

3. N. Makarova, M. Lekka, **K. Gnanachandran**, I. Sokolov, *The study of pericellular brush layer of bladder epithelial cancer cells*, under preparation.

4. **K. Gnanachandran**, E. Lorenc, A. Podestà, M. Lekka, *Mechanical properties of lung cell spheroids determined with different cantilevers*, under preparation.

5. M. Lekka, S. G. Kulkarni, S. Perez-Domingo, **K. Gnanachandran**, et al., *Standardization of AFM-based nanomechanical measurements for living cancer cells*, under preparation.

Abstract

Mechanical and microrheological properties of cells, along with the rearrangements in their actin cytoskeleton, are known to be associated with cancer progression by acquiring an important role in cancer diagnostic research. 3D cell cultures can mimic the natural environment of cells and some features of solid tumors, being widely used as potential *in vitro* models for finding novel biological features of cancer cells and anticancer drug discovery. In this study, three cell lines from different stages of bladder cancer were used to form the multicellular spheroids: HCV29 (non-malignant cancer), HT1376 (grade III carcinoma) and T24 (grade IV transitional cell carcinoma) cells. These cells are characterized by a different actin cytoskeleton, too. Their mechanical and microrheological properties are investigated using atomic force microscopy (AFM) at the nanoscale and hydraulic force spectroscopy (HFS), an innovative micropipette aspiration technique, at the macroscale. This work was mainly focused on understanding how the viscoelastic properties of cells change in 2D cultures, i.e., single cells, monolayers, and 3D spheroids. Our results from AFM show that under both compression and shear stress, HCV29 cells are stiffer than HT1376 and T24 cells, confirming that cancer cells are more deformable than non-malignant cells, regardless of the culture conditions. Then, the age-related changes in the mechanical properties of spheroids were evaluated and the results were compared to the histological analysis of spheroid cross-sections. AFM results showed that all cells become stiffer due to the aging effect and the reorganization of their cytoskeleton. It was also observed that spheroids formed by HCV29 cells were the only ones to produce extracellular matrix (ECM), which could explain the softening of these spheroids when detected by HFS. Therefore, changes in cell-cell and cell-ECM interactions during aging may greatly impact the mechanical behavior of the cells. Finally, it was checked whether the mechanical properties obtained by HFS could be used to study the effects of docetaxel (DTX), an anticancer drug, on the three types of bladder cancer spheroids. The results showed that the three cell lines behave differently and that HFS could detect the mechanical changes induced by the drug, even at the low concentrations, before the appearance of any biological marker, making HFS an advantageous method to assess the activities of anticancer compounds. Considering all the results from this work, we conclude that the mechanical and rheological properties of bladder cancer spheroids, determined by AFM and HFS, may serve as biophysical markers, not only in diagnosis but also in the treatment of this type of cancer.

Streszczenie

Właściwości mechaniczne i mikroreologiczne komórek wraz z reorganizacją cytoszkieletu aktynowego związane z progresją nowotworową stają się istotnym elementem badań nad diagnostyką nowotworów. Hodowle komórkowe 3D mogą naśladować naturalne środowisko komórek oraz niektóre cechy guzów litych, dlatego mogą być szeroko stosowane, jako potencjalne modele *in vitro* zarówno do wykrywania nowych cech biologicznych komórek nowotworowych, jak i do projektowania leków przeciwnowotworowych. W badaniach prowadzonych w ramach prezentowanej rozprawy doktorskiej, trzy linie komórkowe pochodzące z różnych stadiów rozwoju raka pęcherza moczowego zostały wykorzystane do utworzenia wielokomórkowych sferoid. Są to komórki nienowotworowej linii przewodu moczowego (HCV29) oraz komórki linii wyprowadzonych z raka pęcherza o różnym stopniu zaawansowania tj. Linie HT1376 (III stopień zaawansowania nowotworu, carcinoma) oraz T24 (IV stopień zaawansowania nowotworu, rak przejściowokomórkowy). Komórki te charakteryzują się także różną organizacją cytoszkieletu aktynowego. Pomiary własności mechanicznych i mikroreologicznych wykonano w nanoskali z wykorzystaniem mikroskopii sił atomowych (AFM, ang. *atomic force microscopy*) oraz w makroskali za pomocą hydraulicznej spektroskopia sił (HFS, ang. *hydraulic force spectroscopy*), innowacyjnej techniki aspiracji za pomocą mikropipet. Celem pracy było zrozumienie, w jaki sposób lepkosprężyste właściwości komórek zmieniają się w zależności od warunków hodowli: hodowle 2D (pojedyncze komórki, monowarstwy komórkowe) w porównaniu do 3D (sferoidy). Uzyskane wyniki z AFM pokazują, że komórki HCV29 charakteryzują się mniejszą deformowalnością niż komórki rakowe HT1376 i T24 niezależnie od kierunku działania siły odkształcającej (kompresja lub ścinanie), potwierdzając tym samym, że komórki rakowe są bardziej odkształcalne niż komórki nienowotworowe. Ta relacja jest niezależna od warunków hodowli. Następnie badano zmiany własności mechanicznych i struktury wewnętrznej (analiza histologiczna) sferoid związane z ich wiekiem. Wyniki uzyskane za pomocą AFM wykazały, że wszystkie komórki stają się sztywniejsze ze względu na efekt starzenia i reorganizację ich cytoszkieletu. Równocześnie pokazano, że sferoidy utworzone przez komórki HCV29 były jedynymi, które produkowały macierz zewnątrzkomórkową (ECM). To może wyjaśniać większą deformowalność tych sferoid w pomiarach wykonanych przez HFS. Dodatkowo zmiany w oddziaływaniach międzykomórkowych oraz na granicy komórka-ECM, zachodzące podczas starzenia, mogą mieć duży wpływ na odpowiedź mechaniczną komórek. Ostatnim elementem rozprawy

doktorskiej są badania pokazujące zmiany własności mechanicznych sferoid zachodzące pod wpływem działania docetakselu (DTX), leku przeciwnowotworowego, mierzone za pomocą HSF. Uzyskane wyniki pokazały, że pod wpływem leku sferoidy utworzone z badanych linii komórkowych zachowują się inaczej. HFS może wykorzystany w badaniach tego typu, nawet dla niskich stężeń leku, przy których nie pojawia się jakiegokolwiek marker biologiczny. Wyniki te czynią HFS korzystną metodą do oceny działania leków przeciwnowotworowych. Biorąc pod uwagę wszystkie wyniki tej pracy, można stwierdzić, że właściwości mechaniczne i reologiczne sferoid raka pęcherza moczowego mierzone zarówno przez AFM i HFS, mogą służyć jako markery biofizyczne raka, nie tylko w diagnostyce, ale także w leczeniu tego typu nowotworu.

Contents

Abbreviations

2D: Two-dimensional
3D: Three-dimensional
A549: Non-small lung cancer cells
AFM: Atomic Force Microscopy
BC: Bladder Cancer
Ctr: Control
Cyto D: Cytochalasin D
DTX: Docetaxel
ECM: Extracellular Matrix
EDTA: Ethylenediamine Tetraacetic Acid
EMEM: Eagle's Minimum Essential Medium
F-actin: Filamentous actin
FBM: Fibroblast Basal Medium
FBS: Fetal Bovine Serum
FGM: Fibroblast Growth Medium
G-actin: Globular actin
H&E: Hematoxylin and Eosin
HCV29: Non-malignant cell cancer of ureter
HFS: Hydraulic Force Spectroscopy
HT1376: Bladder carcinoma cell
MCS: Multicellular Spheroid
MIBC: Muscle Invasive Bladder Cancer
MT: Masson's Trichrome
MTOC: Microtubule Organizing Centers
NHLF: Lung fibroblasts
NMIBC: Non-Muscle Invasive Bladder Cancer
PBS: Phospahte Buffer Saline
RPMI medium: Roswell Park Memorial Institute medium
SDS: Sodium Dodecyl Sulfate
SR: Sirius red
T24: Transitional cell carcinoma
TBST: Tris-Buffered Saline Tween-20
TNM: Tumor-Node-Metastasis
TURBT: Transurethral Resection of the Bladder Tumor

Part I

Introduction

Chapter 1

Fundamentals and state of the art

1.1 Bladder cancer

Bladder cancer is one of the most diffused malignancies worldwide, occupying the 10^{th} place for the most commonly diagnosed cancer [1]. As a matter of fact, more than 550,000 patients are diagnosed yearly with bladder cancers, predominantly in developed countries. This number roughly represents 3 % of the new cancer diagnosis and 2.1 % of all cancer deaths [2]. One of the dominant risk factors for bladder cancer is smoking. In fact, in males, half of the urothelial carcinoma can be correlated to tobacco use [3].

1.1.1 The urothelium

The major lethality of bladder cancer relies on the urothelium of the bladder [4]. Indeed, about 90 % of this cancer type is derived from transitional epithelial cells (urothelial cells) that cover the bladder and the urinary tract [5].

The urothelium, also called transitional epithelium, changes its shape due to stretching. It has a cuboidal shape when relaxed and a more squamous shape when stretched [6]. The urothelium is composed of three main layers of epithelial cells: basal, intermediate and umbrella cells (figure 1.1).

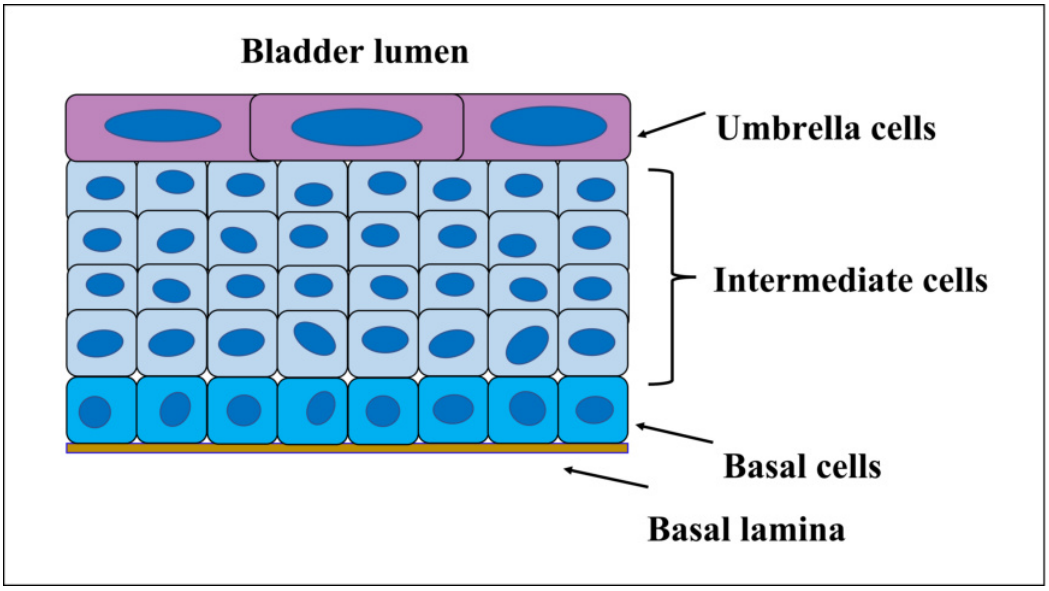

Figure 1.1: **Structure of the urothelium.** The urothelium is composed of three layers of transitional epithelia. Small basal cells are close to the basement lamina, followed by the transit amplifying cells (intermediate cells). Above these two, there is the top layer consisting of large umbrella cells.

The basal cells are attached to the basal lamina, and they are small (roughly 10 μm) epithelial stem cells characterized by a high rate of proliferation and are in charge of the renewal of the epithelium. The intermediate cells are large (approximately 10 to 25 μm in diameter) and involved in the regeneration of cells immediately after an injury or infection of the bladder. The top layer of the urothelium is composed of the umbrella cells (diameter between 25 and 250 μm), which form the barrier between the bloodstream and bladder lumen. Among the three different layers, these are the only ones fully differentiated [7].

1.1.2 Staging and grading of bladder cancer

The fundamental role of the bladder is to work as a momentary reservoir for the urine that the kidneys produce. The urine contains several metabolic waste products that are filtered by the kidneys, and the bladder should prevent them from going into the surrounding tissue and the bloodstream. It is made possible by the urothelium, a multilayer of epithelia that covers the urinary tract and functions as a permeability barrier [7]. Therefore, the urothelial cells are continuously exposed to mutagenic agents in the urine, which is the main reason behind the formation of bladder cancer [8].

There are two main categories of bladder cancers: non-muscle invasive blad-

der cancers (NMIBC) and muscle-invasive bladder cancers (MIBC). They are classified using the TNM (tumor-node-metastasis) system [9]. In this system, T stands for the size and the location of the tumor, N says if the tumor went into the lymph nodes or not, and M indicates metastasis, meaning the tumor has gone into distant sites [8]. Figure 1.2 shows a schematic illustration of the main classification of bladder cancers.

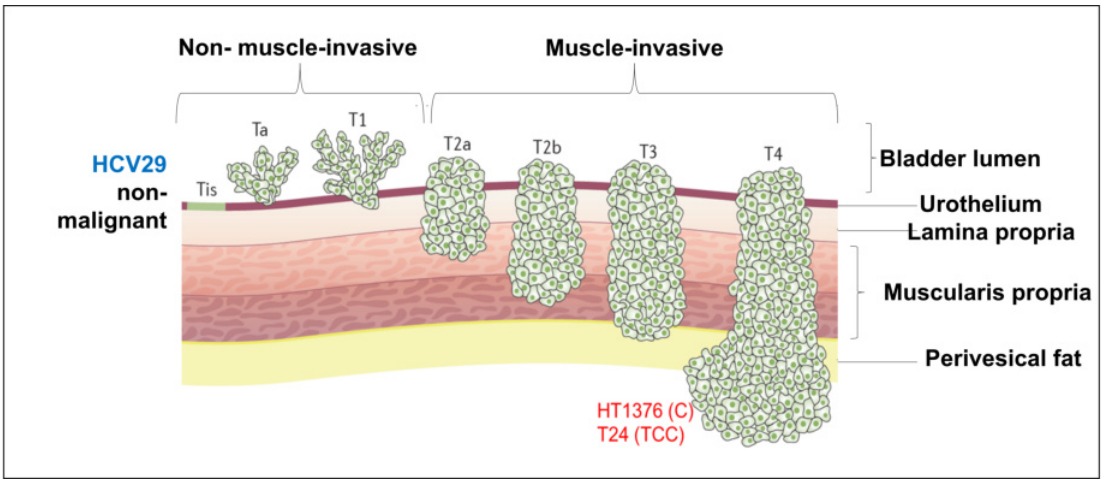

Figure 1.2: **Schematic representation of the bladder cancer stages.** The three cell lines used in this study, i.e., HCV29, HT1376 and T24 cells, are collocated in the corresponding tumor stage. C: carcinoma. TCC: transitional cell carcinoma (adapted from Sanli et al. [8]).

Tumors classified as stage Ta and T1 are non-muscle invasive cancers, which are limited to either only the urothelium (Ta) or both urothelium and *lamina propria* (T1). T2a stage tumors invade the superficial layer of the *muscularis propria*, while T2b stage tumors can go deeper into the muscle layer. T3-stage cancers go through the muscle layer towards the perivesical fat. And last, there are T4-stage tumors that go beyond the bladder wall and invade the surrounding tissues like the abdominal wall, uterus, vagina, pelvic wall, and prostate stroma.

Different bladder cancer cell lines were chosen for the thesis. HCV29, a non-malignant cell cancer of the ureter, was obtained from the non-malignant part of the irradiated, cancer-free bladder transitional epithelium of a patient suffering from bladder carcinoma [111]; HT1376 and T24 cells were collected from grade 3 tumors, representing carcinoma and transitional cell carcinoma [139], respectively. In figure 1.2, the localization of the chosen cell lines is indicated.

1.1.3 Diagnosis and treatment of bladder cancer

The general diagnostic method of bladder cancer is *haematuria*, i.e., the presence of visible blood in the urine or *microscopic haematuria* when blood is detected during urinalysis [12]. In case of suspected bladder cancer, the patient undergoes a cystoscopy, an endoscope-based examination of the bladder wall. The presence of a tumor is confirmed based on histopathological examination. Following this, transurethral resection of the bladder tumor (TURBT) is frequently applied [13]. In TURBT, either the entire tumor is removed or only a biopsy is taken for further analysis in the case of the muscle-invasive tumor.

The treatment for bladder cancer varies for NMIBC and MIBC. NMIBC can be mainly treated with TURBT [14] and/or the Bacillus Calmette-Guérin (BCG) vaccine bladder instillation [15]. However, also these treatments have their own drawbacks. TURBT leaves a high number of circulating tumor cells in the blood after the surgery, which may contribute to the dissipation of urothelial cell carcinomas to other organs and tissues. The BCG immunotherapy could produce adverse reactions due to the treatment contraindications. Despite this, these two forms of treatment give an overall 80 % success rate and are the gold standard for NMIBC cancers. Treating MIBC is much more complicated because it may even require the resection of the entire bladder, i.e., cystectomy [16]. In both cases, the treatment also involves chemotherapy [17], in which cisplatin [18] and gemcitabine [19] are commonly used. The main problem with such drugs is the resistance of cancers to their applications. Indeed, a high percentage of patients are known to acquire bladder cancer resistance, particularly after cisplatin administration, after the initial phase of the treatment [20]. The exact mechanism behind anticancer drug resistance is still unknown, meaning further studies are necessary to improve the treatment.

1.2 Cell structure and cytoskeleton

Cells are very complex systems that consist of various elements that are structurally and mechanically different [21]. In cell mechanics, the cell structure is simplified, taking into account only the main components of the cells: the plasma membrane, the nucleus, and the cytoskeleton (figure 1.3 A).

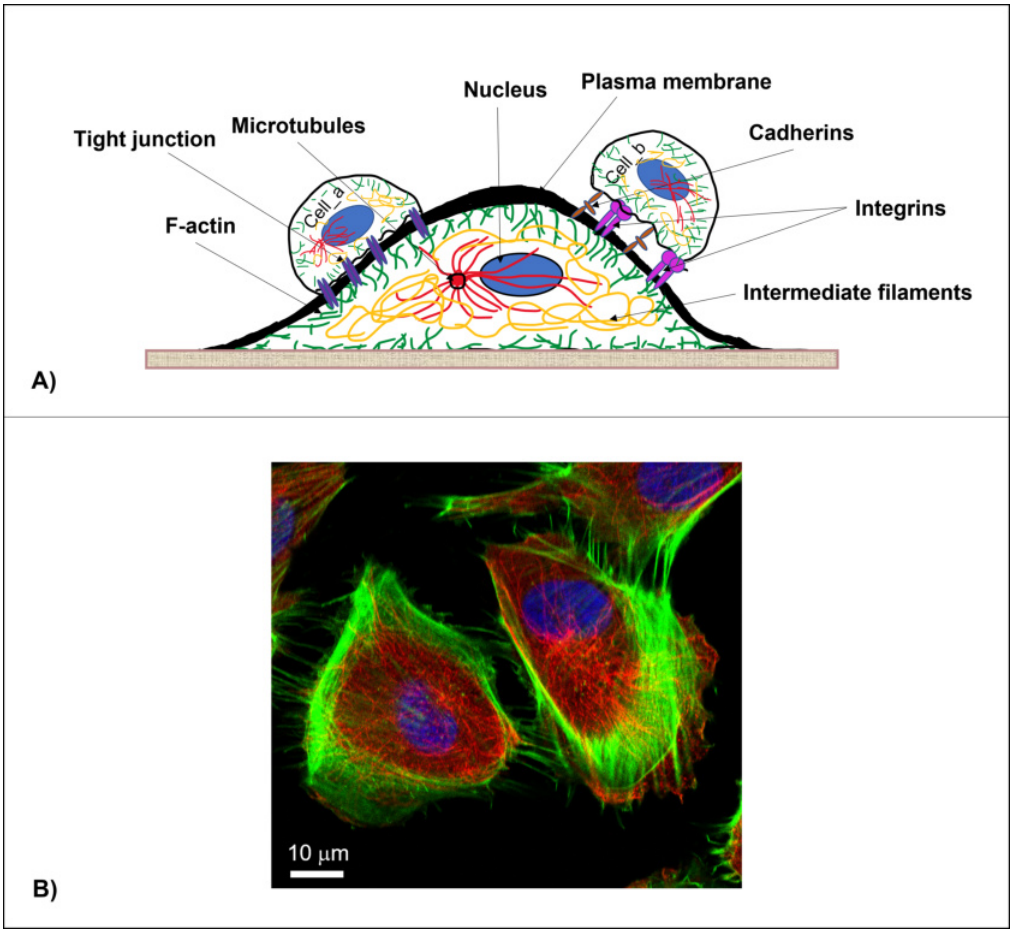

Figure 1.3: **Main components of the cell.** A) Schematic illustration of the main elements constituting the cell (cell nucleus, cytoskeleton, plasma membrane). B) Confocal image of HCV29 non-malignant cells showing the organization of actin filaments and microtubules with respect to the cell nucleus. Fluorescent staining: blue: cell nucleus (Hoechst 33342); green: actin filaments (Alexa Fluor 488); red: microtubules (anti-β-Tubulin-Cy3).

The cell membrane functions as a barrier between the external environment and the cell interior, protecting the cell from external factors [22]. It consists of a phospholipid bilayer penetrable for water and small non-polar molecules like O_2 and CO_2 [23]. Moreover, several proteins and lipids are part of the cell membrane, and they enable the formation of channels through which ions, nutrients and metabolites can be transported in and out of the cell [24].

The greater volume of the total cell is constituted by the cell nucleus, which contains genetic information in the form of chromosomes [21]. In figure 1.3 B, the nuclei of the HCV29 bladder cancer cells are stained in blue (Hoechst 33342).

The nucleus and the plasma membrane are connected to the cytoskeleton.

The cytoskeleton is the structure that supports the cell structure and stabilizes

its shape. The main elements constitute the cell cytoskeleton: actin microfilaments, intermediate filaments, and microtubules. Figure 1.3 B shows the main cytoskeletal networks in HCV29 non-malignant bladder cancer cells, where in green and red, the actin filaments and the microtubules are respectively visualized.

The actin filaments were first described in 1941 [25], and they are known to play an important role in many cellular activities, including cell division, migration and contraction [26]. A single actin filament is composed of actin α and β monomers organized in a fibrous filament consisting of polymerized actin coiled around the filament's main axis [27]. The polymerization starts with the globular actin monomers (G-actin) that polymerize into double-stranded helical filaments (F-actin). Typically, actin filaments have a diameter of 7 nm and a length of up to 100 μm. The actin filaments are localized under the cell membrane (as indicated in figure 1.3), but a bundle of individual actin filaments can cross over the entire cell body.

The intermediate filaments are more flexible fibers than the actin filaments. They are important for cellular and nuclear stability [28]. They are formed by single filaments of 10 nm diameter twisted around each other like a rope. They are mostly present around the cell nucleus [21].

The third major component of the cytoskeleton are the microtubules. They are formed close to the nucleus in so-called microtubule organizing centers (MTOC). They expand from MTOCs to the cell membrane. Microtubules are wide filaments produced by the polymerization of α- and β-tubulin heterodimers, which form a rigid cylindric structure of 25 nm diameter. This makes them the least flexible among the three components of the cytoskeleton. Moreover, they have a unique capacity to disassemble in one end and assemble in another [21]. The functionality of the microtubules is especially related to the chromosomes and mitotic spindles [29].

1.2.1 Cell-cell and cell-ECM interactions

The outer space of the cells is formed by the extracellular matrix (ECM), a complex network of proteins and polysaccharides secreted by the cells. These molecules include fibrous proteins such as collagen, fibronectin, elastin, and laminin, embedded in the proteoglycan and glycosaminoglycan gels [30].

Cells *in vivo* grow next to each other and are associated with the ECM. They receive and send signals from and to the neighboring cells. Cell-cell communication can be mediated in different ways by the interaction of signaling molecules

such as growth factors, hormones, chemokines, and cytokines:

1. paracrine cell-cell communication, which does not require physical contact between cells,

2. juxtracrine communication, where cells directly exchange the signaling molecules without secreting them into the extracellular space, and

3. endocrine communication is typically mediated by a hormone that travels long distances through extracellular fluids [31]

The cell-cell and cell-ECM interactions play an important role in the mechanical response and tissue formation. Cell junctions can be classified into three groups: tight junctions, gap junctions, and anchoring junctions.

The tight junctions provide direct contact between cells, and as the name suggests, they function as a strong barrier that prevents the movement of fluids having a different chemical composition from one side to another (figure 1.3 A) [32].

The gap junctions allow the small ions and metabolites to pass directly from one cell to another and induce chemical and electrical interactions between the two adjacent cells [33].

The anchoring junctions are mainly composed of transmembrane adhesion proteins, which are characterized by a cytoplasmic domain that binds to an intracellular anchor protein and an extracellular domain that binds either to the ECM or to an adjacent cell through the adhesion proteins that are present on its surface [34]. The anchoring junctions can be classified as desmosomes, hemidesmosomes, adherens junctions, and focal adhesions. They differ in the adhesion molecule and the cytoskeletal structure involved in the junctions. Desmosomes and adherens junctions use cadherins [35], while focal adhesions and hemidesmosomes use integrins [36] to bind cells to another cell and ECM. The actin filaments mediate the formation of focal adhesions and adherens junctions. On the other hand, the intermediate filaments moderate the development of desmosomes and hemidesmosomes [37].

1.3 Multicellular spheroids (MCSs)

Cancer progression is related to the genetic mutations that are behind the changes in the main functions of the cells, such as cell differentiation, cellular growth, cell-cell communications and interactions with the extracellular matrix

(ECM) [38]. The cancer tissue is a complex network that consists of neoplastic cells connected with other types of cells, such as fibroblasts, immune cells and endothelial cells. The interactions and cross-signaling between different types of cells are considered to be one of the reasons why anticancer drugs are restrained, even though there has been important progress in drug development [39]. One of the critical problems is the experimental unreliability that appears when moving from a conventional two-dimensional (2D) cell culture to *in vivo* animal models. Generally, 2D cultures are known to be very reproducible and easily controllable in the laboratory [40]. However, the 2D monolayer cultures have several limitations: lack of tissue architecture, simplified cell-cell interaction, and lack of tumor microenvironment heterogeneity. Therefore, the three-dimensional (3D) cultures have been proposed as a suitable model to act as a bridge between the animal models and the *in vitro* cell culture [41].

Multicellular spheroids (MCSs) are spherical aggregates of cancer cells that have been used to mimic the *in vivo* tumor conditions, particularly in the field of drug discovery. They were first used in 1971 [42] [43]. MCSs are applied to reproduce some important features of solid tumors: cell-cell signaling, cell-ECM interaction, gene expression and drug resistance [44] [45] [46].

1.3.1 Assembly of MCSs

MCSs are a product of the self-assembly of a group of cells, and their formation can be divided into three main steps, as illustrated in figure 1.4.

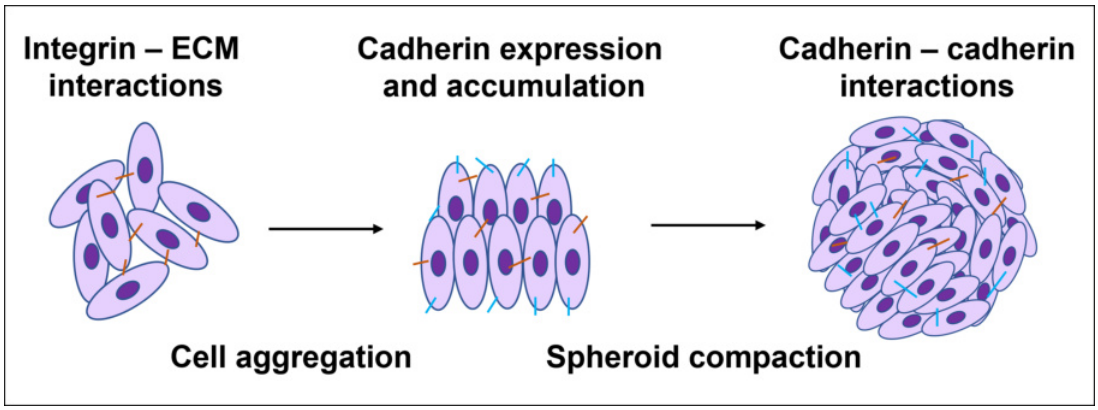

Figure 1.4: **Schematic representation of spheroids formation.** Three main steps characterize spheroid formation: 1. aggregation between cells via integrin-ECM interactions; 2. overexpression and accumulation of cadherins; 3. cadherin-cadherin interactions that form the compact cellular structure.

The formation of spheroids starts when the cells aggregate upon tight bindings

between the integrins present in the cell membrane and the long-chain ECM fibers containing the arginyl-glycyl-aspartic acid (RGD) motifs. It induces the formation of a spheroid, where the cells are loosely attached. Due to the direct cell-cell interactions, cadherin expression is upregulated, causing their accumulation on the membrane surface. It provokes homophilic cadherin-cadherin bindings, which in turn stimulate the formation of compacted cell aggregates, i.e., the multicellular spheroids [47]. The types of cadherin involved in spheroid formation vary from cell to cell, and E-cadherin and N-cadherin are the most frequently found [44]. Additionally, the structural stability of the spheroids is maintained by the forces generated within the cell cytoskeleton [49].

1.3.2 Internal structure of MCSs

Multicellular spheroids can be homotypic and heterotypic. The former refers to the spheroids composed of only one cell type (only cancer cells), while the latter indicates those that also include other types of cells, such as fibroblasts, endothelial cells, or immune cells [44]. The internal structure of the MCS is similar to the one present in a solid tumor, characterized by different cellular layers (figure 1.5).

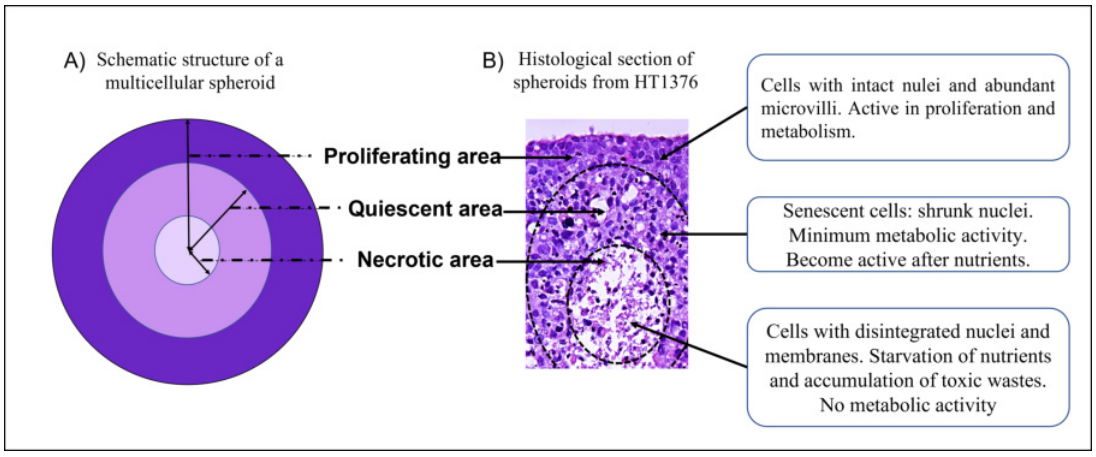

Figure 1.5: **Schematic representation of a multicellular spheroid.** A) The internal structure of an MCS can be divided into three main parts: 1. outer layer of proliferating cells; 2. inner layer of senescent cells; 3. necrotic core. B) An exemplary image of bladder cancer spheroid structure formed from HT1376 cells (hematoxylin and eosin staining of a cross-section of the spheroid).

Three different layers can be found in spheroids:

1. an external layer composed of highly proliferating and metabolically active cells;

2. a middle layer made of quiescent cells, which are metabolically inactive, but when exposed to nutrients they can start to proliferate;

3. the core formed by necrotic (dead) cells [48].

The origin of these layers arises from the diffusion limitation of the oxygen, nutrients, and accumulation of toxic wastes inside the spheroids [45].

The problems related to the impaired efficacy of anticancer drug treatment are mainly due to the layered structure of the spheroids. Depending on the molecular target of the drug, the effect may vary. For instance, drugs designed to kill the proliferating cells will not affect the inner spheroid regions, as these are composed of quiescent and dead cells. Similarly, drugs that induce the formation of reactive oxygen species to cause cell death will not affect the inner regions because of the hypoxic condition present there [44].

1.3.3 Growth kinetics of MCSs

The spheroid growth kinetics is similar to one of the solid tumors (figure 1.6).

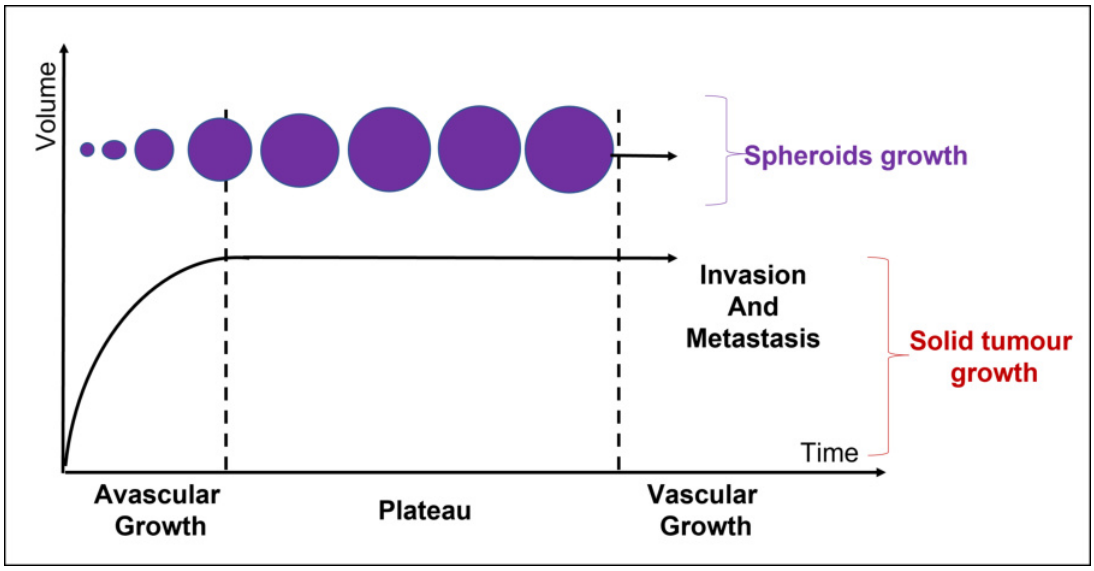

Figure 1.6: **Spheroids growth.** The spheroids have a growth pattern similar to the one of a solid tumor: an initial logarithmic growth followed by a plateau (prepared based on [46]).

The growth starts from an initial phase of logarithmic character, followed by a plateau. In the case of the solid tumor, the first stage is the so-called avascular growth. Later, there is angiogenesis, the formation of new blood vessels, which

leads to vascular growth. Afterward, the tumor may undergo invasion and metastasis. Analogously, the spheroids, during the initial growth, achieve a maximum diameter, and then after reaching the plateau, their size remains constant (i.e., volume rate remains constant) [44] [50].

1.3.4 MCSs culture systems

The spheroids-based culture systems could be divided into scaffold-based and scaffold-free approaches. The main difference between the two is the use of external biomaterials, such as collagen, Matrigel, or other kinds of hydrogels, in the case of scaffold-based systems. In both conditions, there is a high number of cell-cell and cell-ECM interactions. An important advantage of the scaffold-free system is that the cells produce ECM alone, and the gradient of nutrients, gases, and pH is maintained. On the contrary, ECM is produced artificially in the scaffold-based system, and the major difficulty relies on isolating the spheroids from the scaffolds for further experiments. Likewise, one disadvantage of the scaffold-free system is the lack of standardized protocols for forming spheroids. The production of spheroids of uniform size and features requires a high level of optimization [40] [51].

There are several methods to generate MCSs, among which the most popular one is to culture them on non-cell adherent surfaces. This procedure consists of seeding a high number of cells on surfaces that are pre-coated with substrates inhibiting cell adherence [45]. Such substrates could be made of simple agarose gel [52] or hydrophobic polymers like PHEMA (poly 2-hydroxyethyl methacrylate) [53]. It is a simple method, but in order to reproduce the same size of spheroids, depending on the cell line of interest, the seeding number (referred to here as the number of seeding cells) and the medium composition need to be determined precisely [54].
Figure 1.7 presents an example of a spheroid culture method using commercially available U-bottom-well plates.

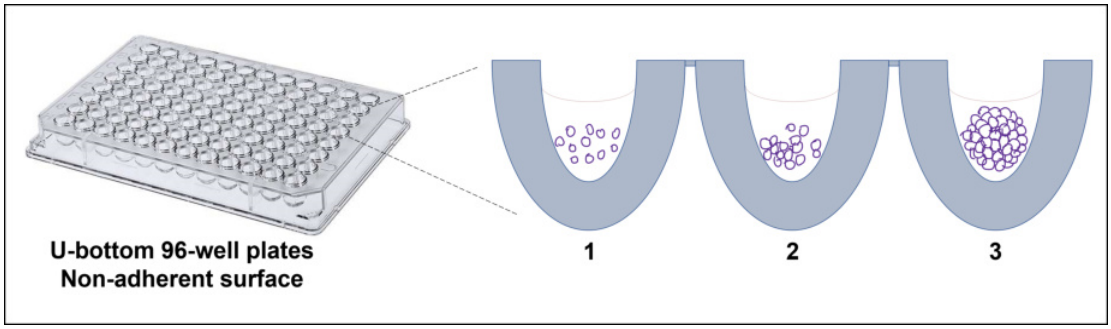

Figure 1.7: **Spheroid culture in non-adherent surface plate.** There are commercially available 96-well plates with U-bottom and non-adherent surface that can be used to generate spheroids. 1. Seeding of a certain number of cells (depends on the cell type and the desired size of the spheorids) 2. Cells are in contact each other and starts to aggregate. 3. Formation of a spheroid.

96-well plates with U-bottom and non-adherent surfaces can be used to generate spheroids in three steps. First, depending on the cell type and the desired size of the spheroids, a certain number of cells are seeded in each well. Then, because of the non-adherent surface of the wells, cells are in contact with each other and start to aggregate until they finally form spheroids. Spheroids can be cultured in the same wells for several days or even weeks.

1.4 Cell mechanics

The term cell mechanics is used to describe the link between force and deformation applied to cells. Cells are generally subjected to forces that induce stresses, which could be classified depending on the type of action (figure 1.8).

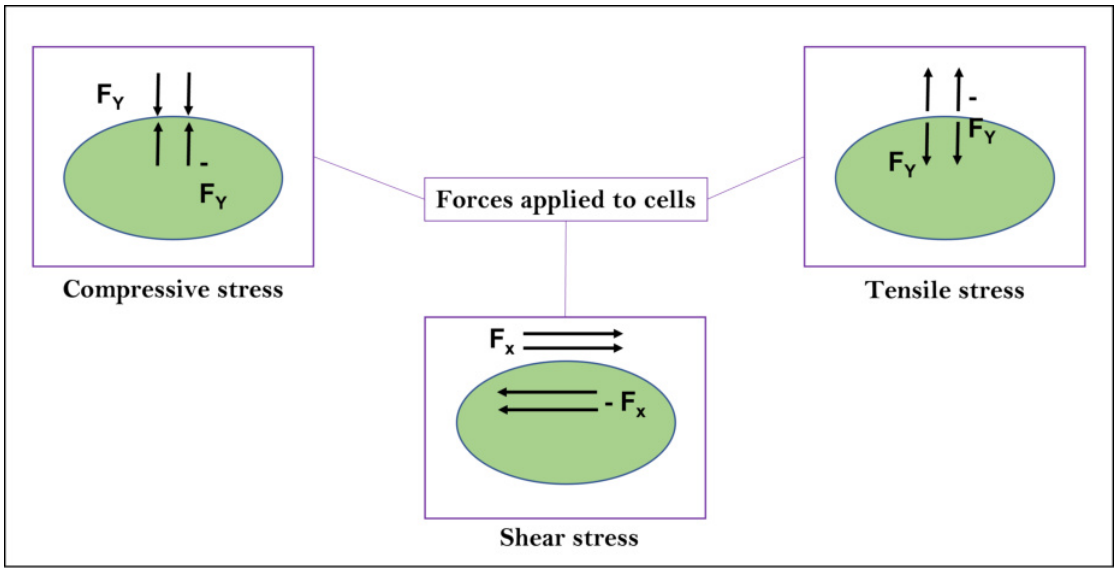

Figure 1.8: **Illustration of the forces acting on cells inducing compressive, tensile, and shear stress.** F_x and F_y are the forces applied on cells; -F_x and -F_y are the forces generated by the cell's reaction.

Depending on the direction of the force acting on the cell surface, either perpendicularly or laterally, they may cause:

1. compression - the stress is applied perpendicularly to the cell surface, towards the cell center. It causes compaction.

2. tension - the stress (called tensile stress) is applied perpendicularly to the cell surface, towards the cell exterior. It causes expansion (stretching) of the cell.

3. shear - the stress is applied parallelly to the cell surface (like the one generated by the blood flow in vessels). It causes the angular change between opposing sides of the cell [55].

1.4.1 Cell mechanics and cancer

Cancer is a disease characterized by uncontrollably dividing abnormal cells subjected to genetic mutations [38]. One of the most frequently mutated genes is

the gene p53, a tumor suppressor gene that promotes cell proliferation by arresting apoptosis and repair mechanisms after DNA damage [57]. Cancer research has been mainly concentrated on investigating such kinds of genetic alterations, but since it has been demonstrated that, compared to normal cells, the mechanical properties of cancerous cells and the organization of their cytoskeletal network are altered [56] [58] [59]. Mechanics of cells has reached an important role in cancer research along with the traditional genetic and biochemical studies.

Cancer cells are known to be subjected to force changes during cancer progression due to the fast-dividing process in a restricted space [55]. Likewise, several mechanical events take place during tumor progression. For instance, there is an overproduction of collagen by stromal myofibroblasts that causes stiffening in the matrix [60]; the tumor mass expansion induces compression [61], and because of the poor lymphatic drainage there is a rise in the interstitial pressure [62]. Furthermore, when cancer cells move into the blood or lymphatic vessels during metastasis, the high hydrostatic pressure facilitates their attachment to the ECM or the epithelium [63]. Thus, compared to normal cells, cancer cells should be characterized by different mechanical properties. Indeed, *in vitro* studies have shown that metastatic tumor cells are softer than normal cells [64] and that these differences are related to the organization of the cell cytoskeleton and the interactions of cells with the surrounding environment [65] [66] [67] [68]. Taking into account all these results, by better understanding the relationship between the nanomechanical properties of cancer cells and their cellular structures, it would be possible to improve diagnosis and identify innovative biomarkers and new potential therapeutic targets.

1.4.2 Cellular modelling in biomechanics

A material can be purely elastic, purely plastic, or viscoelastic [69] [70] [71]. A purely elastic material can resist external force and recover its shape and size once the stress is removed [69]. On the contrary, a purely plastic material recovers only partially its initial shape and size when subjected to external forces [70]. In biological materials, a viscoelastic behavior has been mainly observed, where there is a partial recovery of the shape and size, but with energy dissipation due to internal friction [71].

When stress is applied, the material starts to deform (figure 1.9).

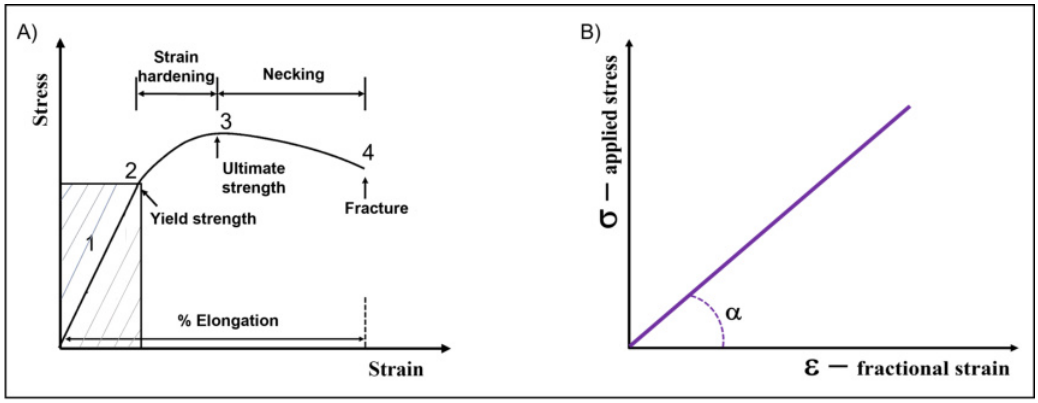

Figure 1.9: **Stress-strain curve.** A) Deformation of material upon external stress acting on it. The deformation begins with an elastic region (1) that is reversible until the yield strength (2), the stress limit after which the plastic deformation takes place. Increasing the stress reaches the ultimate strength (3), and after this, the material will fracture (4). From 1 to 3, there is strain hardening. Once the ultimate strength is reached, necking starts. B) Ideal stress-strain curve in the elastic region (prepared based on [72])

Until a certain stress limit, called the yield strength, there is an elastic region where the deformation is reversible. After this limit, plastic deformation takes place. By increasing the stress, the ultimate strength is reached, and after this, the material will fracture. At the initial phases of the deformation (from 1 to 3), strain hardening is observed, during which stress and strain increase. Once the ultimate strength is reached, the necking process, i.e., a large amount of strain applied in a small region of the material, begins and determines the fracture of the material.

Figure 1.9 B presents an ideal stress-strain curve in the elastic region, where stress is proportional to strain. In this region, Hooke's law can be applied to describe the deformation of the material:

$$\sigma = E\varepsilon \tag{1.1}$$

where, σ is the applied stress, E is Young's modulus and ε is the fractional strain.

Young's modulus, by definition, is the ratio between the stress σ applied along an axis and the strain ε along the same axis in the range where Hooke's law can be applied. The stress is defined as the force per unit area, and the strain is determined as the deformation caused by the initial length (figure 1.10).
In this case, Young's modulus can be determined using the following equation:

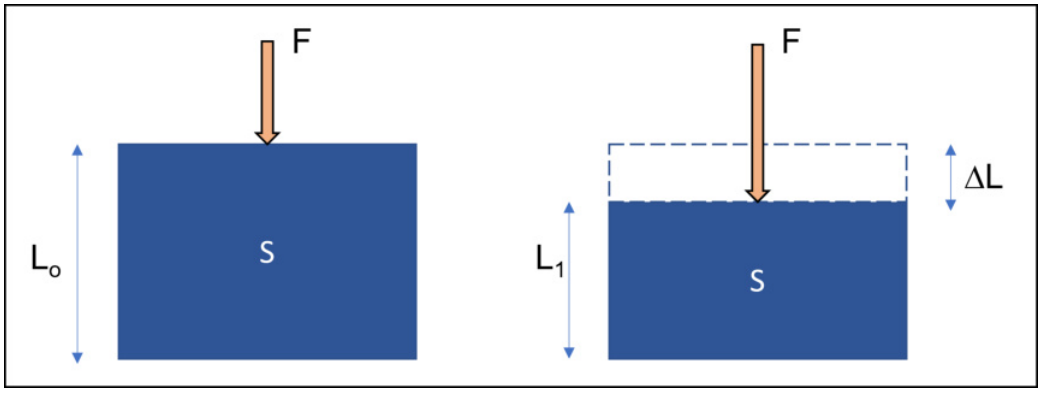

Figure 1.10: **Compression of a material.**

$$E = \frac{F}{S}\frac{L}{\Delta L} \tag{1.2}$$

where the stress is defined as the force (F) acting on the surface area of the sample (S), while the strain is given by the change of the sample length (ΔL) in relation to the initial length (L). In addition to this, another important parameter that needs to be mentioned is Poisson's ratio, which indicates the relation between the relative contraction (lateral strain) and relative expansion (longitudinal strain) of a material undergoing stretching (figure 1.11).

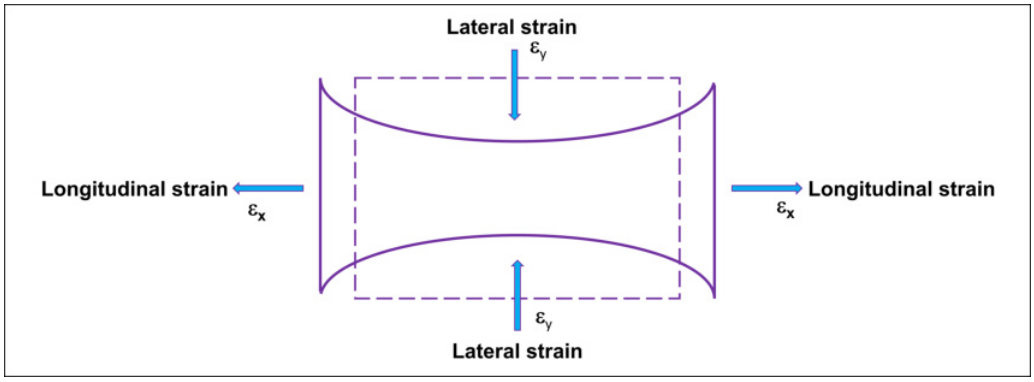

Figure 1.11: **Definition of Poisson's ratio.** Poisson's ratio is the relation between the lateral and longitudinal strains.

The Poisson's ratio is defined as:

$$\mu = \frac{\varepsilon_y}{\varepsilon_x} \tag{1.3}$$

Cells are viscoelastic materials. Although several theoretical models describe such properties [73] [74], it is challenging to apply them. Instead, they are typically considered elastic materials due to their modelling complexity. Young's modulus is often used in such conditions to quantify their mechanical properties. For

living cells, the Poisson's ratio is equal to 0.5, assuming that cells are an ideally incompressible material [75] [78].

1.4.3 Cellular modelling: viscoelasticity

Rheology studies the flow and deformation of matter that defines the correlation between force, time, and deformation [79]. It deals with the deformation of purely solid-like materials, fluid-like materials and complex viscoelastic materials, such as cells, which behave solid-like and liquid-like materials. At the macroscale, the viscoelastic property of a biomaterial is generally studied by using a rheometer or a dynamic mechanical analyzer [80]. The term *microrheology* is referred to the microscale [81].

Viscoelasticity is the combination of a solid-like and fluid-like behaviors. Under strain, an elastic material behaves like an ideal solid material that can be compared to a spring which returns to its undeformed state after being stretched. In equation 1.1, the relation between the shear stress and strain is defined by the constant of proportionality of elastic modulus (solid material follows Hooke's law). On the other hand, a perfectly viscous material follows Newton's law:

$$\eta = \frac{\sigma}{\dot{\gamma}} \tag{1.4}$$

where η is the dynamic viscosity (Pa s), σ shear stress (Pa) and $\dot{\gamma}$ shear rate (s^{-1}).

The shear rate can defined as the velocity gradient, which is the ratio between the difference in velocity of the two surfaces containing the fluid and their distance. The flow behavior, determined during the viscoelastic measurements, is the shear flow, which can be imagined as layers of fluids one over the other, where the velocity increases from the bottom to the top layer (figure 1.12).

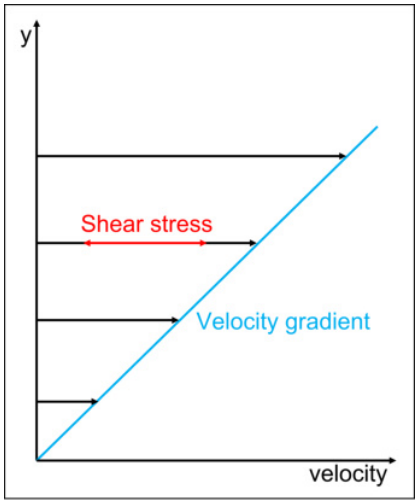

Figure 1.12: **Schematic illustration of a shear flow.** The black arrows indicate the movement of the layers of fluids at increasing velocity, and the velocity gradient is indicated in blue.

When shear stress is applied, an ideal Newtonian fluid behaves so that the shear rate, i.e., the velocity gradient, is proportional to the stress. Such material can be simplified with a dashpot, a mechanical instrument composed of a plunger that moves across a viscous Newtonian fluid. In this case, unlike the spring that goes back to its original form, the dashpot begins deforming under stress at a constant rate and loses its initial shape, accompanied by an energy dissipation. The strain (ε) and the shear stress are related by the following equation:

$$\varepsilon = \frac{\sigma t}{\eta} \tag{1.5}$$

where ε is the strain, σ shear stress, η viscosity and t the time.

Various combinations of springs and dashpots can be applied to represent a viscoelastic material. Among several models, the most common ones describing viscoelastic materials are the Maxwell model for a viscoelastic liquid and the Kelvin-Voigt model for a viscoelastic solid [87] (figure 1.13).

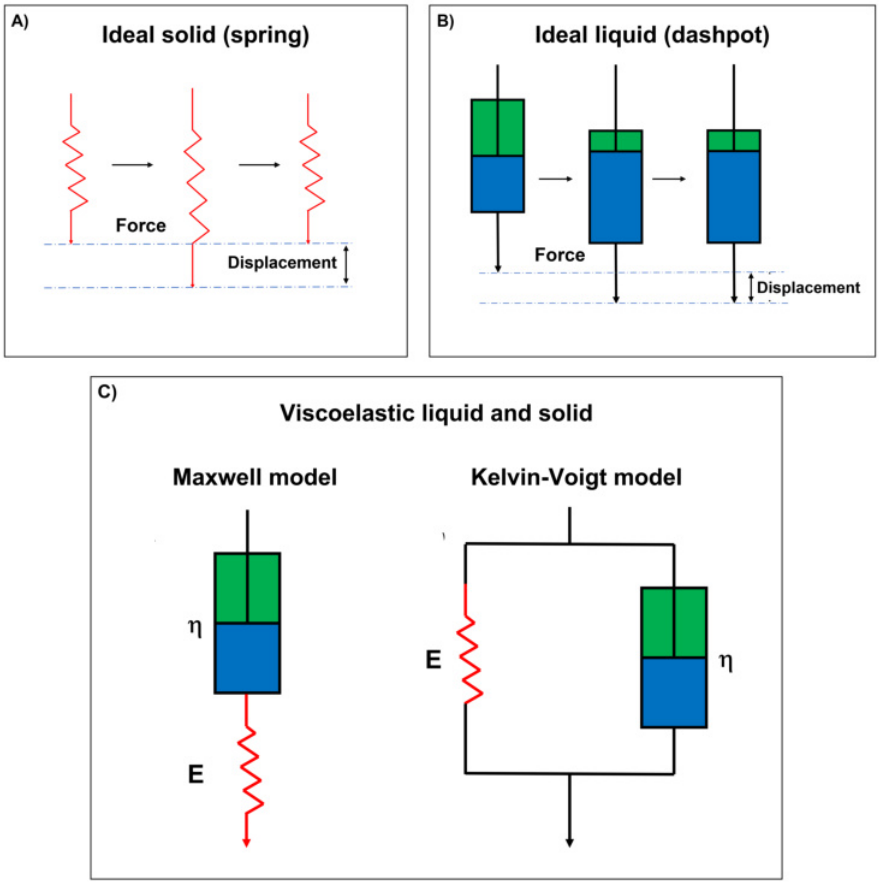

Figure 1.13: **Schematic illustration of the behavior of ideal materials.** A) the spring model of an ideal solid responding to the application and removal of a strain. B) An ideal fluid behavior upon application of an external strain-induced force. C) Maxwell model representing a viscoelastic fluid, and the Kelvin-Voigt model representing a viscoelastic solid material.

In the Maxwell model, the two elements (spring and dashpot) are connected in series, while in the Kelvin-Voigt model, dashpots and springs are connected in parallel. Under stress, the elastic modulus E, gives the main response, which is then substituted by the viscous component governed by the strain rate η. In the Kelvin-Voigt model, the spring reacts to the stress after the dashpot, so the elastic behavior follows the viscous one after the so-called retardation time, expressed as the ratio between the strain rate and the elastic modulus. This transition of the two phases can be expressed in the equation below:

$$\varepsilon = \frac{\sigma}{E}[1 - e^{-t/\lambda}] \tag{1.6}$$

where ε is the strain, σ the shear stress, and λ the retardation time.

1.4.4 Burgers model

Often, the Burgers model is applied to describe the viscoelastic behavior of a material. This model can be seen as a combination of Maxwell and Kelvin-Voigt models linked in series [84]. An exemplary representation of this model and the creep-relaxation curve is presented in figure 1.14.

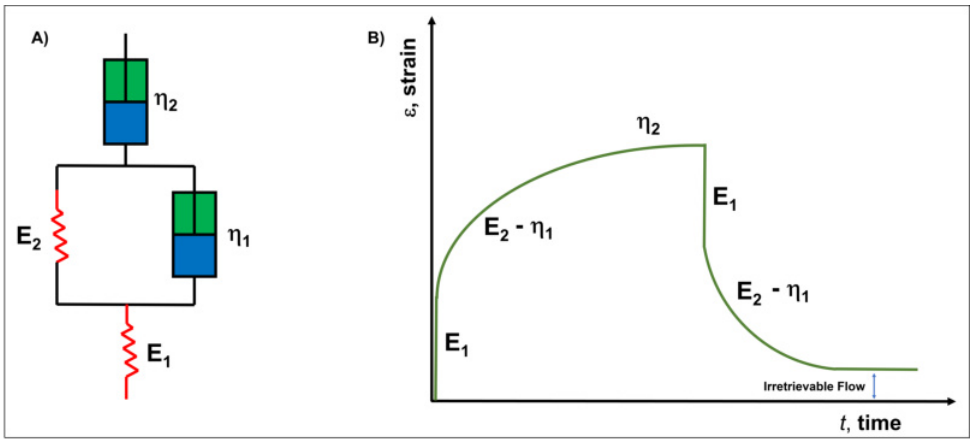

Figure 1.14: **Burgers model and the creep-recovery curve.** A) Connection in series of Maxwell and Kelvin-Voigt models. B) Representation of the creep-relaxation curve.

When stress is applied, there is an immediate elastic deformation of the Maxwell spring, and then a creep causes an irrecoverable viscous flow in the dashpot. This means that there is a permanent deformation of the material, leaving an irrecoverable flow, and even after removing the stress, it does not return to its initial state. By putting together the equations from the various models, the strain for the Burgers model can be obtained by the following expression:

$$\varepsilon = \sigma(\frac{1}{E_1} + \frac{1}{E_2}(1 - e^{-t/\lambda}) + \frac{t}{\eta_2}) \tag{1.7}$$

where ε is the strain, E_1 and E_2 the elastic modulus of the springs, σ the shear stress, λ the retardation time, η the strain rate, and t the time.

1.4.5 Oscillatory measurements

A rotational rheometer is one of the most commonly used methods to study the viscoelastic properties of various materials, particularly using small amplitude oscillatory shear testing [85]. The measuring system generally comprises two parallel plates where the sample is loaded between them at a known height. Then, an oscillation at a certain stress or strain is applied to the upper plate, generating a sinusoidal wave at the given amplitude and frequency. The stiffness of the material is then given by the complex modulus G^*, defined as the ratio between the shear stress σ and the strain ε [86]. Figure 1.15 shows the relationship between stress and strain waves for a purely elastic, viscous and viscoelastic material.

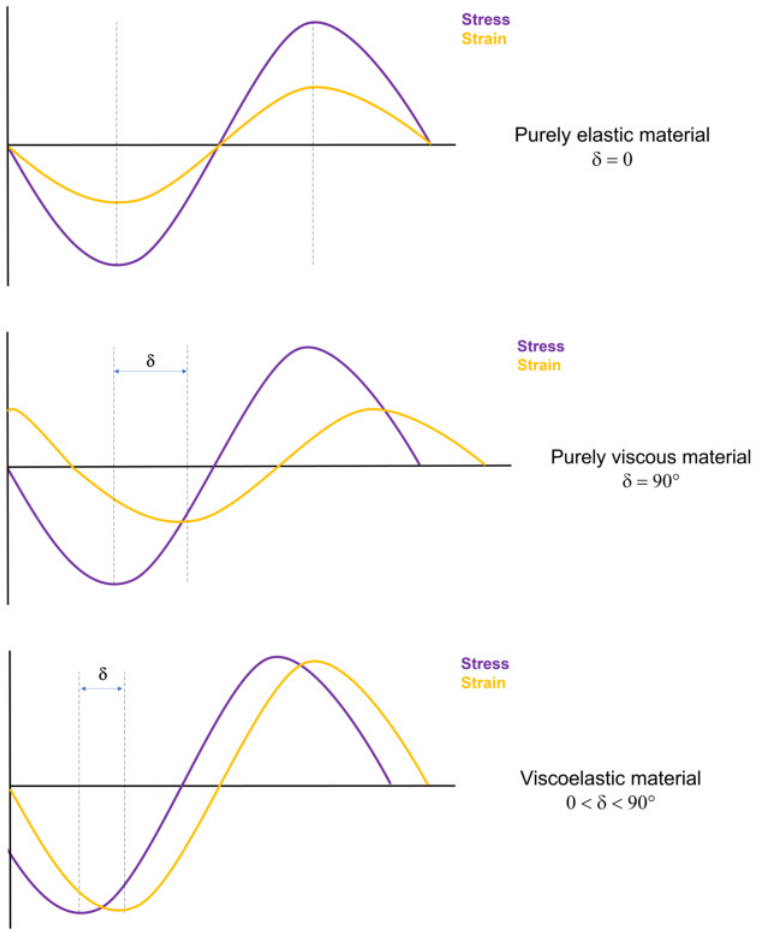

Figure 1.15: **Relationship between stress and strain waves in the different materials.** For a purely elastic material there is no phase shift in the two waves; for a viscous material the shift is equal to 90°, and in the case of a viscoelastic material the phase shift is between 0 and 90°. Purple: stress, yellow: strain; δ: phase angle.

The complex modulus can be described as follows:

$$G^* = G' + iG'' \tag{1.8}$$

where G' is the real and G'' is the imaginary part of the complex modulus (i stands for an imaginary number). Alongside, a complex viscosity η^* can be defined in function of the angular frequency ω:

$$\eta^* = \frac{G^*}{\omega} \tag{1.9}$$

When a sinusoidal force is applied, the complex shear modulus can be expressed as two components: storage modulus G' which is in-phase and refers to the elastic behavior of the sample, and loss modulus G'' which is out of phase and refers to the viscous behavior of the sample. The ratio between loss and storage modulus, i.e., $\tan\delta$, describes the dissipation of the material's energy. The phase angle δ can be used to determine the two components. For a purely elastic material, δ equals to 0 ; for a purely viscous material δ equals to 90°. For a viscoelastic material, its value is placed between 0 and 90°. By applying the basic trigonometry, the storage and loss modulus can be calculated [82] (figure 1.16 A).

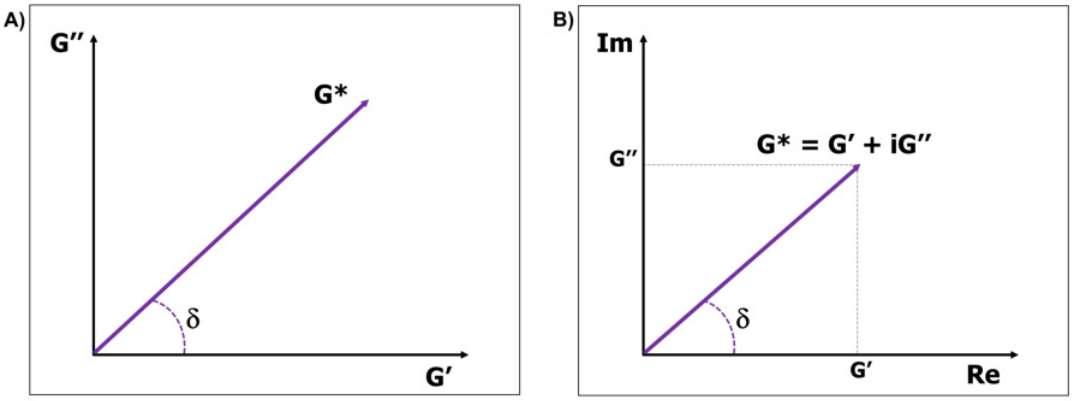

Figure 1.16: **Vector and Argand diagram of the complex modulus.** A) The relationship between the two components of the complex modulus, storage (G') and loss (G'') moduli, are shown. B) The same relation is indicated in the Argand diagram with the real and imaginary axis.

The relationship between the storage and loss modulus can also be expressed by using complex number notations, where G' stands for the real part and G'' for the imaginary part of the complex modulus G^* by applying the so-called Argand diagram (figure 1.16 B). The Argand diagram for the complex modulus shows the real axis (x-axis) and the imaginary axis (y-axis).

Complex shear modulus has two components, i.e., storage G' and loss G'' modulus defined as:

$$G' = G^* \cos\delta \tag{1.10}$$

$$G'' = G^* \sin\delta \tag{1.11}$$

The ratio between G" and G" is the loss factor (tan δ):

$$tan\delta = \frac{G''}{G'} \tag{1.12}$$

1.4.6 Viscoelastic models

Seeing how complex the organization of a cell structure is, finding the proper model to describe the mechanics of cells has always been a challenge. To make things less complicated, cells are generally treated as homogeneous materials [88]. Based on this, there are some models that provide information regarding the viscosity and elasticity of the cells, allowing a quantitative comparison between different groups of cells [89] [90]. A simple way to study the mechanical properties of cells is to consider Young's modulus, a parameter that mainly defines the elastic contribution. Therefore, the main limitation of such a model is that it does not consider the real viscoelastic nature of the cells. To overcome the limitations given by Young's modulus, several models that portray the cells as a viscoelastic material have been proposed: power law and soft glassy rheology [98] [75], poroelasticity [92] [93], tensegrity [94] and the traditional viscoelastic models [95].

Poroelastic model

This model considers the cells as a mixture of two different materials: a tight elastic cytoskeleton network within the bounds of a viscous cytosol [92]. When deformation is locally applied to the material, the elastic phase (cytoskeleton) starts remodeling, and it induces an increase in the pressure of the surrounding fluid, which begins to flow away from the site of distress and produces a non-stop deformation right up to the moment the pressure re-equilibrates. This model has been used to interpret the mechanical behavior of soft tissues [96], collagen gels [97] and cells [93].

Power law and soft glassy rheology

The power law model was first applied to cells in 1997 by Tsai and Hammer [98]. Unlike the traditional viscoelastic models, they defined stiffness as a function of frequency. It was empirically observed that a large number of cells present rheological properties similar to emulsions and foams; thus, they behave like soft glass, a material that has both the disordered state of a fluid and the rigidity of a solid [99]. It led to the description of the soft glassy rheology (SGR) [100]. The principle of this model is based on a structure in which the microscopic constituents are always out of thermodynamic equilibrium, in a metastable state, and they have to cross energy barriers that are higher than the system's thermal energy before reaching the equilibrium [101]. The power law - SGR model has been widely used to study the viscoelasticity of cells with several techniques, including AFM [75]. It was demonstrated that applying a wide range of frequencies increases the elastic and viscous moduli following a weak power law. However, the main drawback is that this model considers only one power law regime, while studies show that the relaxation follows multiple power law regimes, implying that cells do not behave like soft glass [102]. Moreover, the SGR model does not explain the mechanical behavior of cells at very high frequencies. Despite this, power law and the SGR model remain valuable approaches to describing the viscoelastic properties of cells.

1.5 Methods used to assess mechanical properties of single cells

There are many different techniques to determine the mechanical properties of single cells [67]. Among these, atomic force microscopy (AFM) [103], microfluidics [104], optical trap [105], magnetic tweezers [106], magneting twisting cytometry [101], particle microrheology [107], micropipette aspiration (MPA) [108] and traction force microscopy [109]. Among these, AFM and MPA are the ones that are addressed in the current study.

AFM is a powerful tool for measuring biological materials, topography, and force spectroscopy. Therefore, it can be used as an imaging technique to determine the mechanical properties of living cells [110]. The main advantage of AFM is that it enables the performance of the measurements in fluid, consequently in an environment close to the physiological conditions of the cells. One of the first works showing the differences between the elastic properties of normal and

cancerous bladder cells dates back to 1999 by Lekka et al. [111]. They demonstrated that the cancerous cells were much softer than the normal cell line, with a lower value of Young's modulus. The reason behind this softening was shown to be related to the absence of a well-developed cytoskeleton in the metastatic cells. Following this, more studies were conducted on bladder cancer cells [112] [113] [114]. Moreover, not only in bladder cancer cells but also in other types of cancers, such as ovarian, it was validated the direct correlation between the actin filaments and the biomechanical fingerprints of the cancer cells [115].

MPA has been widely applied to study the mechanical properties of both non-adherent and adherent cells [116] [117]. Using the liquid droplet model, it is very common to assess the cell's apparent membrane tension and cytoplasmic viscosity, which is here compared to a bag filled with fluid and with constant surface tension [118]. By measuring the flow rate of a cell into a micropipette, it is possible to determine also the cell viscosity [119].

Chapter 2

Principles of the applied techniques

2.1 Atomic Force Microscopy

Atomic Force Microscopy (AFM) is a type of scanning probe microscopy with a very high spatial and force resolution that enables the imaging and quantification of mechanical properties of living cells at the sub-nanometric level [110] [111] [112] [113]. It enables the measurements in liquid conditions by mimicking the physiological ones. In figure 2.1 there is a schematic representation of the AFM.

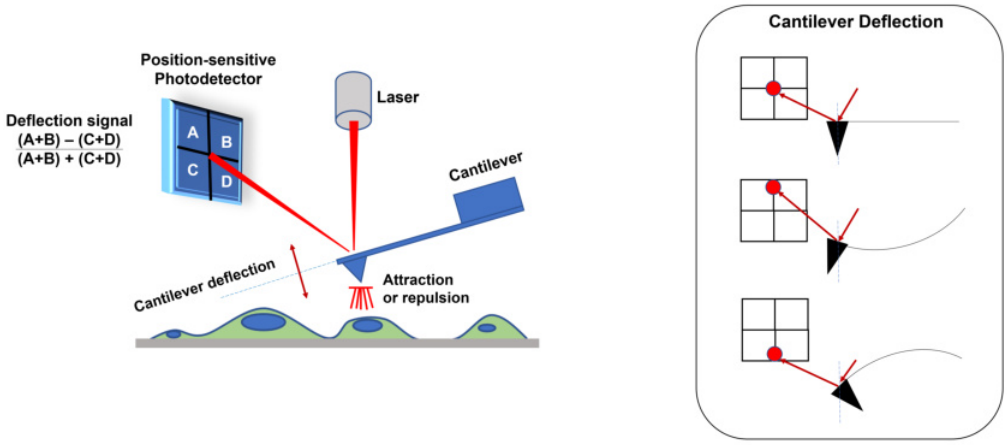

Figure 2.1: **Schematic illustration of the main components of atomic force microscope.** A sample (here cells) is probed with the cantilever, at the end of which there is a probing tip. When the probing tip touches the surface, the forces acting within the contact area cause the cantilever deflection. The deflection is registered by a position-sensitive detector (a photodiode), whose active area is divided into four quadrants.

The AFM comprises three main components: a cantilever with a probing tip mounted at its free end, a piezo-scanner, and an optical system. The cantilever can move up and down perpendicularly to the investigated sample surface. When

the probing tip is in contact with the surface, the forces acting within the contact area deflect the cantilever. The cantilever deflection is recorded by the optical system composed of a laser and position-sensitive detector. A laser beam is focused on the back of the cantilever (above the tip). A reflected laser beam is directed to a position-sensitive detector, a photodiode, whose active area is divided into four quadrants. The deflections perpendicular to the surface change the position of the laser beams between the upper and lower quadrants while twisting the cantilever is recorded as a difference between the left and right quadrants. The third basic AFM element is a piezoelectric motor and scanner used to move the sample.

2.1.1 Cantilever calibration

The deflection of the cantilever is measured in Volts by the optical system. Therefore, a calibration procedure is necessary to obtain exact information about the cantilever deflection in the metric unit. Because AFM measurements are intended to obtain information about forces, the cantilever deflection should be expressed as the force (F) of interaction that follows Hooke's law:

$$F = k \cdot \Delta z \tag{2.1}$$

where k is the spring constant of the cantilever and Δz is the deflection of the cantilever.
The deflection of the cantilever measured in volts is then converted into force units by using the formula below:

$$Force[nN] = I[V] \cdot invA[nm/V] \cdot k[N/m] \tag{2.2}$$

where I is the AFM signal recorded in volts and $invA$ is the photodetector sensitivity.

Every cantilever is characterized by unique physical and geometrical properties such as length, width, thickness, the shape of the probe, resonance frequency and spring constant. All together, these parameters are necessary to determine the actual value of the spring constant, which is essential for a correct measurement of the mechanical properties of the sample. Generally, the cantilever spring constant is calculated by applying the thermal excitation method, which is based on recording the thermally-excited oscillation of the cantilever-free end. The spring constant of the thermally excited cantilever is connected to the measured

amplitude through the Boltzmann's equipartition theorem, which the following equation can describe:

$$1/2k < X^2 >= 1/2k_BT \tag{2.3}$$

where k is the cantilever spring constant, $<X^2>$ is the time averaged square oscillation amplitude, T is the absolute temperature and k_B is the Boltzmann constant.
When the spring constant is not automatically calculated from the software, it is possible to determine its value by considering the mass of the cantilever as equal to the nominal mass and applying the following formula:

$$K_{cant} = K_{nom} \cdot (f_{cant}/f_{nom})^2 \tag{2.4}$$

where k_{nom} and f_{nom} are the nominal spring constant and nominal resonant frequency, while f_{cant} is the measured resonant frequency and k_{cant} the calculated value of the spring constant [120] [121].

Along with the determination of the cantilever spring constant, another key element of the calibration is the determination of photodetector sensitivity, which is the linking factor of the deflection recorded in volts and the equivalent deflection in nanometers. For this, a force curve [*I(V)* versus *Z(μm)*] is recorded on the stiff substrate, usually a glass coverslip or a plastic Petri dish, and in this case the cantilever deflection corresponds to the piezoelectric scanner position. The slope of the obtained force curve is the inverse of the photodetector sensitivity *(invA)*, which reports the connection between volts and nanometers.

2.1.2 Force-distance curves

The elasticity measurements realized by AFM rely on acquiring so-called force curves. The cantilever deflection is recorded as a function of the relative scanner position, which is converted into a force-distance curve. Therefore, a force curve is a relation between cantilever deflection and the relative sample (or tip) position. Figure 2.2 illustrates a force curve recorded on stiff non-deformable and compliant samples.

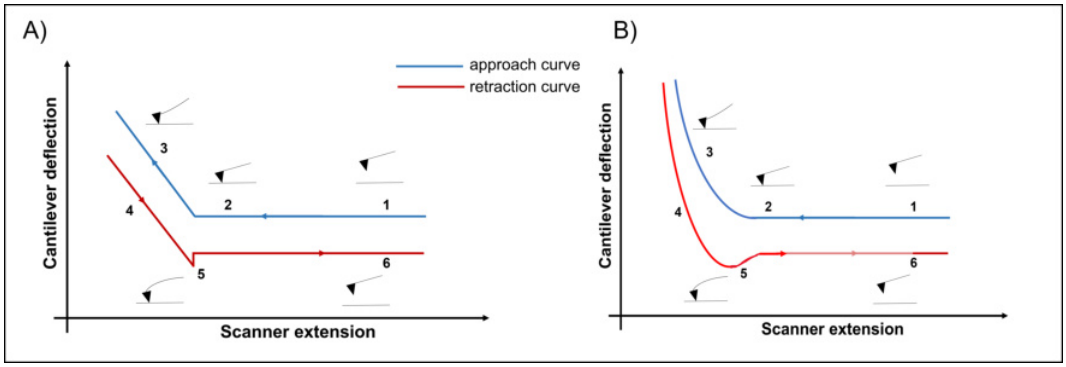

Figure 2.2: **Force-extension curve.** A) An example of a force-extension curve showing the bending of the cantilever. The tip is moved downwards (1) until it gets close to the sample (2). Once the tip is in contact with the sample (3), a force is exerted on the substrate for a few seconds. After this, the tip is moved away from the surface (4-5) until the starting position is reached again. B) An example of a force-extension curve for a soft sample.

The main features of a force curve consist of a flat baseline, which indicates that the interaction forces between the tip and sample may be neglected as the tip is far away from the sample surface (1). A tilled baseline is usually an artefact and must be subtracted from the force curve. Then there is a contact point, i.e., the position when the AFM probe touches the sample surface (2). The region above the contact point indicates the deflection of the cantilever due to the interaction between the tip and the sample surface (3). When the tip approaches the sample surface, the deflection increases up to a maximum force value, while when the AFM tip is withdrawing from the sample surface (retraction), the deflection decreases (4-5) until the tip detaches (5) and the original baseline is recovered (5-6).

2.1.3 Determining elastic properties of soft samples

Determining the mechanical properties of soft samples like cells or tissue relies on comparing two force curves recorded on stiff, non-deformable, and soft samples (figure 2.3)

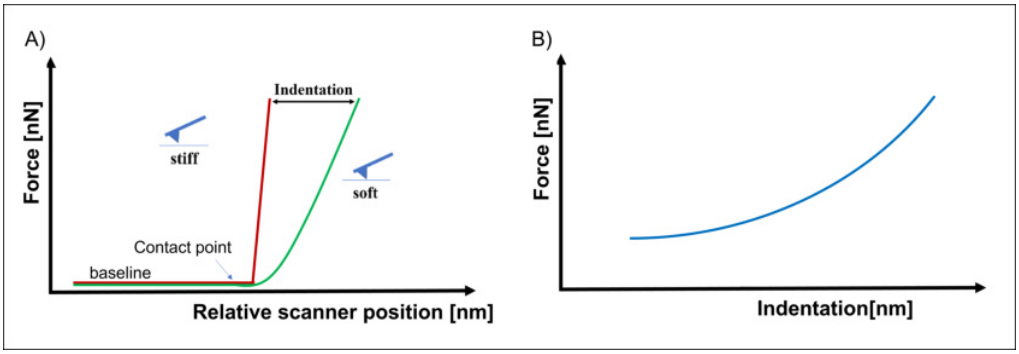

Figure 2.3: **Force - distance curves.** A) Comparing approach parts of force curves recorded on stiff, non-deformable (red curve) and soft (green curve) samples. B) the corresponding force versus indentation curve.

By subtracting these curves, a force versus indentation relationship can be obtained. This relation is further used to determine Young's modulus based on contact mechanics [122]. The most common approach analyses force-indentation curves using the Hertz model with Sneddon modifications [123]. This model assumes that a rigid spherical probe indents a purely elastic, isotropic half-space, and no adhesion is present within the contact area between the indenter and the surface. In the AFM, the probing tip typically has a pyramid shape [124] [125]. Common geometries that approximate the tip are a paraboloid, a cone, and a four-sided pyramid. The relations between the load force F and the resulting indentation δ are the following:

- conical approximation of the probing tip:

$$F(\delta) = \frac{2\tan\alpha}{\pi} E'\delta^2 \tag{2.5}$$

- paraboloidal approximation of the probing tip:

$$F(\delta) = \frac{4\sqrt{R}}{3} E'\delta^{3/2} \tag{2.6}$$

- pyramidal tip:

$$F(\delta) = \frac{\tan\alpha}{\sqrt{2}} E'\delta^2 \tag{2.7}$$

where α is the opening half-angle of the probing tip and R is the radius of the curvature of the tip [145].

In all the above equations, E' denotes the reduced Young's modulus relating Young's moduli of the tip (E_{tip}) and the investigated sample (E_{sample}):

$$\frac{1}{E'} = \frac{1-\mu_{tip}^2}{E_{tip}} + \frac{1-\mu_{sample}^2}{E_{sample}} \tag{2.8}$$

where μ_{tip} and μ_{sample} represent the Poisson ratios of the cantilever and the sample. In the case of cells, the exact value of μ_{cell} is not known. Its value is often set to 0.5, assuming that the cell is an incompressible material composed of water [78].

The elastic modulus of the living cell is in the order of kPa, while the one for the cantilever is generally in the order of GPa, meaning that $E_{cell} << E_{tip}$, and therefore the reduced Young's modulus can be simplified into:

$$\frac{1}{E'} = \frac{1-\mu_{cell}^2}{E_{cell}} \tag{2.9}$$

From this, the reduced elastic modulus of the cell can be written as:

$$E' = \frac{E_{cell}}{1-\mu_{cell}^2} \tag{2.10}$$

As mentioned earlier, the elastic modulus depends on the various geometrical approximation of the tip, and it is derived by fitting the experimental data to the chosen Hertz-Sneddon model. In this study, the cone model was used to approximate the pyramidal shape tip to obtain the elastic modulus from all the samples. By using the above relation, the final equation that describes the relationship between the load force F and the indentation δ for the AFM tip approximated by a cone is the following:

$$F(\delta) = \frac{2\tan\alpha}{\pi}\frac{E_{cell}}{1-\mu_{cell}^2}\delta^2 \tag{2.11}$$

For the tip with a spherical shape, the equation becomes:

$$F(\delta) = \frac{4}{3}\frac{E_{cell}}{1-\mu_{cell}^2}R^{1/2}\delta^{3/2} \tag{2.12}$$

where R is the tip radius.

The final value of the elastic modulus is strictly related to the model chosen for fitting the experimental data; thus, the proper model should be used to avoid introducing artifacts. Based on the previous works on bladder cancer cells [154] [112], the probing tip was approximated by a cone as the most suitable one for the

studies illustrated in this thesis. Another limitation of the standard indentation-based approach is that it gives the average value of the moduli from the various cellular compartments within the fixed indentation depth. Nevertheless, to perform comparative studies to differentiate the general mechanical properties of cells, it is enough to acquire force maps over the central region of the cells that correspond to the nuclear region [126].

2.1.4 Time domain microrheological measurements

In the AFM, the microrheological measurements can be realized in the frequency domain (dynamic experiments) or time domain (static experiment) [127].

The time domain experiment typically has a step-hold pattern (figure 2.4).

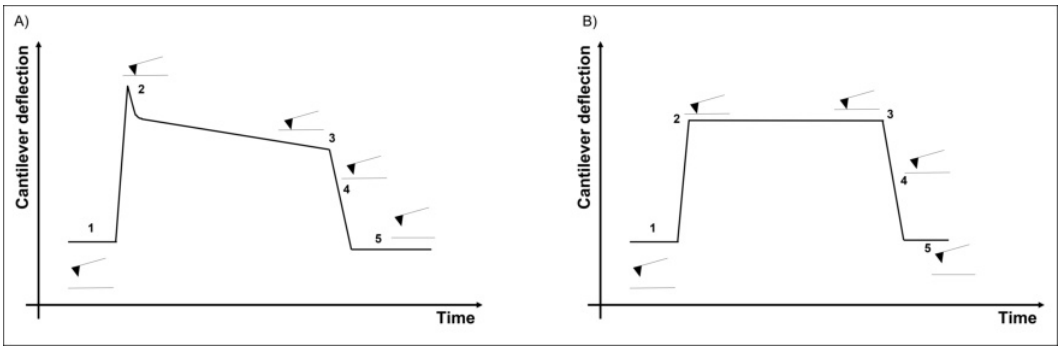

Figure 2.4: **An example of force versus time data in AFM time domain experiments.** A) Stress relaxation: the tip is moved towards the sample until the indentation (1-2) is kept constant during the hold phase. Then, after this hold phase (2-3), the tip is removed from the sample and retraction (4-5). B) Creep relaxation: this is like the stress relaxation experiment, except that the force is kept constant here.

The approaching phase (segments 1-2) is the same as for the conventional elastic experiments, and once the tip reaches the sample, there is a hold phase (segments 2-3) followed by the retraction phase (segments 4-5). The hold phase can also be called a clamp. During this phase, either the force or the indentation is kept constant, and the other is measured as time-dependent. When the invariable indentation characterizes the hold phase, the stress-relaxation experiment can be performed. In this case, it is possible to observe the constant decay of the force interacting between the tip and the sample. The force is kept constant during the hold phase in the creep relaxation experiment while the indentation value is measured. Both force (F) and indentation (δ) from these experiments can be calculated by applying the Lee-Radok equation [127]:

$$F(t) = C_n \frac{E(t)}{1-\mu^2} \delta_0^n \tag{2.13}$$

$$\delta^n(t) = \frac{1}{C_n} J_E(t)(1-\mu^2) F_0 \tag{2.14}$$

where C_n is the constant value related to the shape of the tip (i.e., cone: n= 2 and C_2= *2(tanα)/π*), *E(t)* is Young's relaxation modulus, $J_E(t)$ is the creep compliance related to Young's modulus, μ is the Poisson ratio, δ_0 is the hold indentation value, and F_0 is the hold force value.

2.1.5 Frequency domain microrheological measurements

In the frequency domain, sinusoidal modulations are applied to the piezoelectric scanner perpendicularly to the sample surface (i.e., in the so-called Z direction) while the cantilever indents the sample [75]. When the cantilever is in contact with a hard surface and it is excited harmonically, the deflection signal and the sinusoidal signal are in phase. When the cantilever is embedded in a viscous material, a maximum level of deflection is reached when moving fast through the fluid-like environment. It causes the excitation and the deflection to be out of phase. Analyzing the phase shift ($\Delta\phi$) among these signals makes it possible to determine if a material behaves more like a solid or a fluid. The phase shift value is always between 0 and 90. For a purely elastic material, the phase shift is 0; for a purely viscous material, it is 90.
Figure 2.5 schematically illustrates the cantilever deflection in time during frequency modulation.

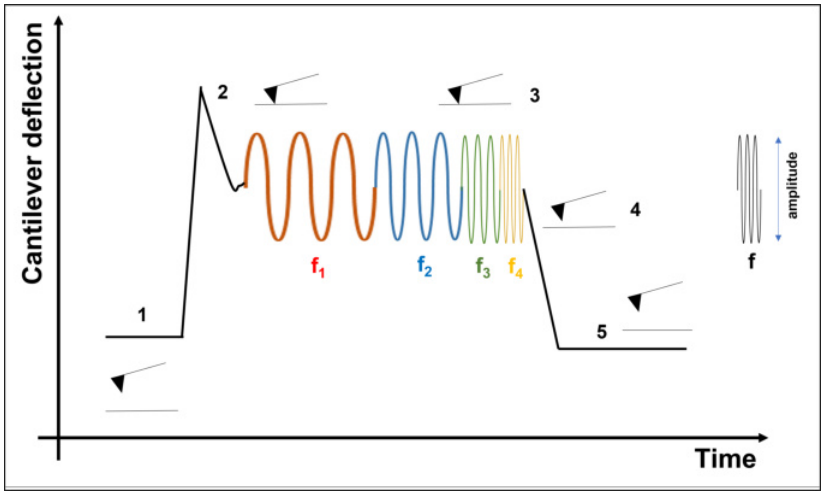

Figure 2.5: **An example of a force curve showing the bending of the cantilever in time during frequency modulation.** The force increases until the cantilever touches the sample surface (from 1 to 2). Once the cantilever indents the sample, an oscillatory movement is carried out with the desired frequency range. The example illustrates four frequency ranges (f1 -f4) at a constant amplitude. During the oscillation, the probing tip is always in contact with the sample (from 2 to 3). After this, the cantilever is retracted from the sample surface (4) and the force becomes zero like before (5) when the cantilever is far from the sample surface.

In the AFM frequency modulation mode, the force increases until the chosen trigger point when the cantilever touches the sample surface. Once the cantilever indents the sample at a certain indentation depth δ_0, an oscillatory movement $\delta(\omega)$ is carried out at the given δ_0 with the desired frequency range. During the oscillation, the probing tip is always in contact with the sample. After this, the cantilever is retracted from the sample surface, and the force becomes zero like before. The amplitude of the oscillation is kept constant during the whole experiment.
Both the indentation $\delta(t)$and the force $F(t)$ can be described as sinusoidal functions of time at the given angular frequency:

$$\delta(t) = \delta_0 + \delta_A \sin \omega t \tag{2.15}$$

$$F(t) = F_0 + F' \sin \omega t + F'' \cos \omega t \tag{2.16}$$

where δ_0 and F_0 are the working indentation and force.

The storage modulus E' and the loss modulus E'' of material are respectively

proportional to the sine (in-phase) and cosine (out-of-phase) of the phase angle, and together they describe the complex modulus [75]

$$E^* = E' + iE'' \tag{2.17}$$

where i is the complex unit.
To obtain the values of the two moduli, the analysis from the sinusoidal oscillations done by AFM requires the Fourier transform of the force and indentation at the angular frequency ω ($=2\pi f$), which gives:

$$F(\omega) = F_A e^{i\phi_F} \tag{2.18}$$

$$\delta(\omega) = \delta_A e^{i\phi_\delta} \tag{2.19}$$

Dividing equation 2.18 by equation 2.19, the ratio $F(\omega)/\delta(\omega)$ can be written as follows:

$$\frac{F(\omega)}{\delta(\omega)} = \frac{F_A}{\delta_A} e^{i\Delta\phi} = \frac{F_A}{\delta_A}(cos\Delta\phi + isin\Delta\phi) \tag{2.20}$$

,where the phase shift between force and indentation is:

$$\Delta\phi = \phi_F - \phi_\delta \tag{2.21}$$

Force and indentation depth for four-sided pyramidal tip are related as follows [76]:

$$F = \frac{3Etan\theta}{4(1-\mu^2)}\delta^2 \tag{2.22}$$

For small oscillations around the indentation δ_0, the equation 2.22 can be approximated by the first term of the Taylor expansion [77], which allows to obtain the expression for elastic modulus [75]:

$$E = \frac{2(1-\mu^2)}{3\delta_0 tan\theta}\frac{F_A}{\delta_A} \tag{2.23}$$

From equations 2.20 and 2.23, the complex modulus for a pyramidal indenter with a half-open angle θ can be calculated with the following equation (assuming $\delta_A \ll \delta_0$):

$$E^* = E' + iE'' = \frac{2(1-\mu^2)}{3\delta_0 \tan\theta}\frac{F_A}{\delta_A}(\cos\Delta\phi + i\sin\Delta\phi) \tag{2.24}$$

From the equation above, the elastic storage *E'* and loss *E"* modulus can be determined:

$$E'(\omega) = \frac{2(1-\mu^2)}{3\delta_0 \tan\theta} \frac{F_A}{\delta_A} \cos\Delta\phi \tag{2.25}$$

$$E''(\omega) = \frac{2(1-\mu^2)}{3\delta_0 \tan\theta} \frac{F_A}{\delta_A} \sin\Delta\phi \tag{2.26}$$

Knowing the relation between the elastic modulus and the shear modulus:

$$G = \frac{E}{2(1+\mu)} \tag{2.27}$$

the dynamic shear moduli can be calculated:

$$G'(\omega) = \frac{1-\mu}{3\delta_o \tan\theta} \frac{F_A}{\delta_A} \cos\Delta\varphi \tag{2.28}$$

$$G''(\omega) = \frac{1-\mu}{3\delta_o \tan\theta} \frac{F_A}{\delta_A} \sin\Delta\varphi \tag{2.29}$$

Transition frequency

The loss tangent, the ratio between *G"(ω)* and *G'(ω)*, can be used as a parameter to describe the solid-like or fluid-like behavior of a material. Along with this, another parameter used in this study to describe the viscoelastic properties of cells is the transition frequency, the frequency at which the storage modulus is equal to the loss modulus. Figure 2.6 shows a schematic illustration of a typical storage and loss modulus trend in relation to the oscillation frequency.

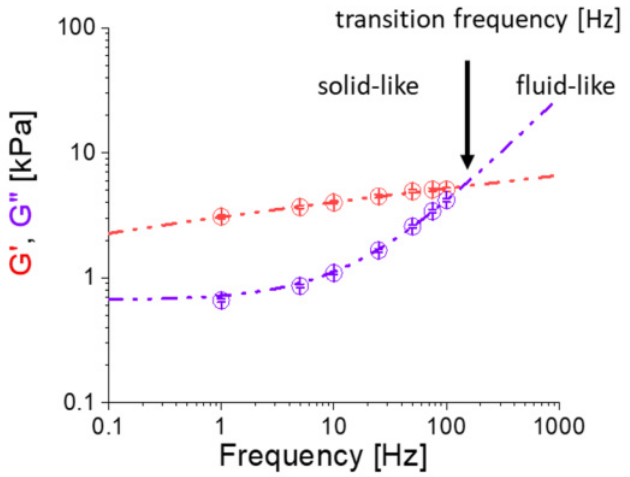

Figure 2.6: **Example of storage *G'* and loss *G"* moduli plotted as a function of the oscillation frequency.** Each point denotes the experimental data, and the dash-dot lines correspond to the power law fit (storage modulus in red and loss modulus in purple). The plot is in log scale, and the transition frequency, where the two moduli are equivalent, is indicated.

The transition frequency has been used to differentiate a more solid-like or fluid-like material, and recently few studies applied this parameter to describe the viscoelastic properties of biological elements like cells [128].

2.2 Hydraulic Force Spectroscopy

2.2.1 Micropipette aspiration - principles

Micropipette aspiration (MPA) is a technique widely used to investigate the physio-pathological properties of cells [108]. The traditional MPA system is composed of a micropipette (or microcapillary) having an internal radius R, connected to a water reservoir or a pump, which generates a suction pressure ΔP due to the difference in height between the tip of the micropipette and the top position of the reservoir h. Knowing the specific weight of the water ρg, ΔP can be determined as:

$$\Delta P = \rho g h \tag{2.30}$$

By changing the pressure, it is possible to capture and release the sample, and the aspirated length, which undergoes an increasing pressure in time, is monitored by using an optical microscope.

The main limitations of this technique are the followings. First, the spatial resolution is limited to the camera resolution connected to the microscope. Second, measuring small deformations is not feasible because of the projection errors introduced by the lack of plate/capillary parallelism. And third, the data analysis process may be complicated and computationally challenging due to the post-processing of the acquired images. To overcome these limitations, a novel MPA system was developed by M. Berardi et al., the hydraulic force spectroscopy [130].

2.2.2 System design

Hydraulic Force Spectroscopy (HFS) is a type of micropipette aspiration (MPA) technique that overcomes the limitations caused by the traditional MPA by using an interferometric optical readout method. It allows the analysis of the mechanical properties of biomaterials at the nanoscale level by making real-time measurements of both pressure and displacement [130]. Figure 2.7 illustrates the main components of the HFS system.

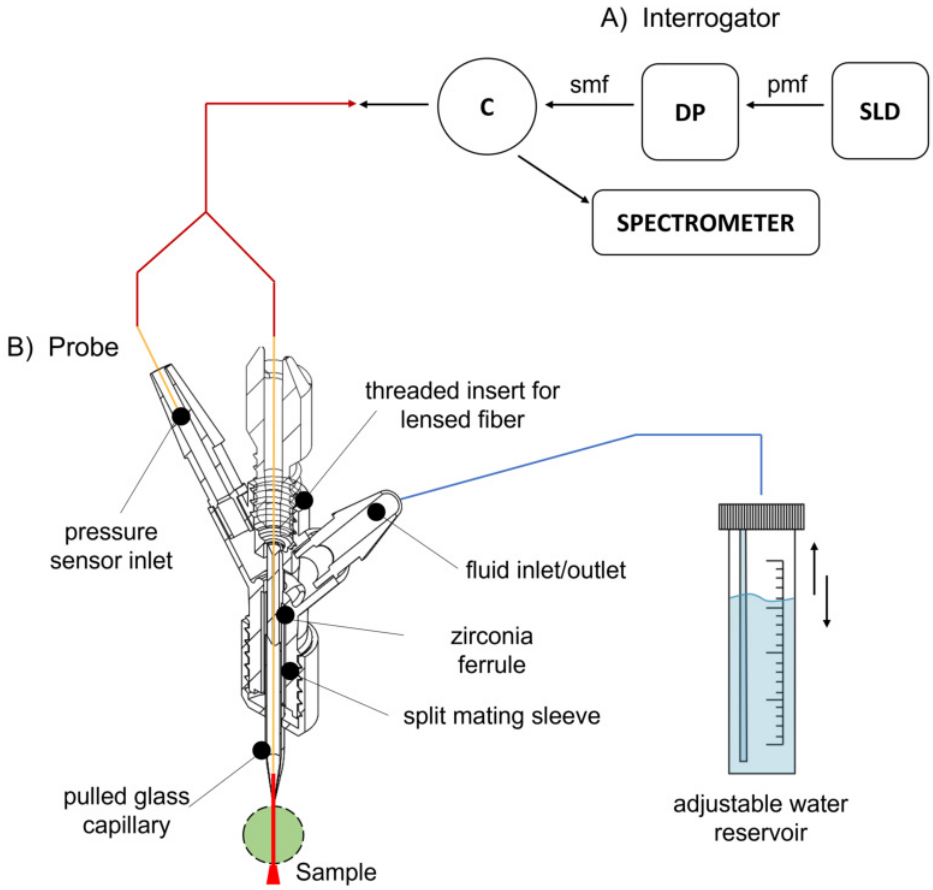

Figure 2.7: **Schematics of the HFS setup.** A) Optical interrogator: a superluminescent diode (SLD) is connected through a Panda fiber (pmf) to a depolarizer (DP), which is joined to a circulator (C) via a single mode fiber (smf). B) Cross-section of the probe: the pressure variation is induced by the change in the height of the water reservoir.

The HFS system comprises three fundamental parts: an interrogator, an interferometric displacement sensor, and a pressure sensor. The optical interrogator is made of a superluminescent diode (SLD), a polychromatic light source that illuminates the sample aspirated by the probe and the pressure sensor membrane. The SLD is connected to a depolarizer linked to a circulator that redirects the reflected light beams to the optical spectrometer. The pressure variation is obtained by either adjusting the height of the water reservoir or using a syringe pump. Figure 2.8 illustrates the pressure variation during the measurements.

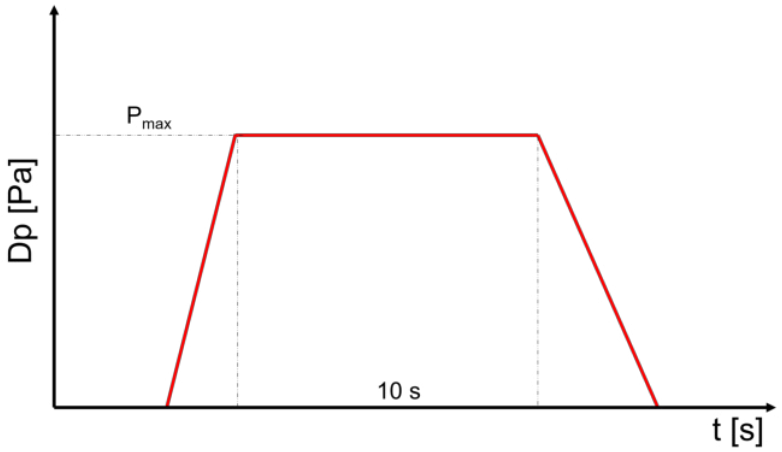

Figure 2.8: **Suction profile of the sample.** A very small pressure is applied to capture the sample, then a ramp of 100 Pa/s is applied, until reaching the maximum value of the pressure (1 kPa) which is kept for a few seconds, and finally there is the release of the sample.

The suction profile has a trapezoidal shape. A small negative pressure is applied to capture the sample while making the measurements. Once the sample is captured, a ramp of 100 Pa/s is applied, followed by a pause of 10 s at the highest pressure reached (1500 Pa), ending with a symmetric release.

2.2.3 Determination of elastic modulus by HFS

To obtain the readout from the optical system installed in HFS, two optical cavities are analyzed:

1. the cavity formed between the aspirated surface of the sample and the ending of the sample fiber;

2. the cavity formed by the membrane of the pressure sensor and the fiber of the pressure sensor.

The system is designed so that these two cavities have different lengths so that their interference pattern can be investigated individually. Afterward, by applying the Fourier transform and studying the phase variation of the optical cavities, it is possible to obtain the displacement value and the aspirated range of the sample.
The elastic modulus was determined by applying a modified linearized version of the Zhou model [131] [132]:

$$E = \frac{3R_p}{\beta_1 \left[1 - \left(\frac{R_p}{R_c}\right)^{\beta_3}\right]} \cdot \frac{\Delta P}{L_p} \tag{2.31}$$

where E is the elastic modulus, ΔP is the differential pressure, L_P is the aspirated length, R_P is the radius of the pipette, R_C is the radius of the aspirated sample, β_1 is equal to 2.0142 and β_3 is equal to 2.1187.

2.2.4 Dynamic mechanical analysis (DMA)

The most important feature of this system that makes it different from the other traditional MPA techniques is that it allows viscoelasticity measurements by dynamic mechanical analysis (DMA) that applies a sinusoidal oscillation at different frequencies. It is possible by attaching the same light source to the pressure and the displacement sensors, enabling the registration of the excitation signal and the material response in one single interferogram. To calculate the storage modulus and the loss modulus, parameters that describe the viscoelastic properties of the sample, again the Zhou model [131] was used. From the sinusoidal oscillations at a given angular frequency ω, the pressure and the length of aspiration can be expressed in relation to the time as follows:

$$P(t) = P_0 \sin(\omega t + \delta_P) \tag{2.32}$$

$$L_P(t) = L_0 \sin(\omega t + \delta_L) \tag{2.33}$$

where δ_P and δ_L are the phase shifts of the amplitudes that refers to the pressure and length oscillations.
By applying the trigonometric rules and using exponential notations, the storage and loss moduli can be determined with the final equations below:

$$L_P(t) = L_0[\sin(\omega t)\cos(\delta_L) + \cos(\omega t)\sin(\delta_L) \tag{2.34}$$

Storage modulus:

$$E' = \frac{3R_P}{\beta_1 \left[1 - \left(\frac{R_p}{R_c}\right)^{\beta_3}\right]} \cdot \frac{P_0}{L_0} \cdot \cos(\delta) \tag{2.35}$$

Loss modulus:

$$E' = \frac{3R_P}{\beta_1 \left[1 - \left(\frac{R_p}{R_c}\right)^{\beta_3}\right]} \cdot \frac{P_0}{L_0} \cdot \sin(\delta) \tag{2.36}$$

2.2.5 Time domain viscoelasticity

The viscoelastic characterization in the time domain can be performed by using the Boltzmann hereditary integral approach. Specifically, the samples are subjected to a ramp-and-hold suction profile:

$$P(t) = \begin{cases} Q \cdot t & \text{for } t \leq t_r \\ Q \cdot t_r & \text{for } t > t_r \end{cases} \tag{2.37}$$

where t_r is the ramp time, typically around 6 s, and Q is the rate of pressure change, approximately 50-60 Pa/s.

As the experiment is in pressure control, it is convenient to define the material creep compliance function $J(t)$. In this case, we assumed the samples exhibit power-law viscoelasticity. This translates into:

$$J(t) = A \cdot t^{\alpha} \tag{2.38}$$

where A is measured in $1/(\text{Pa}\cdot\text{t}^{\alpha})$, and α is a number. The latter can be interpreted as a "fluidity" index of the material: if $\alpha = 0$, the material is purely elastic, and A is its fractional compliance. Conversely, if $\alpha = 1$, the material behaves purely viscously. For a suction experiment, the relationship between aspirated length L_p and applied pressure in time is:

$$\begin{aligned} L_p(t) = & \frac{\beta_1 \cdot (1 - (R_p/R_c)^{\beta_3})}{3} \cdot R_c \cdot \\ & \cdot \int_0^t J(t-\xi) \frac{\mathrm{d}P(\xi)}{\mathrm{d}\xi} \, \mathrm{d}\xi \end{aligned} \tag{2.39}$$

with $\beta_1 = 2.0142$, $\beta_3 = 2.1187$, R_p is the pipette radius, R_c is the sample radius, and ξ is the dummy time variable [131]. By inserting equations 2.37 and 2.38 in equation 2.39, and solving the integral, the following equation is obtained:

$$L_p(t) = \begin{cases} -kAQ \cdot \frac{t^{\alpha+1}}{\alpha+1} & \text{for } t \leq t_r \\ -kAQ \cdot \frac{t^{\alpha+1} - (t-t_r)^{\alpha+1}}{\alpha+1} & \text{for } t > t_r \end{cases} \tag{2.40}$$

where, for conciseness $k = (\beta_1 \cdot (1 - (R_p/R_c)^{\beta_3})) \cdot R_c/3$.

Aims of the thesis

Oncogenic transformation is known to be associated with the mechanical and rheological properties of cells [67] and the rearrangements in the actin cytoskeleton [133] [134]. Cells *in vivo* grow next to each other and continuously exchange signals with the neighboring cells. Tumors have an altered tissue tensional homeostasis due to differences in rheology and increased cell-generated force [135]. During cancer progression, the cell signaling pathways are deregulated to resist apoptosis and invade the surrounding tissues [136]. This implies that cells, when cultured *in vitro* as single non-confluent cells and cells in monolayer, may exhibit different mechanical properties and rearrangement of the actin cytoskeleton [137]. Nowadays, 3D cell cultures, such as multicellular spheroids, are widely used to better mimic the physiological environment of cells in solid tumors [46].

The first main aim of this study was to elaborate on how mechanical and microrheological properties of bladder cancer cells, mimicking the transition from non-malignant to invasive bladder cancer, change when they are cultured as single cells, monolayers, and spheroids. For this purpose, different cell lines from the three stages of bladder cancer were chosen, i.e., non-malignant cell cancer of ureter HCV29 cells, high-grade transitional cell carcinoma T24 cells, and grade III carcinoma HT1376 cells. Each cell line is characterized by different actin cytoskeletal organizations, which play a key role in cell deformability. Thus, it was assumed that the actin filaments contribute significantly to the cellular mechanical/rheological responses regardless of the culture conditions. Moreover, the driving hypothesis was that the single-cell mechanics could be translated into spheroid mechanics by maintaining the relationship between the non-malignant and cancerous cell lines. The mechanical and microrheological properties of all samples were measured with the atomic force microscope (AFM).
As there are not many studies about the spheroid mechanics evaluated by AFM, to validate the application of this technique on 3D cultures, a preliminary study was conducted on spheroids formed from lung cells, i.e., healthy lung fibroblasts (NHLF) and small-lung cancer cells (A549) characterized by a well and poorly differentiated actin cytoskeleton, respectively.

The second major goal of the presented work was to investigate whether cells change their biophysical properties during cancer progression and how this relates to the internal structure of the spheroids. The mechanical and microrheological properties of the spheroids formed from bladder cell lines (HCV29, T24 and HT1376) were analyzed after 3 days of culture to mimic the early stage of tumor,

and after 14 days of culture to mimic a late growth phase of the tumor. AFM and hydraulic force spectroscopy (HFS), respectively at the nanoscale and macroscale levels, were applied to study the age-related changes on the mechanical properties of spheroids.

Lastly, as cancer therapy remains one of the biggest challenges due to the development of drug resistance against antitumor agents [138] and knowing that mechanical properties of cells can be used as a possible biomarker for cancer detection [58], hereby the alterations in the spheroid mechanics were analyzed by HFS after the treatment with docetaxel (DTX), an anticancer drug targeting the microtubules. Therefore, the final goal of this study was to verify whether the 3D multicellular spheroids could really be a good model to mimic the different stages of bladder cancer and whether the mechanical properties of cells detected with HFS could be a useful marker to assess the effects of anticancer drugs.

Part II

Materials and Methods

Chapter 3

Biological methods

3.1 Cell lines

3.1.1 Bladder cancer cells

In this study, three human bladder cancer cell lines were used: HCV29, T24 and HT1376 cells. HCV29 cells are adherent non-malignant epithelial cells derived from a male adult patient suffering from bladder carcinoma([111]). The STR profile of HCV29 cell line is the following: amelogenin: X,Y; TH01: 6,8; D13S317: 8,11; D16S539: 12,13; D5S818: 12; D7S820: 7,12; TPOX: 8,12; vWA: 19,21; CSF1PO: 11,12. The STR profile of HT1376 cell line: amelogenin: X; TH01: 7,10; D13S317: 9,11; D16S539: 11,14; D5S818: 11,12; D7S820: 9,12; TPOX: 8; vWA: 15,18; CSF1PO: 12. The STR profile of T24 cell line is: X; TH01: 6; D13S317: 12; D16S539: 9; D5S818: 10,12; D7S820: 10,11; TPOX: 8,11; vWA: 17,19; CSF1PO: 10,12. These cells were derived from the ureter. T24 and HT1376 cells were obtained from grade III urinary bladder cell carcinoma (ATCC, LGC Standards), but T24 cells were from a patient suffering from transitional cell carcinoma, which is more invasive than bladder carcinoma, represented by HT1376 cells [139].
HCV29 and T24 cells were cultured in RPMI-1640 medium (Sigma) supplemented with 10 % Fetal Bovine Serum (FBS, Sigma). HT1376 cells were cultured in Eagle's minimum essential medium (EMEM, LGC Standards) with 10 % FBS. All cell lines were grown in culture flasks (Sarstedt) in an incubator (Nuaire) at 37° C in 5 % CO_2. The relative humidity was kept above 98 %. The cell passaging was carried out when they reached 80-90 % of the confluency level. For HCV29 and T24 cells, 0.05 % and for HT1376 cells, 0.25 % of trypsin-EDTA solution (Sigma) was applied to detach cells from the culture flask surface.

3.1.2 Lung cells

In addition to bladder cancer cell lines, two human lung cell lines were studied here: NHLF and A549 cells. NHLF is a human lung fibroblast (Lonza) and A549 are cells from a human small-lung cancer (ATCC). NHLF cells were cultured in FBM + FGM-2 medium (Sigma) and A549 cells were cultured in F12K medium (Sigma), both supplemented with 10 % FBS. To detach these cells from the culture flask, 0.25 % of trypsin-EDTA solution was used.

3.2 Spheroid culture

Spheroids were prepared in 96-well U-bottom 3D cell culture plates (Thermofisher). Cells were seeded in 150 μL of suitable culture medium in each well. Depending on the cell line, the number of cells/well was adjusted to obtain spheroids of 350-400 μm diameter. After cell passage, cells were counted by using Burker chamber and the exact number of cells was seeded in each well. The spheroids were formed after 3 days of incubation. Spheroids were prepared in the respective culture medium suitable for each cell line. Table 3.1 show the cell numbers per well for each cell line.

Table 3.1: *Number of cells per well required to form spheroids with a diameter of 350-400 μm*

Cell type	***Cells per well***
HCV29	6000
T24	10000
HT1376	1200
NHLF	1800
A549	1500

To study the aging effect, the spheroids culture was set to 14 days.

3.3 Drug treatment

3.3.1 Cytochalasin D

Cytochalasin D (cyto-D) was purchased as a powder (Sigma - Aldrich, molecular weight = 507.6 g/mol) and diluted in DMSO to prepare a stock solution of 100 μM concentration.
Cells and spheroids were respectively cultured in Petri dishes (single cells and cell

monolayers) and U-bottom well plates (spheroids). On the day of measurements, the culture medium was removed and Phospate Buffer Saline (PBS, Sigma) containing 5 μM cyto-D (1:20 dilution from the stock solution) was added. The samples were kept at 37°C for 30 minutes in the incubator. Afterwards, cyto-D was removed and samples were carefully washed with fresh PBS buffer.

3.3.2 Docetaxel

Docetaxel (DTX, Sigma - Aldrich, molecular weight = 807.9 g/mol) was purchased as a powder and dissolved in 99.8 % ethanol (Sigma - Aldrich) at a final concentration of 1 μM. The stock solution was diluted in the cell culture medium at the desired concentration. Docetaxel was added to spheroids in the following manner. After 3 days of growth, spheroids from HCV29, T24 and HT1376 cells were treated with DTX by adding a fresh media containing DTX (concentrations ranging from 1 nM to 1 μM) and leaving the spheroids in the culture (in the CO_2 incubator) for 24 and 72 hours.

3.4 Cell viability test: MTS

To determine the cell viability of the bladder cancer cell lines, an MTS assay was performed by using CellTiter 96 AQueous One Solution Cell Proliferation Assay (Promega, G3582). In 24-well plate, a suitable amount of cells (10000-20000) was seeded in each well, and after one day of incubation, a fresh culture medium was added. The coulorimetric measurements were performed by using a spectrometer (ELISA SPECTROstar NANO, BMG LABTECH), and the absorbance was determined at 490 nm.
The same MTS assay was carried out to test the cytotoxicity of DTX on spheroids. Ten spheroids were prepared for each concentration for each bladder cell line. After three days of incubation, the cell culture medium was replaced with a fresh medium containing the DTX at the following concentrations:

- HCV29: 0, 5, 20, 100, 250, 500, 1000 [nM]
- T24 and HT1376: 0, 5, 20, 100, 250, 500 [nM]

Afterwards, the spheroids were incubated with the drugs for 24 hours. Subsequently, the samples were used for colorimetric measurements with the same spectrometer, and the absorbance was determined at 490 nm.

3.5 N/E-cadherin expressions

3.5.1 SDS - PAGE

Spheroids were prepared from HCV29, T24, and HT1376 cells, and for each cell line, 10000 cells/well were seeded in 20 U-bottom wells. After three days of incubation, the spheroids were ready to be collected and they were washed in PBS and dissolved in 10 μl of solubilizer, which was prepared by dissolving in water 1M TRIS-HCL pH 6.8, Sodium Dodecyl Sulfate (SDS), glycerol and 2-Mercaptoethanol. Following this, all the solutions containing the spheroids were heated at 95° C for 5 minutes. Then, the samples were sonicated by using an ultrasonic homogenizer (BioLogics Model 300 V/T) three times at intervals of 5-10 seconds. The protein concentration in the lysate was read by using a fluorimeter (Invitrogen Qubit, Thermo Fisher Scientific). For each sample, 20 mg of protein was loaded in polyacrylamide gel for electrophoresis (4-15 % Mini-PROTEAN Gels, BioRad) and run in electrode buffer (10x Tris/Glycine/SDS, BioRad). The electrophoresis was conducted at a voltage of 60 V for 20 minutes and then at 120 V for a couple of hours.

3.5.2 Western Blot and immunodecoration

After the SDS-PAGE, the proteins were transferred from the gel to a polyvinylidene difluoride (PVDF) blotting membrane using a transfer buffer (10x Tris/Glycine Buffer for Western Blots, BioRad). A wet transfer was performed at 4°C overnight at a constant electric field of 15 mA.
To prevent non-specific background bindings, the membrane was incubated in a blocking solution containing 3% of Bovine Serum Albumin (BSA) solution for 3 hours at 4°C under gentle agitation and then washed three times in TBS/Tween20 (TBST) buffer (Sigma Aldrich). Afterwards, the membrane was incubated with the primary antibodies N-cadherin (mouse monoclonal [8C11] to N-Cadherin, ThermoFisher) and E-cadherin (E-cadherin Monoclonal Mouse clone NCH-38, DAKO), in blocking solution (TBST) overnight at room temperature and washed again in TBST buffer.
Finally, the presence of the protein bands was verified by using a secondary antibody (anti-Mouse IgG (whole molecule)-Alkaline Phosphatase antibody).

3.6 G/F-actin determination

The G-actin/F-actin In Vivo Assay Kit (cat. BK037, Cytoskeleton) was used to determine the F/G-actin ratio. Cells were grown at a high density in their culture flasks and homogenized in 300 μl of LAS2 buffer (LAS2 contains detergents disrupting the cell membrane). The cell lysates were collected and centrifuged at 100.000 x g at 37° C for 1 h, separating a soluble G-actin (supernatant) from the polymerized F-actin (pellet). The ultracentrifuge was accessible at the Department of Physical Biochemistry, Faculty of Biochemistry, Biophysics and Biotechnology, Jagiellonian University.
The collected supernatants were separated on 10 % SDS-PAGE gels and transferred onto a PVDF blotting membrane. Here, an anti-actin rabbit polyclonal antibody, provided along with the kit (Cytoskeleton), was used to detect G- and F-actins. Bands were visualized using horseradish peroxidase-coupled secondary anti-rabbit antibody (Cell Signaling Technology). The ratio between G/F actin was determined by using Image J - based densitometric calculation.

3.7 Histology of spheroids

3.7.1 Paraffin embedding

Spheroids were prepared as described in section 3.2 and after 3 or 14 days of incubation, they were collected in 1.5 ml Eppendorf tube for the histological analysis. They were fixed with 10 % neutral buffered formalin (Sigma) for 15 minutes. Then, they were dehydrated in a series of alcohol solutions dissolved in water: 50 %, 80 %, 96 % and 100 %. Each of these steps was done for 15 minutes. Afterwards, the samples were treated with Xylene (Sigma). Once all the xylene was completely removed, the spheroids were embedded in paraffin blocks. The samples were cut into 6 μm serial sections by using a microtome (Microtome Biocut 2035; Leica Instruments GmbH) and mounted on poly-lysine-coated slides (Menzel-Glaser; Thermo Scientific).

3.7.2 Immunostaining

The spheroid sections were deparafinized and stained using histochemical methods:

- Hematoxylin and Eosin (H&E, Sigma-Aldrich) to stain the cell nuclei (purplish blue) and the extracellular matrix and cytoplasm (pink).

- Masson's trichrome (MT) distinguishes cells from the surrounding connective tissue (blue). This is a three-colour staining that uses: *(I)* hematoxylin solution, Harris modified, to stain the nuclei; *(II)* a plasma staining solution containing 1 % acid fuchsin, 1 % xylidine ponceau, 1 % glacial acetic acid and distilled water; *(III)* a solution containing 1 % phosphomolybdic acid and 2.5 % methyl blue in distilled water to stain collagen. All components were purchased at Sigma-Aldrich.

- Sirius red (SR) stains the collagen type I and type III (red). Slides were stained with 0.1 % picro-sirius red (Sigma-Aldrich) in saturated acqueous solution of picric acid, washed in 0.5 % acetic acid, dehydrated, cleared and mounted in resin.

3.8 Cryosection of spheroids

T24 spheroids were prepared as described in section 3.2, and after 3 and 14 days of incubation, they were ready for cryosection. Spheroids were mixed with an optimal cutting temperature compound (OCT, ThermoFisher) and frozen at - 80°C. The frozen samples were then cut into 20 μm serial sections at -20°C by using a cryostat (Leica Biosystems) present in the Urological Research Institute (URI) of Ospedale San Raffaele, Milano -Italy, and finally mounted on poly-L coated slides.

3.9 Epi-fluorescence Images

Cells were cultured in Petri dishes at the density of single cells and monolayers. The culture medium was removed and the cells were washed with PBS buffer before the fixation procedure. Cells were fixed with 3.7 % paraformaldehyde solution in PBS for 20 minutes. After this, they were washed with PBS three times, and the cell membrane was permeabilized using 0.2 % Triton X-100 (Sigma) in PBS at 4° C for 5 minutes. Following this, the cells were rinsed with PBS and they were labelled with fluorescent dyes in a dark environment. For visualizing the actin filaments, cells were stained with Phalloidin conjugated with Alexa Fluor 488 (Invitrogen) dissolved in PBS buffer (1:200) for 30 minutes, while the cell nuclei were stained with Hoechst 33342 (Invitrogen) dissolved in PBS buffer (1:5) for 15 minutes. Finally, the samples were washed with PBS buffer and were ready for imaging.
The fluorescent images were recorded using an Olympus IX83 inverted microscope

(Olympus, Japan) equipped with a 100 W mercury lamp and a set of filters used to record the emission at 515-545 nm (Alexa Fluor 488) and 461 nm (Hoechst 33342).
The images were acquired using the Orca Spark digital camera (Hamamatsu, Japan), providing 2.3 megapixels (1920 pixels per 1200 pixels) images that were recorded using CellSens Dimension software (Olympus).

3.10 Confocal Imaging

Confocal images of actin filaments and microtubules inside spheroids were visualized using a confocal microscope, accessible in the Laboratory of *in vivo* and *in vitro* imaging, Maj Institute of Pharmacology, Polish Academy of Sciences. The samples were stained using the following protocol. Spheroids from each cell line were collected in a 1.5 ml Eppendorf and fixed with 3.7 % paraformaldehyde for 1 hour. Following this, the samples were washed with PBS for 2 minutes three times, treated with 1 % cold Triton X-100 overnight at 4°C, and washed again with PBS. Then, 1 % cold BSA solution was added for 3 hours at 4°C, and after removing BSA, the spheroids were washed with PBS. Next, the spheroids were incubated overnight at 4°C with phalloidin conjugated with Alexa Fluor 488 (1:20 in PBS). The next day, the dye for actin filaments was removed, and either SiR-DNA (Spirochrome), diluted 1:1000 in PBS, or Hoechst 33342, diluted 1:5 in PBS, for the cell nuclei was added. The day after, after washing the samples with PBS, the dye for the microtubules, monoclonal anti-β-Tubulin-Cy3 (1:150 in PBS) was added. Finally, the samples were washed with PBS and moved to 18-well glass-bottom slides (Ibidi) with an anti-shading solution (Thermofisher) having the same refractive index (1.52) as the oil used for the objective of 63 X magnification. Images were recorded using a Leica TCS SP8 WLL confocal microscope equipped with new-generation HyD detectors and they were registered using an oil immersion 63x objective lens (HC PL APO CS2 NA 1.40).

3.11 Live/Dead staining

Live/Dead staining was performed on spheroids from bladder cancer cells, which were grown for 3 days and 14 days, and treated with DTX at different concentrations. A commercially available kit (Live/Dead Cell Double Staining Kit, Sigma) was used. The culture medium was removed and the spheroids were carefully washed with PBS. Then, PBS containing two solutions with calcein (for

live cells - green signal) and propidium iodide (for dead cells - red signal) was added. The samples were kept at 37° C for less than ten minutes and were ready for imaging. The fluorescent images were acquired by using an Olympus IX83 inverted microscope (Olympus, Japan) equipped with a 100 W mercury lamp and a set of filters used to record the emission at 490-515 nm (green) and 535-617 nm (red). The images were acquired using the Orca Spark digital camera (Hamamatsu, Japan), providing 2.3 megapixels (1920 pixels per 1200 pixels) images that were recorded using CellSens Dimension software (Olympus).

Chapter 4

Experimental methods

This study used two types of AFMs to measure the mechanical and microrheological properties of cells cultured as single cells, cell monolayers, and multicellular spheroids.
For the nanoindentation measurements of 2D cultures, a commercial AFM (Xe120 model, Park Systems, Korea) was mainly used. This microscope works in a force spectroscopy mode. For the study of mechanical properties of the spheroids and the microrheological measurements of all the samples, Nanowizard IV (Bruker - JPK Instruments) was used. Both AFMs are integrated with optical microscopes (Olympus IX71).

4.1 Sample preparation for AFM measurements

4.1.1 Single cells and monolayers

For the 2D culture measurements at two different confluency levels, i.e., single cells and cell monolayers, cells were seeded either on glass coverslips for the nanoindentation experiments conducted with the Park Systems AFM or on standard Petri dishes for the microrheological measurements with JPK AFM. In both cases, cells were prepared 24 hours before the day of the measurement. A fresh, corresponding to each cell line medium was added, and the AFM measurements were conducted for not longer than 2 hours per sample.

4.1.2 Spheroids

For the AFM measurements, the spheroids were prepared as described in section 3.2. They were measured after 3 days or 14 days of incubation. Both the

mechanical and microrheological measurements of spheroids were conducted by Nanowizard IV (JPK Instruments). Two methods were used to immobilize the spheroids during the AFM measurements (Fig. 4.1).

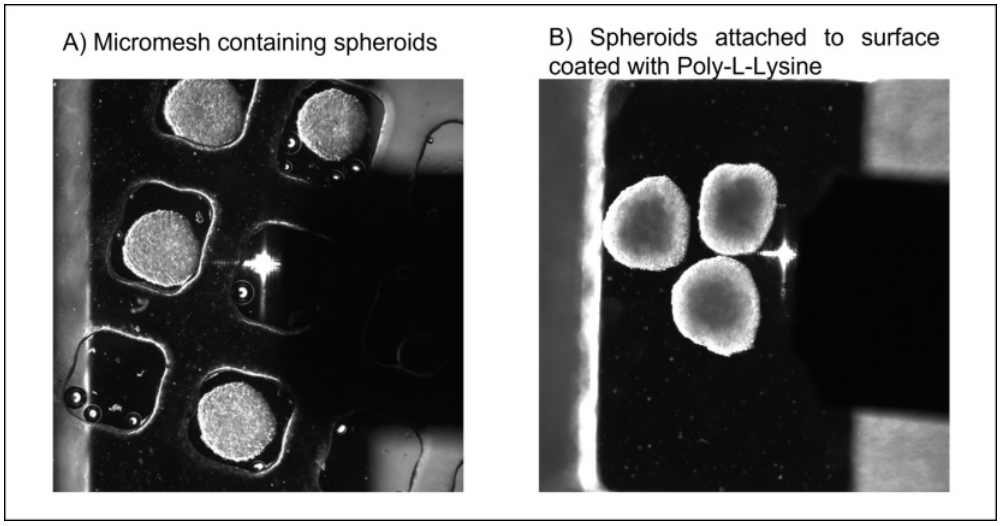

Figure 4.1: **Spheroids immobilization for AFM measurements.** A) Image showing the micromesh containing the spheroids during AFM measurements. B) Image showing spheroids immobilized on Petri dishes coated with poly-L-lysine.

In the first method (figure 4.1 A), a micromesh array (Microsurfaces, Australia) made of bio-compatible silicone polymer, composed of 500 μm length and 100 μm height wells, was used. Spheroids were collected from their culture plates and seeded in these wells. The size of the spheroids was around 400 μm in diameter, so they nicely fit in these wells.

In the second method (figure 4.1 B), spheroids were fixed in Petri dishes coated with 0.01 % poly-L-lysine and 5 % glutaraldehyde. The coating protocol is as follows. The Petri dish was washed with ethanol and let dry, then washed with water and dried again; it was covered with 5 % glutaraldehyde for 20 minutes and washed again with water. Finally, it was coated with 0.01 % poly-L-lysine for 30 minutes. After removing the poly-l-lysine, the Petri dish was left to get dry, and it was ready to be used. Afterwards, spheroids were collected from their culture plates and placed on the coated Petri dishes. Before starting the AFM measurements, the spheroids were left for 15-30 minutes to be attached to the surface.

4.2 Cantilever selection

The soft cantilevers for AFM measurements are typically made of silicon nitride, and they may have different forms and dimensions. In this study, several types of cantilevers were used.
In the case of the bladder cancer cell lines, two main types of pyramidal cantilevers were used, i.e., triangular MLCT and rectangular NSC36. Table 4.1 summarizes the main features of the cantilevers selected for the measurements.

Table 4.1: *Main parameters describing the cantilevers used for bladder cancer cells and spheroids.*

			Level		Tip geometry	
Cantilever type	Spring constant [N/m]	Frequency [kHz]	Length [µm]	Width [µm]	Height [µm]	Half-open angle
MLCT	0.03	15	225	20	4-6	20°
NSC36	0.6	65	130	32.5	12-18	20°

The choice of the cantilevers is critical to have good results, as they influence the signal-to-noise ratio, drift, and feedback response time. The smaller the cantilever spring constant, the better the noise-to-signal ratio. In addition, the resonance frequency of the cantilever limits the feedback response of the system. Therefore, a good probe must be stable in a time of a few milliseconds and must have a linear response in quite a large range of forces. For these reasons, the triangular MLCT cantilever was chosen. On the other hand, rectangular NSC36 cantilevers were chosen for the spheroids because they can produce deeper indentations on the sample due to the larger spring constant. The tips mounted on these two cantilevers have a half-open angle of 20°.
The value of the photodetector sensitivity is specific to the used cantilever. As described in section 2.1.1, it is necessary to determine this value for each cantilever. Here, MLCT cantilevers showed 47.13 ± 1.2 nm/V, and NSC36 cantilevers had 14.2 ± 1.4 nm/V.

Four different cantilevers were used in the AFM measurements carried out on lung cancer cell lines. These were triangular (MLCT) with pyramidal tip (open-angle 20°), rectangular tipless (Arrow-TL), and triangular (CP-PNP-BSG) with colloidal probes of radius 5 μm and 10 μm (Table 4.2).

Table 4.2: *Main parameters describing the cantilevers used for lung cancer spheroids measurements.*

			Level		Tip geometry	
Cantilever type	Spring constant [N/m]	Frequency [kHz]	Length [µm]	Width [µm]	Height [µm]	Half-open angle
MLCT	0.6	125	85	18	4-6	20°
Arrow-TL	0.03	6	500	100	no tip mounted	
CP-qp-CONT-BSG	0.1	30	125	35	Spherical probe of 5 µm radius	
CP-PNP-BSG	0.32	67	100	13.5	Spherical probe of 10 µm radius	

4.3 AFM measurements

4.3.1 Nanoindentation of bladder cancer cells

In the study of the mechanical properties of living bladder cancer cells, measured at the different levels of cellular organization, the AFM measurements were performed as follows. For the bladder cancer cells in 2D cultures (single cells and monolayers), force curves were acquired above the nuclear region in a region of 64 μm^2 and a total of 36 force curves were recorded per cell. The approach speed was set to 8 μm/s and the maximum load force was between 1-2 nN, and a maximum indentation of 1 μm. The indentation experiments were conducted at room temperature in liquid conditions, and 20 cells were measured for each set of measurements (3 times repeated). In the case of 3D culture, 15 spheroids were measured, with 2 maps per spheroid. Also, in this case, a region of 64 μm^2 in the central area of the spheroid and a total of 36 force curves were recorded per map. The force value was kept at 15 nN for the spheroids, giving a maximum indentation of 2.5-3 μm.

In the case of the mechanical properties of spheroids cultured at two different time points, the indentation measurements were conducted with NSC36 cantilever, at a load force of 30 nN, an approach speed of 10 μm/s, and for each map, the scan area was 100 μm^2 and a total of 64 force curves were recorded per map. The number of total maps varied between 30-40.
The force curves acquired with Park AFM (2D culture) were analyzed by using software developed at the Department of Biophysical Microstructures - IFJ PAN. The data acquired with the Nanowizard IV for the 3D culture were processed using the software provided by JPK.

4.3.2 Nanoindentation of lung cancer cells

The mechanical properties of lung cancer cells were measured only when they formed spheroids. Four different cantilevers were used for these experiments, and in all indentation measurements, the approach speed was 10 μm/s, and the load force was kept at 15 nN, except for the MLCT cantilever. In this case, both 15 nN and 5 nN force were applied to obtain deep and shallow indentations. For each set of measurements, 10 spheroids were measured and 3 maps per spheroid, for a total of 30 maps. A suitable scan area was chosen according to the contact area of the different cantilevers (100 - 900 μm^2). The acquired data were processed with the software provided by JPK, and Young's modulus value is expressed as mean $\pm$ standard deviation.

4.3.3 Young's modulus distributions

Young's modulus was expressed as a mean value for all the samples with the corresponding standard deviation for both 2D cells and spheroids. Figure 4.2 illustrates the distribution of Young's modulus in the bladder cancer cells, measured as single cells and monolayers.

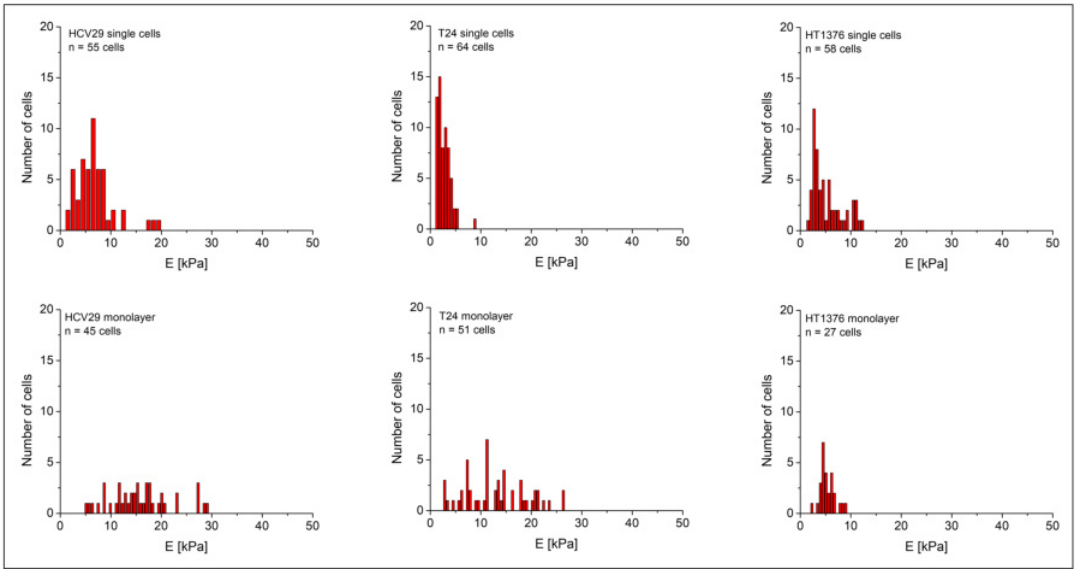

Figure 4.2: **Young's modulus distribution for bladder cancer cells (non-malignant HCV29, carcinoma HT1376, and transitional cell carcinoma T24 cells).** The average value was calculated for each recorded elasticity map denoting a single cell to obtain fully independent data. Then, the mean value and standard deviation were determined with such a dataset.

Similarly, Young's modulus distribution for the bladder cancer spheroids is shown

in figure 4.3.

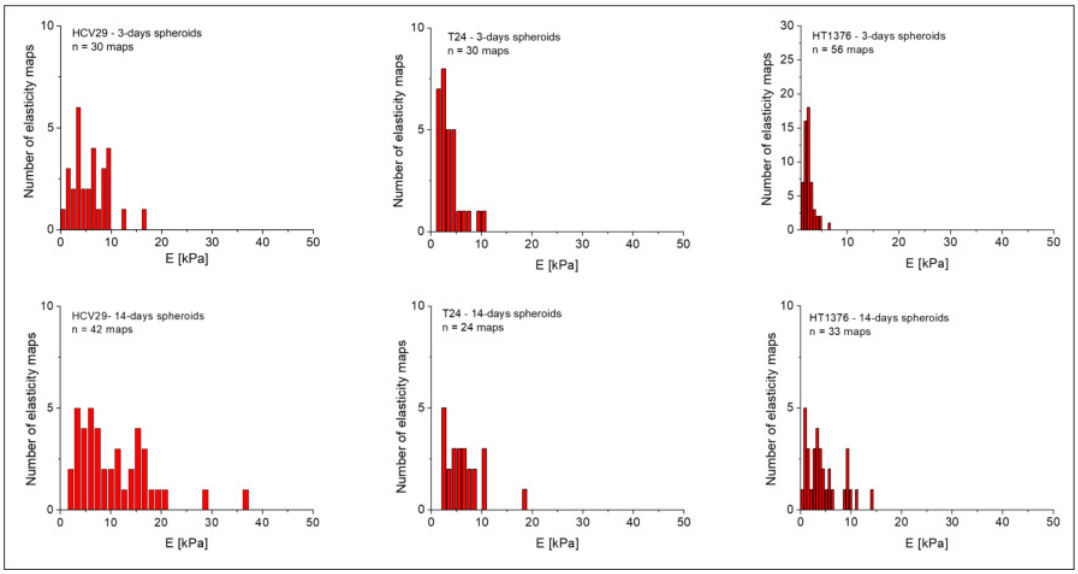

Figure 4.3: **Young's modulus distribution for bladder cancer spheroids (non-malignant HCV29, carcinoma HT1376, and transitional cell carcinoma T24 cells.** The average value was calculated for each recorded elasticity map denoting a place on a spheroid center to obtain fully independent data. Approximately, 15-20 spheroids were measured for each celll line. Then, the mean value and standard deviation were determined with such a dataset.

Considering each point from the dataset as independent measurements, the mean value and standard deviation of Young's modulus were determined.

4.3.4 Rigidity index

To quantify the obtained differences between the non-malignant and the cancer cells in the three culture conditions measured with two different cantilevers, the rigidity index R was defined as:

$$R = \log_{10} \frac{E_{cancer}}{E_{reference}} \tag{4.1}$$

The value of the rigidity index below 0 indicates the softening of the cells, while for values above 0, cell stiffening is detected. The rigidity index was also used to determine the difference between the spheroids formed by the NHLF fibroblasts and A549 lung cancer cells measured with the various cantilevers.

4.3.5 Microrheological measurements of bladder cancer cells and spheroids

The microrheological measurements were performed on bladder cancer cell lines both in 2D culture conditions and 3D spheroids. The general idea of the experiment is explained in chapter 2.
For the cells in 2D and for spheroids, MLCT cantilever and NSC36 cantilevers were used, respectively. The oscillation frequencies were from 1 Hz to 100 Hz for 2D cells, and from 1 Hz to 250 Hz for spheroids. The applied frequencies were: 1, 5, 10, 25, 50, 75, 100, 150 and 250 Hz. These frequencies were acquired with 10 periods/frequency and a pause of 500 ms between each frequency. The amplitude was kept constant at 50 nm; the sampling number was always 600 by adjusting the sample rate, the approach velocity was of 3 μm/s and the scan area was 9 μm^2. In the case of cells, the force limit was 2 nN, while for the spheroids, it was 15 nN (or 30 nN). An average of 50 cells were measured for each cell line and 15 spheroids (2 maps/spheroid).

4.3.6 Power-law relations

The acquired data were processed with the software provided by JPK, and the storage and loss moduli from every force map were calculated as the mean value for each frequency of oscillations. Figure 4.4 shows the exemplary distributions of the storage modulus determined for HCV29 spheroids at frequencies 1 Hz, 100 Hz and 250 Hz.

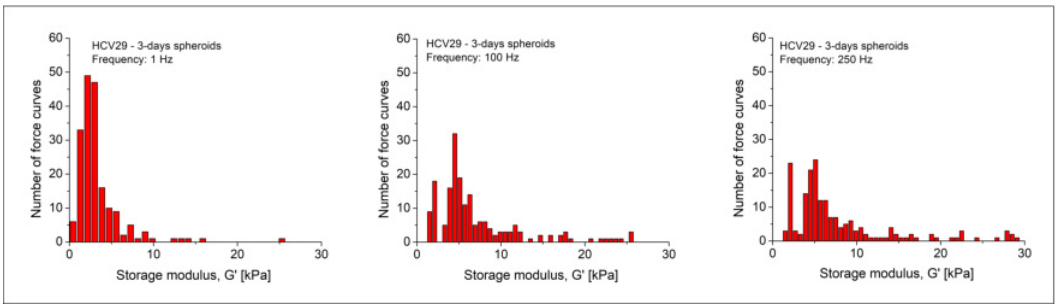

Figure 4.4: **Storage modulus distribution for spheroids formed by non-malignant HCV29 cells.** The average value was calculated for each recorded elasticity map denoting a place on a spheroid center to obtain fully independent data. Then, the mean value and standard deviation were determined with such a dataset.

Figure 4.5 shows the exemplary distributions of the loss modulus determined for HCV29 spheroids at frequencies 1 Hz, 100 Hz and 250 Hz.

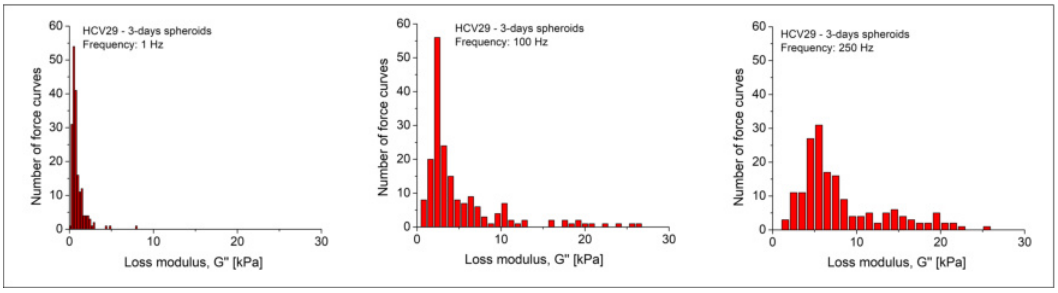

Figure 4.5: **Loss modulus distribution for spheroids formed by non-malignant HCV29 cells.** The average value was calculated for each recorded elasticity map denoting a place on a spheroid center to obtain fully independent data. Then, the mean value and standard deviation were determined with such a dataset.

The obtained mean values were used to plot the storage G' and loss G'' moduli as a function of oscillation frequency, and they were then modeled with the power-law approach (Abidine et al., 2015 [128]) by using the software OriginPro:

$$G'(\omega) = G'_N + k_1\omega^{\alpha} \tag{4.2}$$

$$G''(\omega) = G''_N + k_2\omega^{\beta} \tag{4.3}$$

The power-law exponent α obtained from the fitting of the storage modulus was used to describe the viscoelastic properties of the samples. While to determine the transition frequency, the frequency where storage modulus is equal to loss modulus, the software Mathcad 2001 was used.

4.4 HFS measurements

For the HFS measurements, spheroids were prepared in the same manner as for the AFM measurements (section 3.2). However, in this case, they did not require immobilization as the spheroids needed to be captured by the pipette for the HFS measurements. Thus, spheroids were collected from their culture wells and placed in a Petri dish. All the measurements were done in PBS.
The pipette used in this study had a diameter of 50 μm, while the spheroids were around 350-400 μm. Figure 4.6 shows how the pipette captured the spheroids during the measurements.

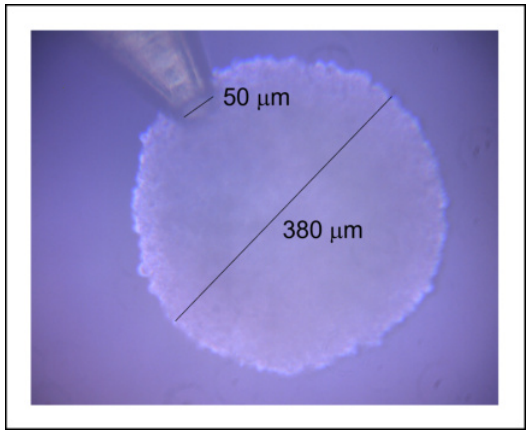

Figure 4.6: **HFS measurement of spheroids.** Optical image showing the capture of a spheroid formed by HT1376 cells with the pipette during HFS measurements.

Data from HFS were collected averagely on 10-15 spheroids. The experimental data were analyzed with Matlab. The values of Young's modulus and the viscoelastic parameters (fluidity index α and the fractional compliance A) were expressed as mean $\pm$ standard deviation.

4.5 Statistical tests

The statistical significance of the data sets was obtained by applying a non-parametric Mann-Whitney test at the significance level of 0.05. The mean value was calculated from each elasticity map, and then these data were used to create the box plots. Therefore, every single dot in the box indicates a single elasticity map. In the case of 2D cultures, one single map was recorded per cell, while for the spheroids, 2 maps were recorded per spheroid.

Part III

Results

Chapter 5

Mechanical properties of lung cell spheroids determined with different cantilevers

5.1 Objectives

Several studies have already reported on the effects of different types of cantilevers on the elastic properties of single cells. They have demonstrated that values of Young's modulus change depending on the cantilever type and geometric approximations needed in contact mechanics models [140] [141]. It is one of the main reasons contributing to the relativeness of Young's modulus [142]. As no data shows the analogous effect of the cantilever geometry on spheroid mechanical properties, AFM-based elasticity measurements were conducted on spheroids formed from lung cells, i.e., lung fibroblasts and lung cancer cells. This choice was dictated by large differences in the organization of the actin cytoskeleton in these cells. Healthy lung fibroblasts (NHLF) possess very well-differentiated actin filaments spanning the whole cell body. The fibroblasts are large cells with spindle-like morphology. Conversely, small-lung cancer A459 cells are much smaller with round morphology and a poorly differentiated actin cytoskeleton. Mechanical properties of spheroids formed from these cells were measured by employing AFM with the use of cantilevers possessing four different types of probing tip: four-sided pyramids (MLCT), large and small spheres, and no probing tip (so-called tipless cantilever) *[more details in section 4.2 of materials and methods]*.

5.2 Cytoskeletal organization of lung cell spheroids

In the first step, the actin cytoskeleton organization in spheroids formed by lung cancer cells (A549) and lung fibroblasts (NHLF) was visualized using confocal microscopy (figure 5.1).

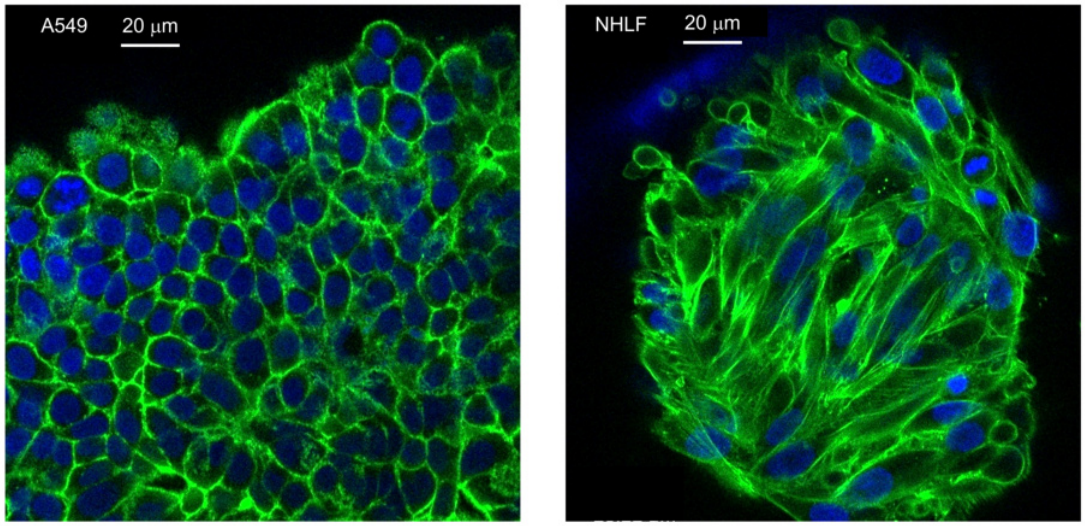

Figure 5.1: **Confocal images of A549 and NHLF spheroids.** The cellular structures present in spheroids formed by lung cancer cells (A549) and healthy lung fibroblasts (NHLF) are shown. Blue: nucleus, Green: actin filaments.

The spheroids formed by the healthy lung fibroblasts, NHLF, and the small-lung cancer cells, A549, were stained with Hoechst 33342 and Alexa Fluor 488 to observe, respectively, the cell nucleus and the actin filaments. The spheroids formed by A549 cells are characterized by a poorly differentiated actin cytoskeleton, where the actin filaments are mainly distributed around the cells. Compared to A549 cells, healthy lung fibroblasts present a well-differentiated actin cytoskeleton with thick actin bundles distributed around and over the cells. Furthermore, from the confocal images the dissimilarities in the shapes of the two cell lines present in the multicellular spheroids are clearly visible: more rounded A549 cells and more elongated NHLF cells.

5.3 Mechanics of lung spheroids measured with pyramidal probes

The mechanical properties of lung spheroids were using silicon nitride cantilevers (MLCT, 0.5 N/m), with the probing tip being a four-sided pyramid with a half-open angle of 20°. The tip length varied between 3 μm and 8 μm with a mean of 5.5 μm (according to manufacturer data). Young's modulus was calculated at two different indentation depths (low indentation = 1 μm; high indentation: 2-3 μm), which were obtained by adjusting the load force to 5 nN and 15 nN, respectively. The results are presented in figure 5.2.

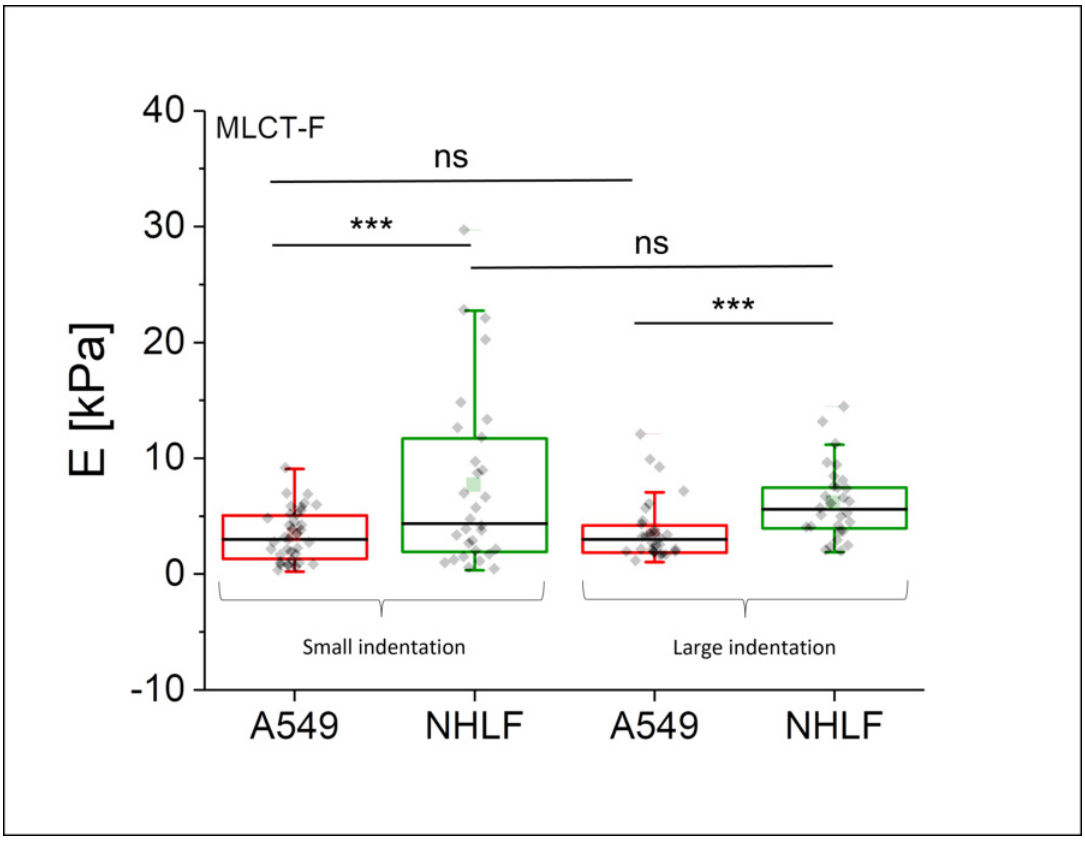

Figure 5.2: **Young's modulus obtained for spheroids formed from lung cells (lung cancer: A549 cells, lung fibroblasts: NHLF cells), measured with MLCT cantilevers.** For each cell line, 10 spheroids were measured (3 force maps per spheroid, each point denotes an individual elasticity map). The squares and black lines are the mean and median, respectively; the box denotes the standard deviation. Low (below 1 μm) and high (above 2-3 μm) indentions were considered (*** $p < 0.001$, ns - not statistically significant).

The main results show that for each cell line, Young's modulus remained the same, regardless of the indentation depths considered. It suggests that the probed

spheroid layer remained mechanically homogenous. No influence of the presence of ECM or cell nucleus inside the specific cell type was detected in the mechanical properties of spheroids. However, the spheroids formed from healthy fibroblasts (NHLF cells) were significantly stiffer than those made from lung cancer (A549 cells). The corresponding Young's modulus was 7.6 ± 7.4 kPa (n = 30 maps) versus 3.3 ± 2.2 kPa (n = 36 maps) and 6.9 ± 3.2 kPa (n = 30 maps) versus 3.7 ± 2.7 kPa (n = 29 maps) for low and high indentations.

5.4 Mechanics of lung spheroids measured with spherical probes

The elastic properties of two types of lung spheroids were measured using spherical cantilevers with spherical probes mounted at the free end. The spheres were characterized by a radius of 5 μm and 10 μm. In this case, low and high indentations were considered; however, their values were larger than pyramidal probes. The indentation depth for smaller probes was between 2-3 μm, while for larger probes was 4-6 μm. These indentation depths were obtained by applying a load force of 15 nN. The comparison between Young's moduli is shown in figure 5.3.

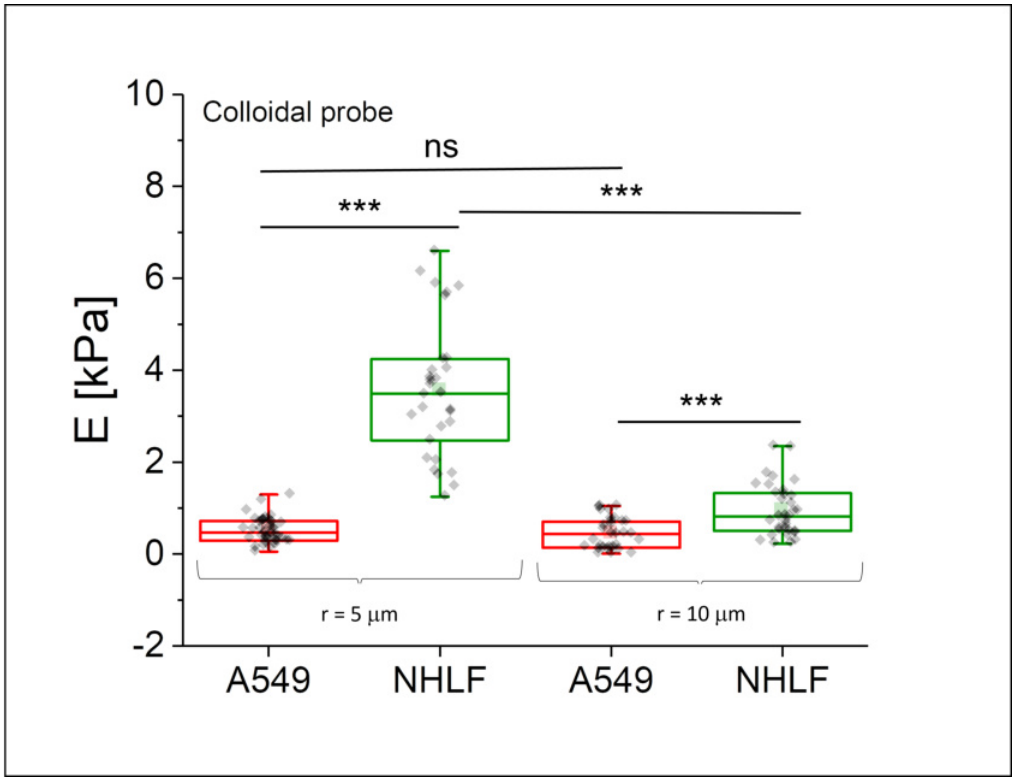

Figure 5.3: **Young's modulus obtained for spheroids formed from lung cells (lung cancer: A549 cells, lung fibroblasts: NHLF cells), measured with cantilevers with spherical probes of 5 μm and 10 μm radius.** For each cell line, 10 spheroids were measured (3 force maps/spheroid, each point denotes an individual elasticity map). The squares and black lines are the mean and median, respectively; the box denotes the standard deviation (*** $p < 0.001$, ns - not statistically significant).

As expected from the literature data [125] [140], Young's modulus is smaller than that obtained from the spheroids' measurements with the pyramidal tip. Young's modulus, obtained for spheroids formed from lung cancer cells (A459 cells), was independent of the spherical probes used in the measurements. Its value remained similar, i.e., 0.5 ± 0.2 kPa ($n = 39$ maps) versus 0.45 ± 0.34 kPa ($n = 31$ maps), for spherical probes of 5 μm and 10 μm radius, respectively. Analogously as for pyramidal probes, these results indicated mechanical homogeneity of the lung cancer spheroids. A different situation is observed for spheroids formed from lung fibroblasts. Here, Young's modulus was, i.e., 3.6 ± 1.5 kPa ($n = 30$ maps) versus 0.95 ± 0.57 kPa ($n = 33$ maps), for spherical probes of 5 μm and 10 μm radius, respectively.

5.5 Mechanics of lung spheroids measured with tipless cantilevers

Finally, the elastic modulus of the lung cell spheroids was calculated by using a tipless cantilever. In this case, the indentation reached was between 4 and 6 μm. To determine the value of Young's modulus, the Hertz model was applied, in which a cantilever denotes the flat rigid surface indented by a soft sphere (here, spheroid). Thus, the indenting spherical probe's radius equaled the particular sphere's radius, which was within 300 μm. The results from these experiments are shown in figure 5.4.

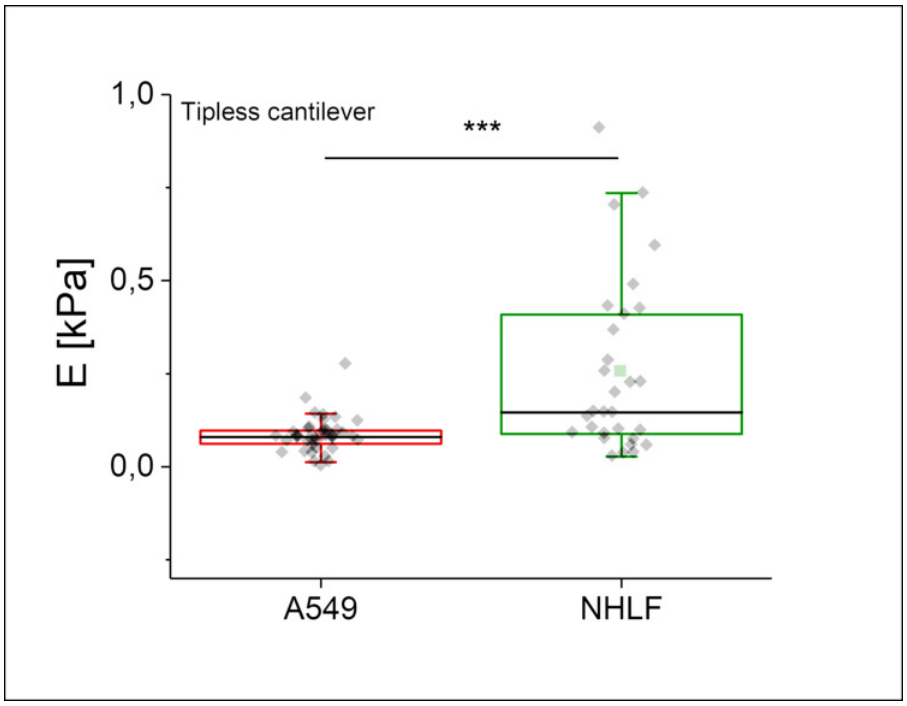

Figure 5.4: **Elastic modulus obtained for spheroids formed from lung cancer cells and fibroblasts determined from the experiments in which tipless cantilevers were used.** For each cell line, 10 spheroids were measured (3 force maps/spheroid, each point denotes an individual elasticity map). The squares and black lines are the mean and median, respectively; the box denotes the standard deviation (*** $p < 0.001$).

The most important observation is that the values of Young's modulus are much smaller as compared to modulus values when pyramidal and spherical probes were considered. The moduli range was 0.08 $\pm$ 0.04 kPa (n = 40 maps) and 0.25 $\pm$ 0.23 kPa (n = 30 maps) for spheroids formed respectively by A549 cells and NHLF cells.

5.6 Mechanics of the lung spheroids - summary

At the single-cell level, the mechanical properties of individual cells are related to the organization and/or density of actin filaments. The results presented in this section can relate the mechanical properties of lung spheroids to a different organization of the actin cytoskeleton, which is characteristic for each studied cell line, i.e., NHLF fibroblasts and A459 lung cancer cells 5.1. Spheroids formed by lung cancer cells are densely packed with cells, in which the actin cytoskeleton forms a ring around the cells. In the case of spheroids formed from NHLF fibroblasts, the number of cells was smaller. Cells preserved spindle-like morphology, which was accompanied by a larger area occupied by actin filaments. Apart from entirely distinct actin filament organization, lung fibroblasts could also secrete some ECM proteins that make the matrix surrounding the cell stiffer [143].

The results obtained for lung cells show that spheroids formed by lung fibroblasts are stiffer than spheroids formed by cancer cells (they are also consistent with already published data showing that individual cancer cells are softer than normal cells [112]. The obtained results were consistent for all measurements recorded with various cantilevers. However, the apparent Young's modulus strongly depended on the probe type. Its highest value was obtained for pyramidal probes, then spherical ones, and the smallest for tipless cantilevers. A summary of all the results obtained for spheroids formed from lung cells (NHLF – healthy lung fibroblasts, A459 – lung cancer cells) measured with various cantilever types is presented in table 5.1.

Table 5.1: *Young's modulus determined for spheroids formed from lung cells measured with the different cantilever types. The values are expressed as mean ± standard deviation of the mean (n – the number of the force maps taken for the analysis).*

	E [kPa] for spheroids from A549 cells	E [kPa] for spheroids from NHLF cells	Number of force maps	Indentation range
MLCT- F (small indentation)	3.3 ± 2.2	7.6 ± 7.4	36-30	<1 µm
MLCT –F (large indentation)	3.7 ± 2.7	6.9 ± 3.2	29-30	2-3 µm
Sphere with r = 5 µm	0.5 ± 0.2	3.6 ± 1.5	39-30	2-3 µm
Sphere with r = 10 µm	0.4 ± 0.3	0.9 ± 0.5	31-33	4-6 µm
Tipless	0.08 ± 0.05	0.25 ± 0.23	40-30	2-4 µm

Notably, regardless of the probing tip, the distribution of the apparent Young's modulus was largest for lung fibroblasts than for cancer cells which indicates (and can be related to) heterogeneity in the structure of spheroids (distinct actin

filaments organization and the presence of ECM proteins secreted by fibroblasts). More uniform distribution of the apparent Young's modulus in lung cancer cells indicates a poorly differentiated cytoskeleton.

Having in mind the relativeness of the apparent Young's modulus, the rigidity index was calculated (section 4.3.4). Its value allows objectively evaluating the difference between the elastic modulus of spheroids, independent of the cantilever type used in the measurements. Its value is defined as a logarithmic ratio of the elastic modulus of the lung cancer cells to healthy lung fibroblasts (figure 5.5).

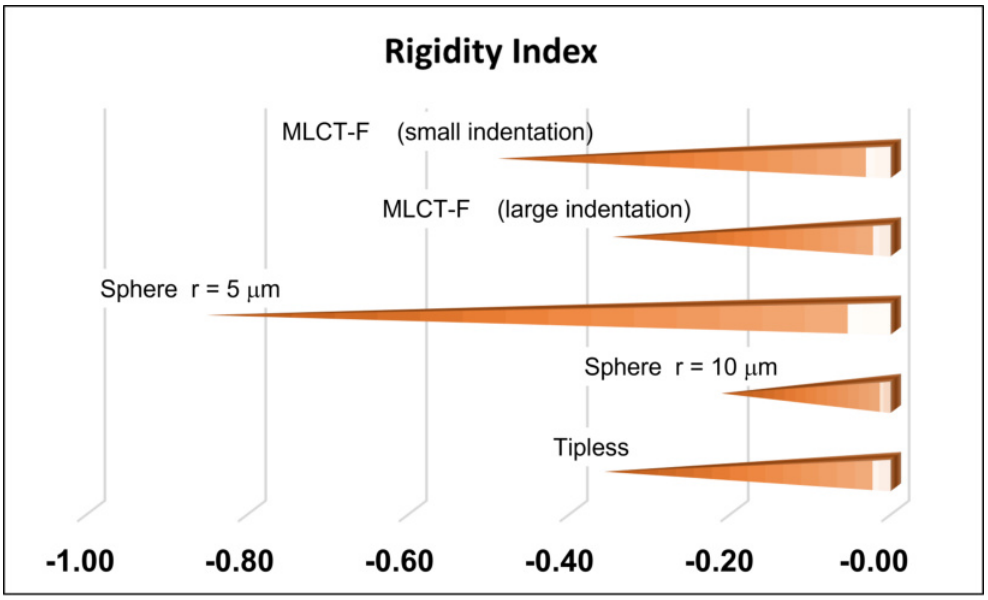

Figure 5.5: **Rigidity index showing softening of lung cancerous cell lines.** Regardless of the cantilever type used during the AFM indentation, spheroids formed from cancer cells are softer (spheroids formed by A549 lung cells in relation to the ones from NHLF fibroblasts).

The rigidity index for all cases is negative (from -0.22 to -0.86), which indicates that spheroids formed from cancer lung cells are more deformable than those composed of healthy lung fibroblasts. One can recall here that the difference in mechanical properties between the studied spheroids is the same (spheroids are of the same type and treatment in all experiments). The use of cantilevers with distinct tips, size and geometry, allows for enhancing the detection sensitivity of the mechanical properties. The most significant difference was observed during the indentation with spherical probes with a diameter of 5 μm, while the lowest is seen for the indentation using a spherical probe with a radius of 10 μm. MLCT and tipless cantilevers are placed in between. To understand why the values of Young's modulus depend on the cantilever type, one can consider from which part of the investigated sample mechanical response origins.

Indeed, one of the parameters that Young's modulus value is dependent on is the indentation depth. It is known that at smaller indentation depths, the tension generated by the cell membrane and the superficial layer of the actin cortex is responsible for most of the mechanical response, whereas, at higher indentations, this role is taken by the other cellular organelles. Therefore, the indentation depth obtained with them matters in the measurements with the different shapes of the probes. As previously mentioned, healthy fibroblasts (NHLF cells) are characterized by the presence of thick actin bundles that span all over the spheroids. The spheroids formed by the NHLF cells show a higher value of Young's modulus than those formed by the cancerous A549 cells, especially when probed with the small spherical probe and pyramidal probe. In these two conditions, the rigidity score shows the largest value, indicating a significant difference between the spheroids formed by the two cell lines, suggesting that they are suitable for detecting the difference between both spheroid types.

In conclusion, the results obtained for lung cells, i.e., fibroblasts and cancer cells, show the relation of Young's modulus on the organization of actin filaments and/or the presence of ECM. The softening of cancer spheroids was independent of the cantilever type (more specifically, a tip applied to probe the spheroid surface) used for the experiments. However, the magnitude of changes was strongly related to the cantilever type, suggesting that using the cantilever with a specific probing tip can be essential for increasing/decreasing the sensitivity of the AFM-based elasticity measurements.

Chapter 6

Mechanical and microrheological properties of bladder cancer cells at 2D and 3D levels.

6.1 Objectives

Oncogenic transformation is associated with rearrangements in the cell cytoskeleton, particularly in actin filaments and microtubular networks [66]. Any alterations in the structure and organization of cytoskeletal elements can be detected with such methods as atomic force microscopy because of their capability to probe mechanical properties at the single-cell level [110] [113]. This chapter presents the results of AFM-based indentation measurements of various bladder cancer cells cultured as single, individual cells, cell monolayers, and spheroids. The goal was to evaluate in a quantitative way how the cytoskeleton (in particular, actin filaments) is organized inside the cells depending on the type of cultures, i.e., 2D or 3D, and how this correlates with elastic and/or rheological properties of these cells. The studied bladder cancer cell lines originated from various stages of bladder cancer progression. They were HCV29 (non-malignant cell cancer of the ureter), HT1376 (bladder carcinoma, grade 3), and T24 (transitional cell carcinoma, grade 4). A detailed description of the studied cell lines is included in chapter 3. The results presented within this chapter were published in *Gnanachandran et al. J. Biomechanics 144 (2022) 111346* (All rights were obtained to reprint the images, where necessary).

6.2 Mechanical properties of bladder cancer cells

6.2.1 Actin cytoskeleton organization in bladder cancer cells

Most of AFM cell mechanics studies relate the mechanical properties to the actin cytoskeleton [66] [67] [112]. Thus, in the first step, the organization of actin filaments inside the studied bladder cancer cells and spheroids was visualized using fluorescence and confocal microscopes (details of the sample preparation and image recording are in sections 3.9 and 3.10). Exemplary fluorescent images are shown in figures 6.1 and 6.2.

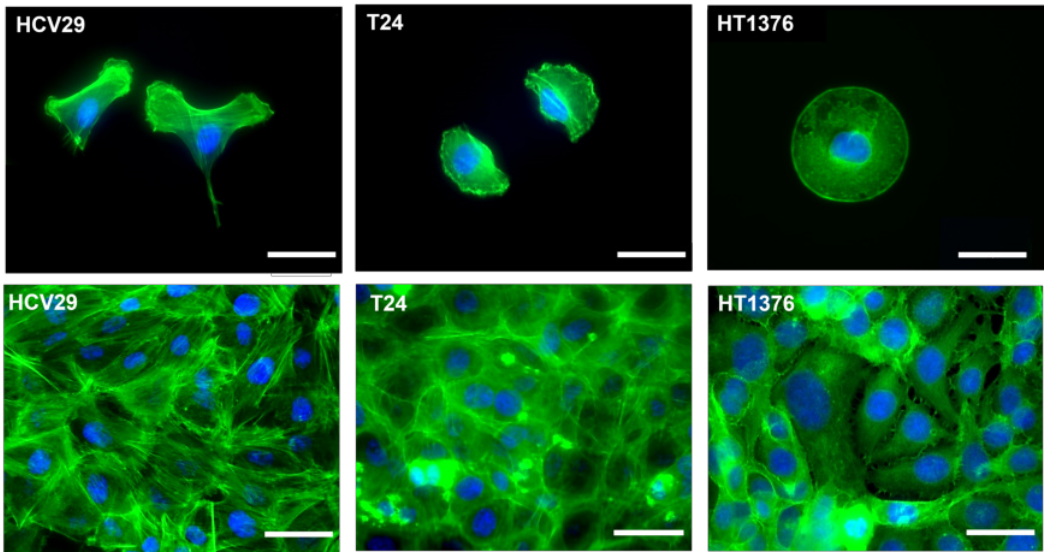

Figure 6.1: **Fluorescent images of the actin cytoskeleton in non-malignant HCV29, transitional cell carcinoma T24, and carcinoma HT1376 cells cultured as single cells and monolayers (2D cultures).** Staining: cell nucleus (blue) – Hoechst 33342 and F-actin (green) – phalloidin conjugated with Alexa Fluor 488. The scale bar is 10 μm. (figure reprinted from Gnanachandran et al. [144]).

Non-malignant HCV29 and transitional cell carcinoma T24 cells reveal well-differentiated actin filament organization showing stress fibers (thick actin bundles that span the cell body). Their presence was detectable inside the individual cells cultured as single cells and monolayers. In the latter, the number of actin bundles was much more evident, particularly in HCV29 cells. Carcinoma HT1376 cells display different F-actin organization with no stress fibers. The distribution of actin filaments changes when cells are cultured as spheroids (figure 6.2).

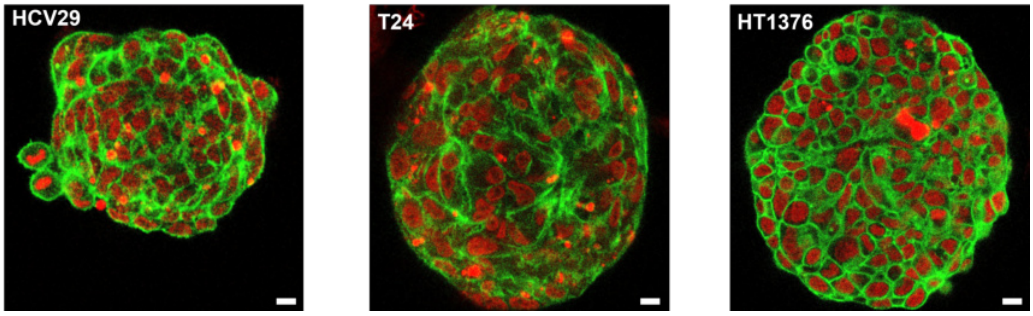

Figure 6.2: **Confocal images of the actin cytoskeleton in spheroids formed from HCV29, T24, and HT1376 cells.** Staining: cell nucleus (red) – SiR-DNA and F-actin (green) – phalloidin conjugated with Alexa Fluor 488. One slice from the Z-stack of each cell line is presented. The scale bar is 10 μm. (figure reprinted from Gnanachandran et al. [144]).

F-actin is mainly grouped around the cells. Comparing the recorded images of bladder spheroids, one can notice that HT1376 spheroids have cells that are organized in a shell-like manner, while it is still possible to see some stress fibers in HCV29 and T24 cells.

6.2.2 F/G- actin expression in bladder cancer cells

Inside the cells, actin can be present in two forms: monomeric G-actin and polymerized F-actin. The latter form actin filaments visualized typically in fluorescent microscopes. We postulate here that actin filaments are responsible for the elastic properties of cells, while monomeric G-actin is responsible for the viscous part of their cell mechanics. Therefore, before any AFM measurements, the expression (amount) of G-actin and F-actin was verified in the studied bladder cancer cell lines by using the Western blot (section 3.6). In both HCV29 and T24 cells, a dark band corresponding to both G- and F- actin was observed, which, in turn, was less intense in HT1376 cells (figure 6.3 A).

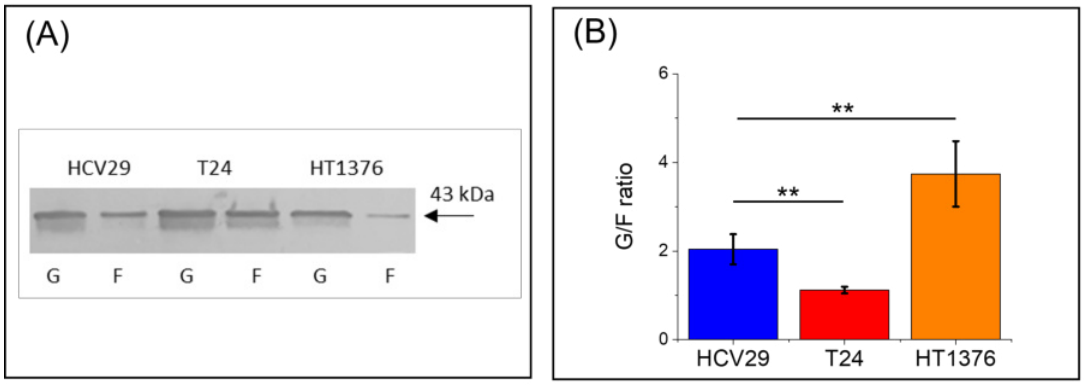

Figure 6.3: **F/G-actin expression in BC cells.** A) An exemplary Western blot image showing G- and F-actin expression in human bladder cancer cells. Both bands correspond to 43 kDa. B) Determined G/F-actin ratio, shown as mean ± SEM, from 3 to 4 independent repetitions, **p $<$ 0.001 (figure reprinted from Gnanachandran et al.)

By applying the densitometry approach, the G- and F- actin ratio was estimated (figure 6.3 B). The highest G/F actin ratio was obtained for HT1376 cells, 3.74 ± 0.74 (n = 3 repetitions), while the lowest ratio was seen for T24 cells (1,12 ± 0.15). The G/F actin ratio for HCV29 cells was placed between these two cell lines (2.04 ± 0.68).). In summary, among the studied bladder cancer cell lines, HT1376 cells were characterized by a high level of monomeric G-actin, while its lowest amount was observed for T24 cells. One can notice that lower G-actin was observed for cells in which thick actin bundles are formed (figure 6.1). There is no correlation between the amount of G-actin and the stage of bladder cancer progression.

6.2.3 Nanomechanical properties of bladder cancer cells

The elastic properties of the bladder cancer cells were measured using AFM-based nanoindentation experiments and quantified with Young's modulus, which reflects the ability of cells to withstand compressive forces (details of the data analysis are described in section 4.3). Young's modulus obtained from the AFM measurements is a relative value that is dependent on various parameters, including the choice and calibration of the cantilever, the AFM experimental conditions such as the load speed, the poking location of the cell surface, the cell culture conditions, the cell confluency, the number of passages and the way of data analysis [145]. Therefore, the experimental conditions and data analysis must be adjusted to compare the mechanical properties among various cell lines. One such parameter is the indentation depth [88]. When the AFM tip starts indenting into the

cell, the first structure it meets is the glycocalyx attached to the cell membrane, followed by the actin cortex. When moving deeper into the cell, the tip is in contact with the several organelles present inside the cell and the cytosol. Therefore, at smaller indentation depths, the cell membrane tension and superficial layers of actin filaments contribute to the mechanical response of cells, while at deeper indentations, the main contribution comes from the cellular organelles, like the cell nucleus or microtubular network [126] [146].

In this study, an analysis of data recorded during the indentation of single cells was conducted at different indentation depths (figure 6.4).

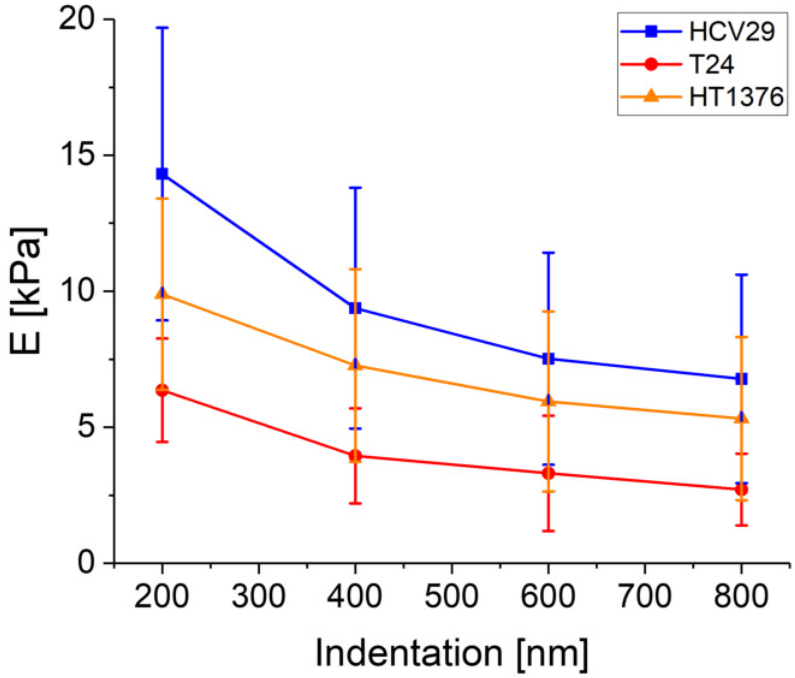

Figure 6.4: **Young's modulus of HCV29, T24 and HT1376 at single cell level at different indentation depth.** Results are presented as mean ± standard deviation.

Young's modulus plotted as a function of indentation depth decreases, as previously confirmed by Lekka et al. [126]. However, despite this relationship, cancerous T24 and HT1376 cells were softer than the non-malignant HCV29 cells, which agrees with already published results showing that cancer cells are softer [112]. The results presented in figure 6.4 highlight that mechanical properties among various cell types should be compared for a given indentation depth. In this study, the indentation of 800 nm was chosen to investigate the overall elasticity of the cell (figure 6.5).

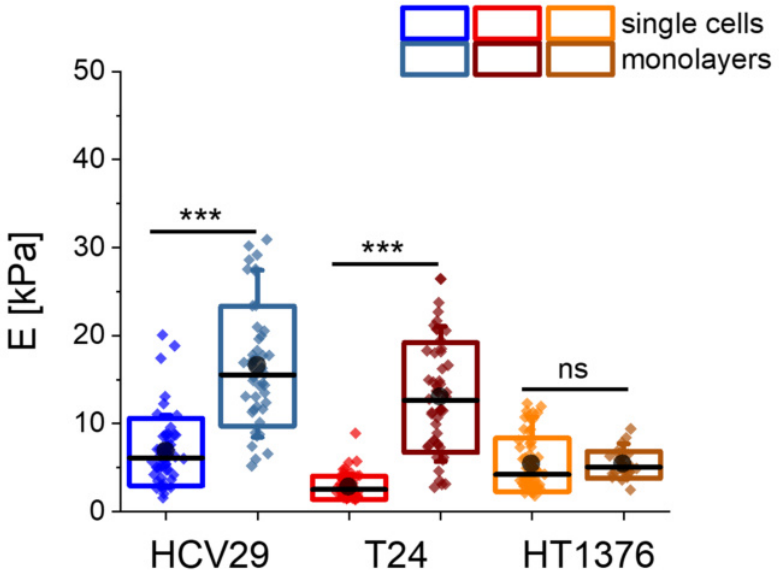

Figure 6.5: **Young's modulus determined for HCV29, T24, and HT1376 cells at single-cell and monolayer levels.** Box plots showing Young's modulus variability for 2D cultured conditions with MLCT cantilevers. Each point denotes the mean value calculated for single cells. The total number of cells measured was between 27 to 50 cells, depending on the cell type and culture conditions. The black dots and lines are mean and median; the box denotes standard deviation; error bars represent 10 % and 90 % percentile (*** $p < 0.001$, ns – not statistically significant)(figure reprinted from Gnanachandran et al. [144]).

The apparent Young's modulus values obtained for the three bladder cell lines are shown in table 6.1.

Table 6.1: *Young's modulus determined for HCV29, T24, and HT1376 cells at single-cell and monolayer levels for the indentation depth of 800 nm. Data are presented as a mean ± standard deviation from N cells*

Cell type	**Single cells**		**Cell monolayer**	
-	**N° cells**	**E [kPa]**	**N° cells**	**E [kPa]**
HCV29	55	6.8 ± 0.5	45	16.5 ± 1.0
T24	64	2.7 ± 0.2	52	13.0 ± 0.9
HT1376	58	5.3 ± 0.4	27	5.3 ± 0.3

First, the non-malignant HCV29 cells were rigid compared to cancer cells; thus, the highest Young's modulus was obtained at the single-cell and monolayer levels. The moduli changes depending on the culture conditions and cell types. HCV29 and T24 cells display a significant increment in Young's modulus, while the mechanical properties of HT1376 cells remain unaltered. These results indicate that

the mechanical properties of these cells are strictly related to the organization of the actin filaments. Young's modulus increased for cells cultured as monolayers only in HCV29 and T24 cells containing actin stress fibers. On the contrary, the absence of stress fibers in HT1376 cells is reflected in the unaltered mechanical properties of this cell line.

Next, the mechanical properties of multicellular spheroids formed by the same bladder cell lines were measured [*more details on spheroid preparation are in section 4.3*]. In the case of spheroids, longer NSC36 cantilevers were used during AFM measurements (tip height was 13 μm, according to manufacturer data). The indentation depth obtained was 2-3 μm. The choice was dictated by the fact that in spheroids, cells are embedded within the microenvironment. Thus, the determined Young's modulus reflects the contribution of cells forming the spheroids and the surrounding microenvironment. Knowing that spheroid growth depends on the initial number of cells and time ([46]), the spheroids with a diameter of 400 μm, cultured for 3 days were compared. This way, all spheroids from HCV29, T24, and HT1376 cells could be measured with equivalent dimensions and similar culture conditions. Young's modulus for spheroids is presented in figure 6.6.

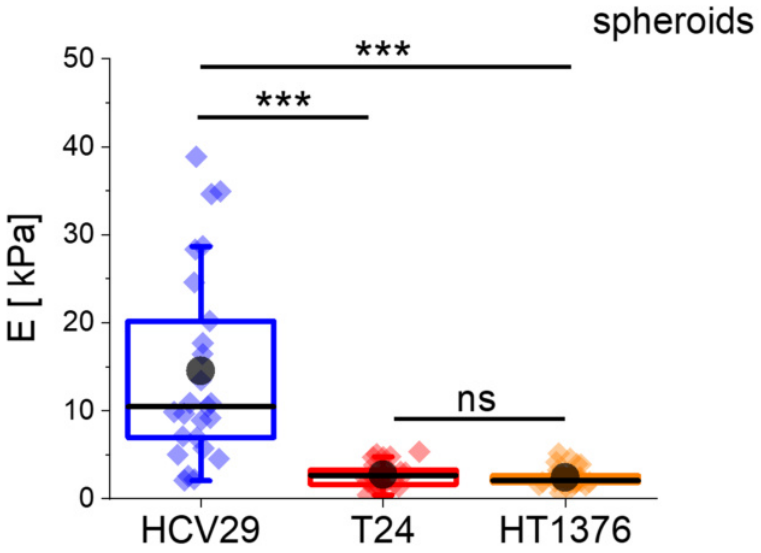

Figure 6.6: **Young's modulus determined for HCV29, T24, and HT1376 spheroids, measured with NSC36 cantilevers.** For each cell line, 15 spheroids were measured (2 force maps/spheroid, each point denotes an individual elasticity map). The black dots and lines are mean and median; the box denotes standard deviation; error bars represent 10 % and 90 % percentile. (*** $p < 0.001$, ns – not statistically significant)(figure reprinted from Gnanachandran et al. [144]).

The highest elastic modulus value characterized the spheroids formed from HCV29

cells, 14.5 ± 2.2 kPa, indicating that they are rigid structures. The spheroids formed from the cancer cell lines displayed a similar value of 2.7 ± 0.3 kPa and 2.4 ± 0.2 kPa, respectively, for T24 and HT1376 cells. These results show that, in the 3D culture, the non-malignant HCV29 cells form stiffer spheroids than the cancer cell lines.

The direct comparison of mechanical properties of cells, monolayers, and spheroids is difficult because of two different cantilevers used during the indentation and two different indentation depths. Thus, the rigidity index was calculated to assess the magnitude of the difference in the mechanical properties of bladder cancer cells, monolayers, and spheroids (figure 6.7). Analogously as for lung spheroids, the rigidity index is defined as a logarithmic ratio of the Young's moduli obtained for cancer cells/monolayers/spheroids to values of the reference sample, which in our case, are the results obtained for non-malignant HCV29 cells/monolayers/spheroids [*Details are in section 4.3.4*].

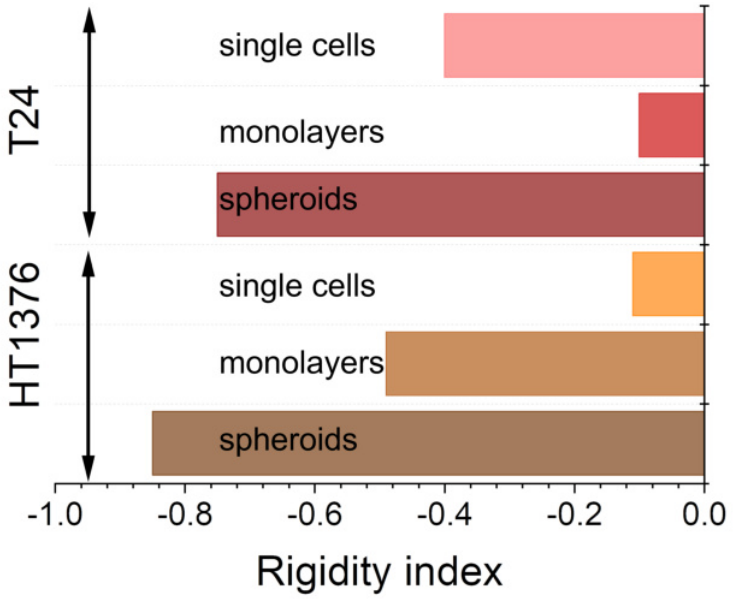

Figure 6.7: **Rigidity index determined for single cells, monolayers, and spheroids formed from HCV29, T24, and HT1376 cells.** Its negative value indicates softening of cancer samples - the largest softening was observed for the spheroids. (figure reprinted from Gnanachandran et al. [144]).

The rigidity index shows the largest softening of cancer spheroids (R = -0.75 and R = -0.85, formed from T24 and HT1376 cells, respectively), indicating that cancer spheroids are more deformable than spheroids made of non-malignant HCV29 cells. The rigidity index values depend on the cell type and culture conditions for

cells grown as 2D cultures (either single cells or cell monolayers). For T24 cells, the rigidity index is the lowest for cells cultured as monolayers, while in HT1376 cells, the opposite relation is observed. The rigidity index is the lowest for cells cultured as single cells. This is in good relation to the fact that T24 cells express more stress fibers when cultured as a monolayer than single cells.

6.3 Microrheological properties of bladder cancer cells

Young's modulus determination from contact mechanics assumes that the living cell is a purely elastic material with a homogeneous structure. However, cells are known to exhibit viscoelastic nature [147]. The viscoelasticity of cancer cells has been demonstrated to be a useful marker of their metastatic potential in different types of cancers, including bladder cancer [148] [149] [128]. There are various ways to measure the viscoelastic properties of biological samples using the AFM [127]. Two approaches were considered to explore the viscoelasticity of the three bladder cancer cell lines studied here. First, the mechanical properties of cells were recorded for single cells indented with various speeds, from 0.5 μm/s to 10 μm/s. In the other, sinusoidal oscillations at the specific depth were applied within the range of 0.5 Hz to 150 Hz (250 Hz) to single cells, cell monolayers, and spheroids.

6.3.1 Load speed effect on mechanical properties of single cells

Part of the AFM-related studies evaluates the viscoelastic properties of living cells from the indentation measurements recorded at different load speeds [150]. The load speed is related to the loading rate, which describes time-related changes in the load force. Few studies have already been carried out by considering the effects of different loading rates showing a direct relationship between the mechanical properties of cells and the loading rate [150] [151] [152].

Based on those previous works, indentation measurements were performed in the three bladder cell lines (HCV29, T24 and HT1376) at load speeds ranging from 0.5 μm/s to 10 μm/s (figure 6.8).

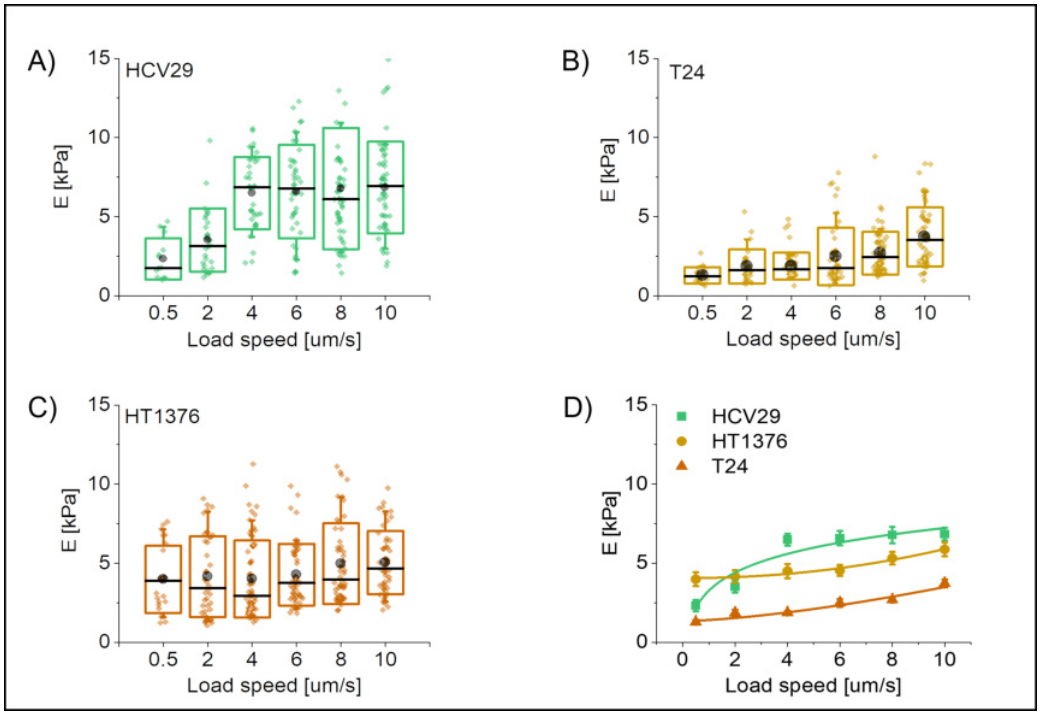

Figure 6.8: **Young's modulus of HCV29, T24, and HT1376 cells plotted as a function of the load speeds.** (A-C) In the box plot, the line and the circle represent the median and the mean values, respectively. The symbols are Young's modulus calculated as a mean from each recorded map. The boxes indicate the quantiles (25 % and 75 %), while the error bars represent the standard deviation. D) Comparison of relationships between Young's modulus and load speed for all studied cell lines. A single point denotes a mean ± standard deviation calculated from n (30-60) elasticity maps.

Young's modulus was calculated using Hertz contact mechanics with cone approximation of the probing tip. Moduli values were calculated for the indentation depth of 800 nm. For HCV29 cells, Young's modulus increases with the load speed up to 4 μm/s (from 2.33 ± 0.36 kPa at 0.5 μm/s to 6.49 ± 0.38 kPa at 4 μm/s). Above this speed, it remains constant at the 6 -7 kPa. Young's modulus for cancer cells increases monotonically from 1.29 ± 0.13 kPa (0.5 μm/s) to 3.73 ± 0.25 kPa (10 μm/s) and from 3.99 ± 0.44 kPa (0.5 μm/s) to 5.88 ± 0.31 kPa (10 μm/s), for T24 and HT1376 cells, respectively. Notwithstanding, the increase is more pronounced for T24 cells, not HT1376 cells.

Following the theory described by Nawaz et al. [152], to determine the viscoelastic property of cells at different load rates, the relations between Young's modulus and load speed were fitted with the function $E(v) = k \cdot v^{\alpha}$, where v is the load speed, and α is the power law exponent (figure 6.9).

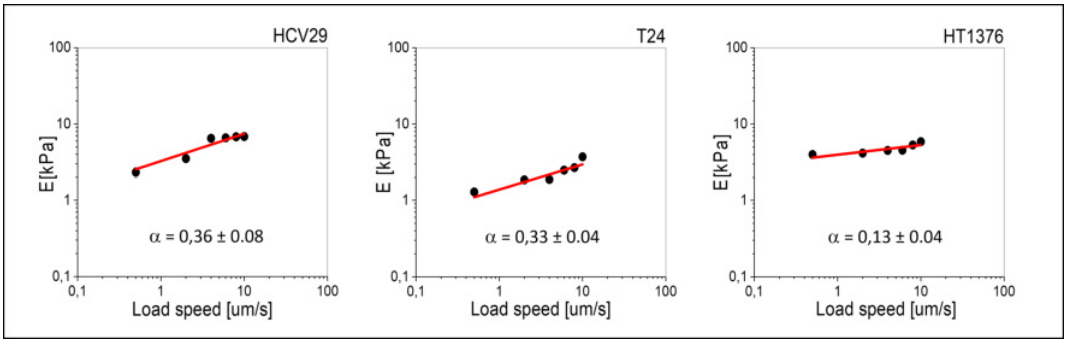

Figure 6.9: **Power-law function fitted to the data showing the relation between Young's modulus and load speed.** Young's modulus is expressed as a mean ± standard deviation calculated from 30-60 elasticity maps.

The power law exponent obtained for non-malignant HCV29 and transitional cell carcinoma T24 cells has similar values, i.e., 0.36 ± 0.08 and 0.33 ± 0.04, respectively. HT1376 cells were characterized by a much lower α, i.e., 0.13 ± 0.04. The observed difference seems to agree with the cytoskeletal organization of the cells. The presence of actin stress fibers observed for HCV29 and T24 cells could be responsible for similar power law exponent values, while the lack of them increases the viscoelastic component in the mechanics of HT1376 cells. Additionally, lower α correlates with the highest G/F-actin ratio.

6.3.2 Sinusoidal oscillatory measurements

The AFM-based microrheological measurements have become more common compared to load speed measurements described above. In these measurements, the cell is indented, and sinusoidal oscillations are applied in the direction perpendicular to the cell surface [technical details may be found in section 2.1.5]. The human bladder cancer cells studied here were measured within the frequency domain between 0.5 Hz to 150 Hz (single cells and monolayers) and 250 Hz (spheroids). The oscillation amplitude was kept constant at 50 nm. As an outcome, the relationships between storage G' and loss G'' moduli and oscillation frequency were obtained (figure 6.10).

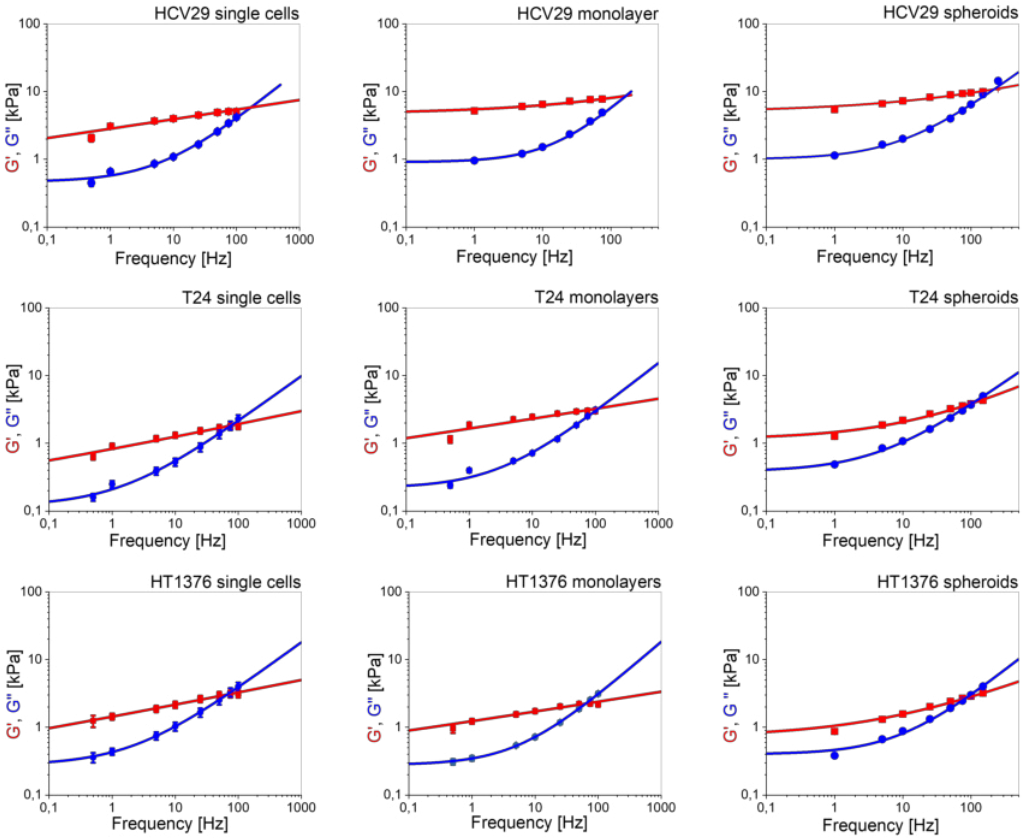

Figure 6.10: **Microrheological properties of bladder cancer cells in 2D cultures, measured with MLCT cantilevers, and spheroids, measured with NSC36 cantilevers.** Each point denotes the mean ± standard error of the mean calculated from 30 to 40 cells and 15 spheroids (2 maps/spheroids). The lines represent the fitted power-law function to the obtained data.

In the first step, the mechanical response of cells to the applied sinusoidal oscillations was studied as a function of 2D culture conditions. At first sight, the relations between Young's modulus and oscillatory frequency were characteristic for each cell type. Storage and loss moduli were the largest for HCV29 cells, while in both cancer cell lines, their values were lower, indicating that cancer cells are softer also when this type of measurement is applied. In HCV29 and T24 cells possessing stress fibers in their cytoskeletal structure, storage and loss modulus was higher for cells cultured as monolayers. The exception was HT1376 cells, for which storage and loss moduli were similar regardless of the culture conditions. For spheroids, first of all, the oscillatory measurements were possible within the larger frequency range, i.e., up to 250 Hz. Spheroids formed from rigid non-malignant cells were stiffer than spheroids composed of soft cancer cells.
The relations presented in figure 6.10 were fitted with the power law function,

resulting in a set of parameters describing the rheological properties of human bladder cancer cells (table 6.2).

Table 6.2: *Parameters describing microrheological properties of bladder cancer cells, monolayers, and spheroids, obtained from power-law function fitted to relations between storage (loss) modulus and oscillatory frequency, plotted in figure 6.10.*

Single cells	HCV29	T24	HT1376
G_N' [kPa]	2.27 ± 0.12	0.84 ± 0.06	1.14 ± 0.10
G_N'' [kPa]	0.59 ± 0.04	0.22 ± 0.01	0.26 ± 0.01
loss factor	0.26 ± 0.12	0.30 ± 0.13	0.23 ± 0.12
Cell monolayer	HCV29	T24	HT1376
G_N' [kPa]	5.03 ± 0.26	1.79 ± 0.13	1.14 ± 0.13
G_N'' [kPa]	0.88 ± 0.01	0.35 ± 0.01	0.29 ± 0.07
loss factor	0.17 ± 0.10	0.20 ± 0.02	0.54 ± 0.10
Spheroids	HCV29	T24	HT1376
G_N' [kPa]	4.99 ± 0.38	1.16 ± 0.09	0.77 ± 0.08
G_N'' [kPa]	1.01 ± 0.07	0.38 ± 0.04	0.29 ± 0.03
loss factor	0.20 ± 0.15	0.33 ± 0.07	0.38 ± 0.25

The storage G' modulus correlates well with Young's modulus obtained from the indentation experiments. Its value is the largest for non-malignant HCV29 cells and lowers for cancer cells. It indicates the larger deformability of cancer cells during the compression (Young's modulus) and when shear forces are applied. A similar tendency is observed for loss modulus G'', which describes how much energy is dissipated in the sample. These relations are independent of the culture conditions, i.e., they are preserved for single cells, monolayers, and spheroids. Based on G' and G'', the loss factor was calculated. It is the ratio between the storage and loss modulus, and it explains the solid-like and fluid-like behaviors of the studied sample. The mean value from the measurements of the single cells, monolayer, and spheroids was 0.21 ± 0.05 for HCV29 cells, 0.28 ± 0.07 for T24 cells, and 0.38 ± 0.16 for HT1376 cells. HT1376 cells were characterized by the highest loss factor, indicating that this cell line reveals the more fluid-like behavior among the three. It is again in a good relationship with the cytoskeletal organization (lack of stress fibers) and high G/F ratio (more monomeric G-actin).

6.3.3 The effect of cytochalasin D on microrheological properties of cells

The effects of cytochalasin D (cyto-D) on bladder cancer cells in 2D cultures have already been shown in previous studies [112] [154], showing that adding cyto-D changes the mechanical properties of indented cells. In microrheological measurements, the applied deformation force is a shear, not a compressive force. Therefore, to unravel the role of the actin filaments in the microrheological properties of cells, the samples were treated with 5 μM cyto-D added to 2D culture and spheroids (as described in section 3.3.1). Fluorescent images of cells and spheroids recorded before and after cytochalasin D treatment show changes in actin filaments organization (figures 6.11 and 6.12).

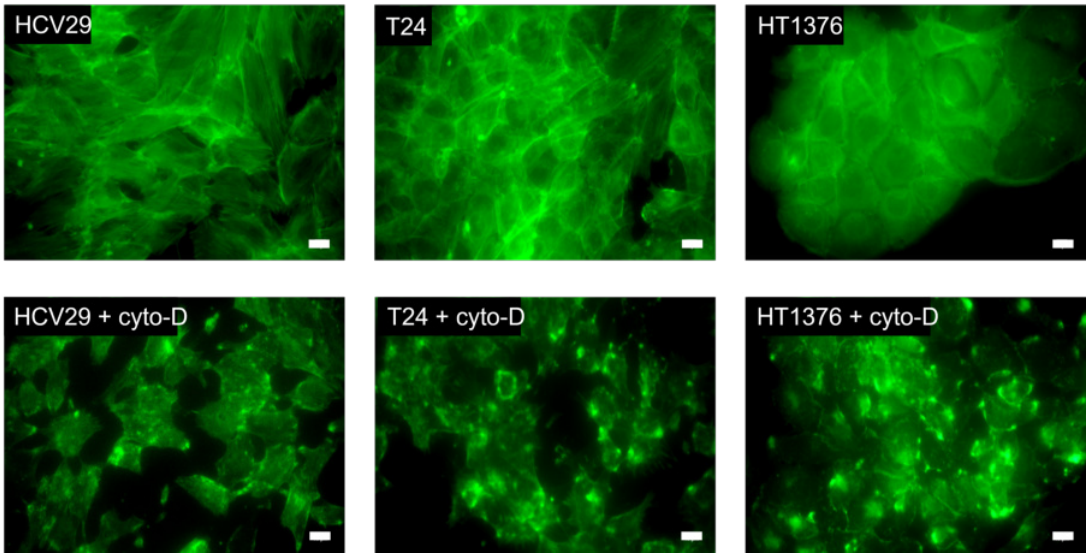

Figure 6.11: **Exemplary epi-fluorescent images of cytochalasin D treated cell monolayers of non-malignant HCV29, transitional cell carcinoma T24, and carcinoma HT1376 cells.** Staining: F-actin (green) – phalloidin conjugated with Alexa Fluor 488. The scale bar is 10 μm.

When cells are cultured as monolayers, 5 μM cyto-D treatment weakens the adhesion of cells to the underlying plastic substrate. Their surface area becomes smaller, which indicates impairments in cell adhesion. The effect of cyto-D on spheroids was visible as a disruption in the organization of the actin filaments (figure 6.12).

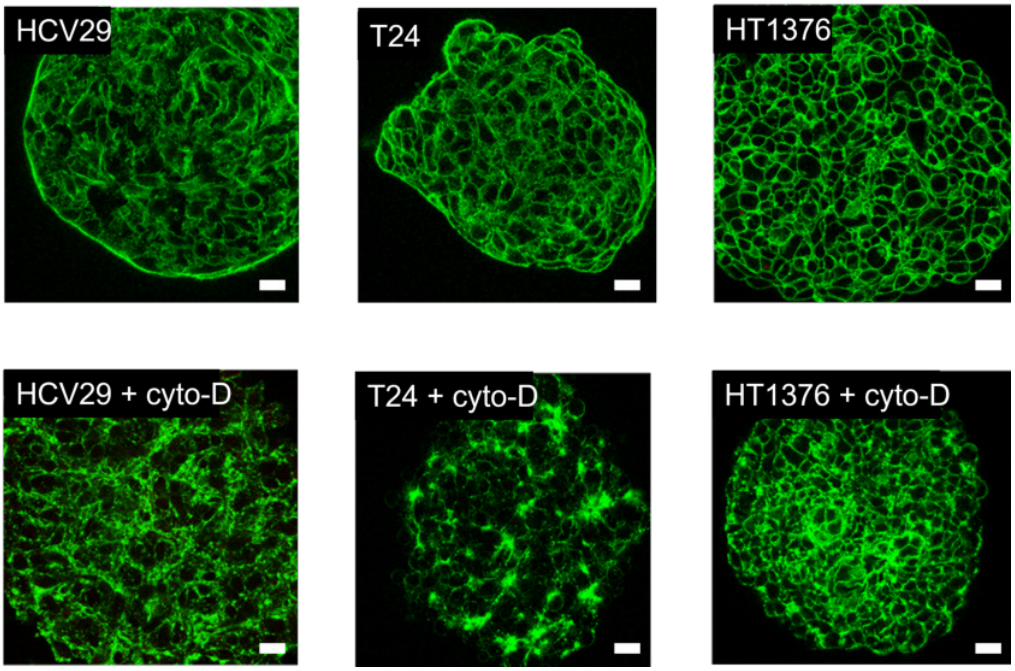

Figure 6.12: **Exemplary confocal images of cytochalasin D treated spheroids formed by non-malignant HCV29, transitional cell carcinoma T24, and carcinoma HT1376 cells.** Staining: F-actin (green) – phalloidin conjugated with Alexa Fluor 488. The scale bar is 10 μm. (Figure reprinted from Gnanachandran et al. [144]).

Having in mind cyto-D - related changes in actin filaments organization, microrheological measurements were performed. As the actin cytoskeleton is disrupted, focal adhesions do not resist the shear forces, causing the detachment of cells. Indeed, cells were easily detached during the microrheological measurements after the treatment with cyto-D. The detachment is observed as a drop of storage modulus at larger frequencies (above 20 Hz, figure 6.13).

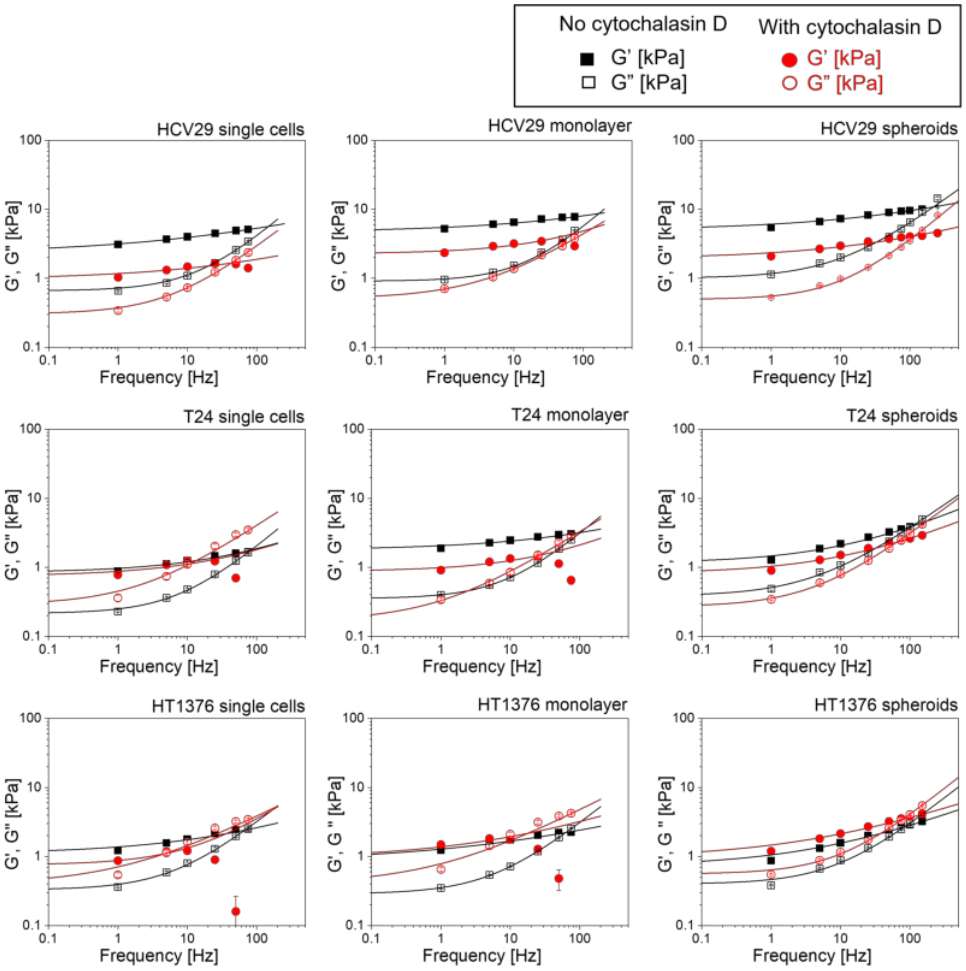

Figure 6.13: **Microrheological properties of bladder cancer cells, monolayers, and spheroids treated and not treated with 5 μM cytochalasin D.** The storage modulus *G'* and the loss modulus *G"* are plotted as a function of the frequency of oscillation. The oscillation amplitude was kept constant at 50 nm, and the frequency varied from 1 - 250 Hz for spheroids and from 1 - 100 Hz for the cells. Each point denotes the mean ± standard error of the mean calculated from n (30-40 for cells cultured in 2D, 30 for spheroids) elastic maps. The lines represent the fit of the power-law function to the obtained data. (Figure reprinted from Gnanachandran et al. [144]).

The detachment of cells is more pronounced in cancer cells than in non-malignant HCV29 cells. It can be explained by the fact that in non-malignant HCV29 cells, the amount of actin filaments is much higher than in cancer cells, which prevents the detachment of these cells. Notably, it is visible only in 2D cultures (single cells and monolayers), while it is not present in microrheological measurements of spheroids, regardless of the cell type studied.

Analogously, as for the non-treated samples, the relations presented in figure 6.13 were fitted with the power-law function, resulting in a set of parameters describing

the rheological properties of samples treated with cyto-D (table 6.3).

Table 6.3: *Parameters describing microrheological properties of bladder cancer cells, monolayers, and spheroids treated with 5 μM cytochalasin D, obtained from power-law function fitted to relations between storage (loss) modulus and oscillatory frequency, plotted in figure 6.13.*

Single cells	HCV29 Cyto-D	T24 Cyto-D	HT1376 Cyto-D
G_N' [kPa]	0.97 ± 0.15	0.75 ± 0.11	0.85 ± 0.10
G_N'' [kPa]	0.24 ± 0.01	0.29 ± 0.14	0.39 ± 0.07
loss factor	0.25 ± 0.15	0.48 ± 0.14	0.46 ± 0.40
Cell monolayer	HCV29 Cyto-D	T24 Cyto-D	HT1376 Cyto-D
G_N' [kPa]	2.30 ± 0.16	0.88 ± 0.09	1.46 ± 0.14
G_N'' [kPa]	0.51 ± 0.04	0.17 ± 0.04	0.49 ± 0.14
loss factor	0.22 ± 0.10	0.19 ± 0.21	0.34 ± 0.09
Spheroids	HCV29 Cyto-D	T24 Cyto-D	HT1376 Cyto-D
G_N' [kPa]	1.92 ± 0.16	0.81 ± 0.07	1.06 ± 0.12
G_N'' [kPa]	0.49 ± 0.04	0.27 ± 0.03	0.44 ± 0.03
loss factor	0.26 ± 0.10	0.33 ± 0.20	0.42 ± 0.06

Storage and loss modulus of non-malignant HCV29 cells, monolayers, and spheroids dropped by about 20-40 % after the cyto-D treatment. The drop was independent of the way of culture. Such a drop can be explained by the depolymerization of actin filaments induced by this compound. It is consistent with fluorescent images of HCV29 cells showing strong modifications in the actin filament organization. An almost analogous relation is observed for cancer T24 cells. A drop in storage and loss moduli was observed for all culture conditions, which can be explained by changes in actin filaments organization shown in fluorescent images. The results obtained for HT1376 cells were different. Storage modulus dropped for single cells, but simultaneously the loss modulus increased. An increase in storage and loss moduli was observed for monolayers and spheroids. These results indicate the possible higher dissipative character of these cells, which is preserved regardless of the culture conditions.

6.3.4 Describing a transition between fluid-like and solid-like cell behavior

Alongside the storage and loss modulus and loss factor, two other parameters can describe the viscoelastic nature of such samples as cells or spheroids. They are the transition frequency ω_T and the power-law exponent α obtained from the power-law fit to the obtained data [details can be found in section 2.1.5]. A graphical summary of changes in transition frequency and power-law exponent obtained for single cells, monolayers, and spheroids is presented in figure 6.14.

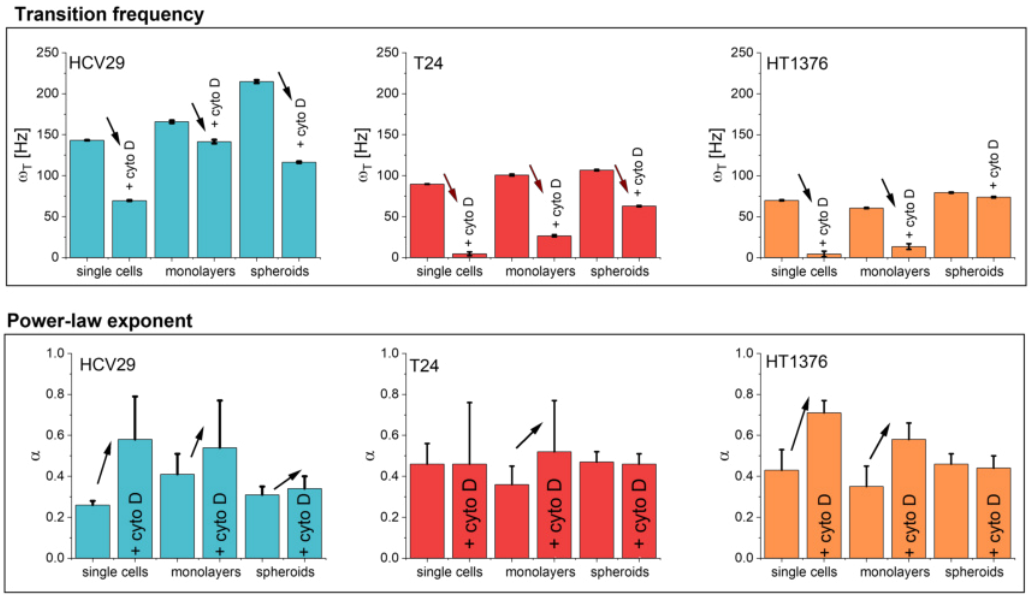

Figure 6.14: **Transition frequency and power-law exponent determined for single cells, monolayers, and spheroids formed from bladder cancer cell lines.** The values of transition frequency and the power-law exponent, obtained from the power-law fit, are shown as a function of culture conditions before and after treatment with 5 μM cyto-D.

The table below illustrates the transition frequency values and the power-law exponents obtained from the power-law fit.

Table 6.4: *Parameters describing microrheological properties of bladder cancer cells, monolayers, and spheroids untreated and treated with 5 μM cytochalasin D, obtained from power-law function fitted to relations between storage (loss) modulus and oscillatory frequency, plotted in figures 6.10 and 6.13.*

Single cells	HCV29	HCV29 Cyto-D	T24	T24 Cyto-D	HT1376	HT1376 Cyto-D
ω_T [Hz]	143.2 ± 0.3	69.6 ± 0.6	89.6 ± 0.4	7.4 ± 0.5	70.0 ± 0.7	4.5 ± 3.4
α @ G'(ω)	0.26 ± 0.02	0.58 ± 0.21	0.46 ± 0.10	0.46 ± 0.30	0.43 ± 0.10	0.71 ± 0.06
Cell monolayer	HCV29	HCV29 Cyto-D	T24	T24 Cyto-D	HT1376	HT1376 Cyto-D
ω_T [Hz]	165.8 ± 1.6	141.5 ± 2.3	100.7 ± 0.1	26.6 ± 1.3	60.6 ± 0.7	13.6 ± 3.5
α @ G'(ω)	0.41 ± 0.10	0.54 ± 0.23	0.36 ± 0.09	0.52 ± 0.25	0.35 ± 0.10	0.58 ± 0.75
Spheroids	HCV29	HCV29 Cyto-D	T24	T24 Cyto-D	HT1376	HT1376 Cyto-D
ω_T [Hz]	214.8 ± 1.9	116.4 ± 1.0	106.7 ± 0.9	62.8 ± 0.7	79.5 ± 0.7	73.9 ± 0.9
α @ G'(ω)	0.31 ± 0.04	0.34 ± 0.06	0.47 ± 0.05	0.46 ± 0.05	0.46 ± 0.05	0.44 ± 0.06

When comparing transition frequencies for non-treated single cells, monolayers, and spheroids, it is evident that its value is lower for cancer cells compared to the non-malignant HCV29 cells, regardless of the culture conditions. They are 143.2 ± 0.3, 165.8 ± 1.6, and 214.8 ± 1.9, respectively, for HCV29 cultured as single cells, monolayers, and spheroids; 89.6 ± 0.4, 100.7 ± 0.1, and 106.7 ± 0.9, respectively for T24 cultured as single cells, monolayers, and spheroids; 70.0 ± 0.7, 60.6 ± 0.7 and 73.9 ± 0.9, for HT1376 respectively cultured as single cells, monolayers, and spheroids. The lowest values of the transition frequency were observed for HT1376 cells, regardless of the culture conditions. Results obtained for T24 cells are placed in between. Such a relation, i.e., ω_T for HCV29 cells $>$ ω_T for T24 cells $>$ ω_T for HT1376 cells, directly correlated with the presence of stress fibers. Lower ω_T points that HT1376 cells become more fluid-like materials at lower frequencies than the other cells, particularly non-malignant HCV29 cells. Importantly, this relation is preserved and independent of the culture conditions. This trend is maintained when the power-law exponent α is considered as a parameter describing the viscoelastic nature of bladder cancer cells. Its larger values indicate the increasing viscous contribution with increasing frequency.

Knowing that mechanical response to shear forces involves the actin filaments, both ω_T and α were determined for single cells, monolayers, and spheroids after cytochalasin D treatment. The transition frequency decreases regardless of the culture conditions indicating that the transition between solid-like and fluid-like states proceeds at lower frequencies than for non-treated cells. It means that the fluid-like character is more pronounced after disrupting the actin filaments. Analogously, the power-law exponent was analyzed. It increases consistently in the treated non-malignant HCV29 cells; however, its changes in cancerous cells

are less conclusive (only a lack of changes is constantly observed in spheroids).

6.4 Mechanics of bladder cancer cells at 2D and 3D levels - summary

In this chapter, the mechanical and microrheological properties with atomic force microscopy were used to discriminate three different types of bladder cancer cells: non-malignant HCV29, transitional cell carcinoma T24, and carcinoma HT1376. During the study, the cell confluency (single cells, monolayer of cells, and spheroids) and the role of actin filaments in mechanical and rheological properties were evaluated.

Fluorescent staining and Western blot analysis were applied to describe the actin cytoskeleton of the three cell lines at the single cells level. The actin cytoskeleton of non-malignant HCV29 and transitional cell carcinoma T24 cells was well-organized and displayed thick actin bundles that were not present in a poorly differentiated cytoskeleton of carcinoma HT1376 cells. HT1376 cells have the highest G/F actin ratio, indicating a high level of monomeric G-actin in these cells. This agrees with the absence of thick actin bundles in their cytoskeletal organization.

The mechanical properties of bladder cancer cells cultured as single cells, monolayers, and 3D multicellular spheroids were determined based on AFM measurements during indentation. The obtained results show that cancer cells, T24 and HT1376, were more deformable than the non-malignant HCV29 cells regardless of whether they grew as single cells or monolayers. These results were preserved for the measurements conducted on spheroids. Cancer spheroids were more deformable than spheroids formed from non-malignant HCV29 cells. Stiffening of cell monolayers composed of HCV29 and T24 cells was observed, too. The larger rigidity of these monolayers was attributed to the presence of thick actin bundles in the studied cells. Simultaneously, their role was confirmed by the nanomechanical results for HT1376 cells for those the elastic properties remained at the same level, regardless of whether they grew as single cells or monolayers. HT1376 cells remain the same at both confluency ranges. Changing the conditions from 2D to 3D cultures did not affect the mechanical relation between non-malignant and cancer cells. The spheroids formed from cancerous T24 and HT1376 cells were more deformable than spheroids consisting of non-malignant HCV29 cells. Despite a large difference between non-malignant and cancerous cells, cancer cells were characterized by similar Young's modulus- indicating that the mechanical

response of these cells to compressive forces does not allow differentiation among cancer cells at various stages of cancer progression.

Cells are not a purely elastic material but viscoelastic; the microrheological properties of the studied bladder cell lines were quantified from AFM measurements, in the sinusoidal oscillations were applied to the sample. Cancerous T24 and HT1376 cells show lower storage and loss moduli values than non-malignant HCV29. It denotes the larger deformability of cancer cells under shear forces and agrees with the results obtained from indentation experiments. The storage and loss moduli display a similar trend as Young's modulus for single cells and monolayers. Non-malignant HCV29 and cancerous T24 cells stiffen when moving from single cells to monolayer cultures, while moduli values for cancerous HT1376 cells remained at the same level. In the case of 3D cultures, the spheroids formed by HCV29 cells show the highest storage and loss moduli compared to spheroids consisting of cancer cells.

The calculated loss factor, describing the relation between elastic and viscous components, reveals a considerably large value for cancer HT1376 cells, indicating that this cell line is characterized by large viscous component, which is linear with the absence of thick actin bundles and a high level of G-actin monomers. A deeper analysis of viscoelastic properties of the studied bladder cell lines shows a power law relationship between storage and loss moduli as a function of oscillation frequency. Such relations fitted with the theoretical models can derive information on the microrheological properties of cells. Two existing approaches were fitted to derive a parameter describing two regimes of cell behavior, i.e., solid-like and fluid-like. One model uses transition frequency (a frequency at which storage and loss moduli take on the same value), and the other analyses the power law exponent. The transition frequency and the power-law exponent, obtained from the same rheological measurements, confirmed the results described by the loss factor. Cancerous HT1376 cells were more viscous, characterized by the lowest transition frequency and the highest power law exponent. The non-malignant HCV29 cells exhibited more solid-like- behavior, characterized by the highest transition frequency and the lowest power law exponent. Importantly, the transition frequency seems to be a better parameter describing the microrheological properties of cancer cells. For bladder cancer cells, it allows the differentiation between carcinoma HT1376 and transitional cell carcinoma T24 cells.

The role of actin filaments in maintaining the rheological properties of bladder cancer cells was evaluated by comparing the microrheological properties of cells before and after cytochalasin D treatment. Cytochalasin D inhibits the polymer-

ization of actin filaments; thus, the increase of viscous component in cells was expected. The increase of viscous component of bladder cancer cells treated with cytochalasin D was observed for cells cultured as grew as single cells and monolayers. The transition frequency decreased for all studied bladder cancer cells. Moving from 2D to 3D cultures, the increased viscous component after cytochalasin D treatment was observed for non-lignant HCV29 and cancerous T24 cells, while no change was observed for cancerous HT1376 cells. This allows attributing changes in cell rheological properties to the presence of thick actin bundles. Moreover, their role in maintaining cell mechanics (and rheology) remained dominant also at the spheroid level.

Chapter 7

Mechanical and microrheological properties of aging spheroids

7.1 Objectives

It has already been reported that spheroids formed from cancer cells grow similarly to solid tumors, starting from logarithmic-like growth and then revealing a plateau until tumors become potentially invasive [46]. As shown in Chapter 6, the mechanical and microrheological properties of tumor spheroids formed by bladder cancer cells are different for each cell type. In this chapter, the mechanical and microrheological properties of aging spheroids taken at the early (3 days) and late (14 days) growth phases are compared. The two selected time points mimic tumor growth, i.e., the early stage of the formation of a tumor and a well-developed tumor. The main goal was to evaluate age-related changes in the biophysical properties of spheroids and how these changes relate to their internal structure. The atomic force microscope (AFM) and the hydraulic force spectroscope (HFS) were applied to determine the mechanical properties at the nanoscale (AFM) and macroscale (HFS) levels.

7.2 Growth rate of tumor spheroids

To form spheroids of similar diameter, the cell number in each well must be adjusted to the specific cell line. To obtain spheroids of a diameter of 400 $\pm$ 50 μm, the following number of cells per well were applied: 7000 cells for HCV29 cells, 1500 cells for HT1376 cells, and 10000 cells for T24 cells. Then, the growth of spheroids was traced at 3, 5, 7, 13, and 15 days. Each day the spheroid diameter

was determined using phase-contract images recorded by an optical microscope. The relations between spheroid diameter and the day of culture for each cell line studied are shown in figure 7.1. It reveals a biphasic character, i.e., starting with a fast-growing region in which cells dividing increase the spheroid diameter, followed by a plateau in which spheroid diameter remains at the same level.

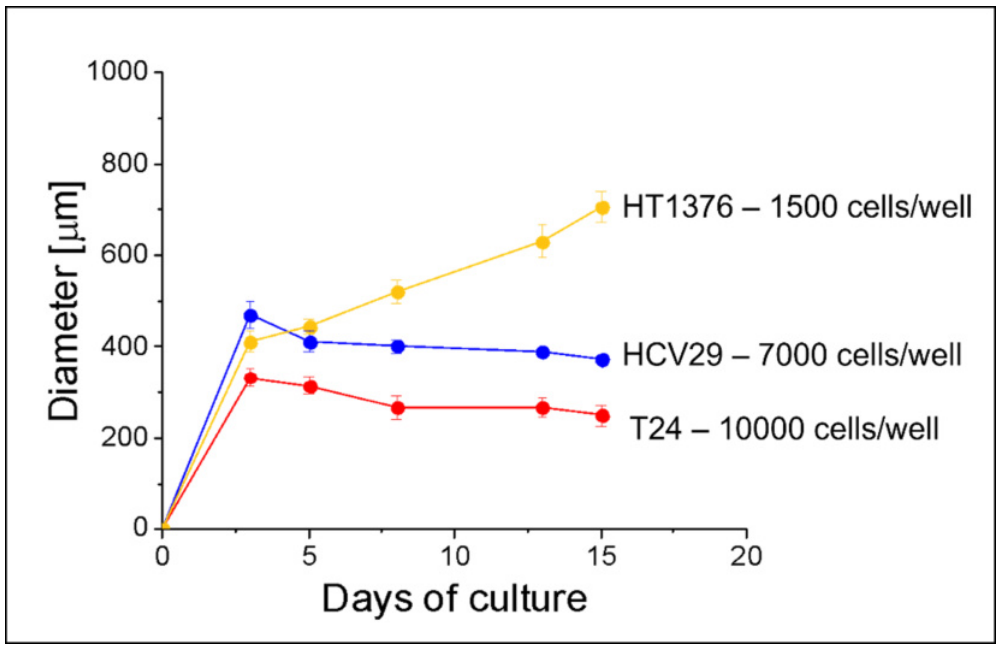

Figure 7.1: **The relation between spheroid diameter and the day of culture obtained for the bladder spheroids.** Spheroids were formed by non-malignant HCV29 cells, transitional cell carcinoma T24 cells, and carcinoma HT1376 cells. Each point denotes a mean value from 10 spheroids per cell line, and the number of cells/well required to form spheroids of 350-450 μm diameter is indicated.

A plateau (similar spheroid diameter from 5 to 15 days) is nicely visible for spheroids formed from non-malignant HCV29 and transitional cell carcinoma T24 cells (these cells display thick actin bundles in their cytoskeleton, Chapter 6) after five days of culture. For spheroids formed from carcinoma HT1376 cells, a monotonous increase in spheroid diameter is observed. Interestingly, these cells do not display any actin bundles in the cytoskeleton and require the lowest amount of cells/well.

Cell-cell interaction is primarily governed by cadherins [155]; thus, they are crucial for the formation of spheroids. E- and N-cadherins are involved explicitly in spheroid compaction [156]. Therefore, their expression was estimated using the Western blot technique (figure 7.2).

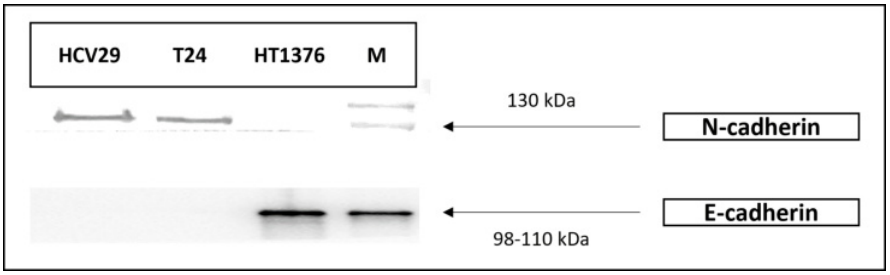

Figure 7.2: **N- and E-cadherin expression obtained from the Western Blot for multicellular spheroids formed by HCV29, T24, and HT1376 cell lines.** N-cadherin was detected at 130 kDa, while E-cadherin related band was at 98-110 kDa.

The Western blot results show that in HT1376 cells, the bands were visible for E-cadherin and not for N-cadherin. The non-malignant HCV29 and transitional cell carcinoma T24 cells display the opposite trend, i.e., N-cadherin was present, while E-cadherin was absent. These results observed for non-malignant HCV29 and cancerous T24 cells are consistent with previous results [157]. It has been shown that E-cadherin contributes to the stabilization of cell contacts [158], which could be the reason behind the different behavior of the spheroids formed by HT1376 cells.

7.3 AFM-studies of aging spheroids

7.3.1 Elastic (Young's) modulus – compressive forces

The mechanical properties were determined for aging spheroids at two growth times, i.e., after 3 and 14 days of culture. The spheroids prepared for AFM measurements were 400 μm in diameter (*detailed preparation of spheroids is described in Materials*). In such a way, the spheroids formed from non-malignant HCV29, transitional cell carcinoma T24, and carcinoma HT1376 cells were measured with an equivalent dimension and similar culture conditions. To get the mechanical response from deeper parts of the spheroids, larger indentations were applied using NSC36 cantilevers (spring constant of 0.6 N/m), which enabled a force of the order of 30 nN. The resulting indentation depth is 6-8 μm. The obtained results show that despite the type of cell lines used to form spheroids, there was a significant increase in Young's modulus after 14 days of culture; however, spheroids composed of cancer cells remained softer than spheroids formed from non-malignant HCV29 cells (figure 7.3).

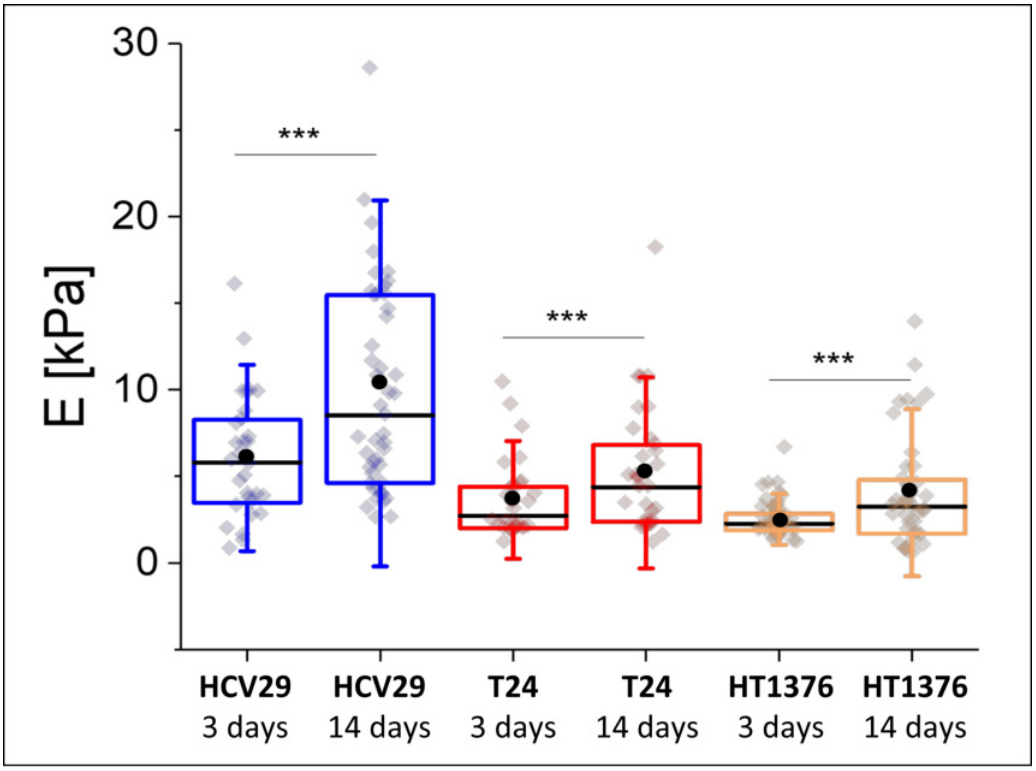

Figure 7.3: **Changes in elastic (Young's) modulus in 3- and 14-day spheroids measured by AFM.** For each cell line, 15 spheroids were measured (2 force maps/spheroid, each point denotes an individual elasticity map). The black dots and lines are the mean and median, respectively; the box denotes standard deviation; error bars represent 10 % and 90 % percentile (*** $p < 0.001$).

The spheroids formed from non-malignant HCV29 cells are characterized by Young's modulus of 6.1 ± 3.5 kPa and 10.6 ± 7.2 kPa for 3- and 14-day spheroids, respectively. Spheroids formed from transitional cell carcinoma T24 cells doubled Young's modulus after 14 days of growth. Spheroids formed from carcinoma HT1376 cells remained the softest, regardless of the culture time. The summary of the obtained results is shown in table 7.1.

Table 7.1: *The determined Young's modulus for spheroids formed from non-malignant HCV29, transitional cell carcinoma T24, and carcinoma HT1376 cells after 3 and 14 days of growth.* The values are expressed as mean ± standard deviation of the mean.

Cell type	**3 days**		**14 days**	
-	**N° maps**	**E [kPa]**	**N° maps**	**E [kPa]**
HCV29	30	6.1 ± 3.5	42	10.6 ± 7.2
T24	30	3.6 ± 2.2	34	6.3 ± 3.7
HT1376	56	2.5 ± 0.9	33	4.4 ± 3.4

In the obtained results, a clear difference is observed between spheroids formed from non-malignant and cancer cells. For 3-day spheroids, p-values were 0.0016 and < 0.0001 unpaired t-tests, for T24 and HT1376 cells, respectively. For 14-day spheroids, the corresponding p-values were 0.0023 and $<$0.0001. While comparing the statistical difference between cancer T24 and HT1376 cells, the p-values were 0.0015 and 0.0324 for 3- and 14-day spheroids, respectively. This analysis concludes that aging can hide the differences between carcinoma HT1376 and transitional carcinoma T24 cells.

7.3.2 Microrheological properties of 3 days and 14 days spheroids by AFM

Various research has demonstrated that microrheological properties are more specific to cancer-related changes [128] [75]. Therefore, like for single bladder cancer cells, microrheological properties were quantified for aging spheroids [more details in section 4.3.5]. Thus, the storage G' and loss G'' moduli were plotted as a function of the frequency of oscillations and fitted with a power-law function (figure 7.4).

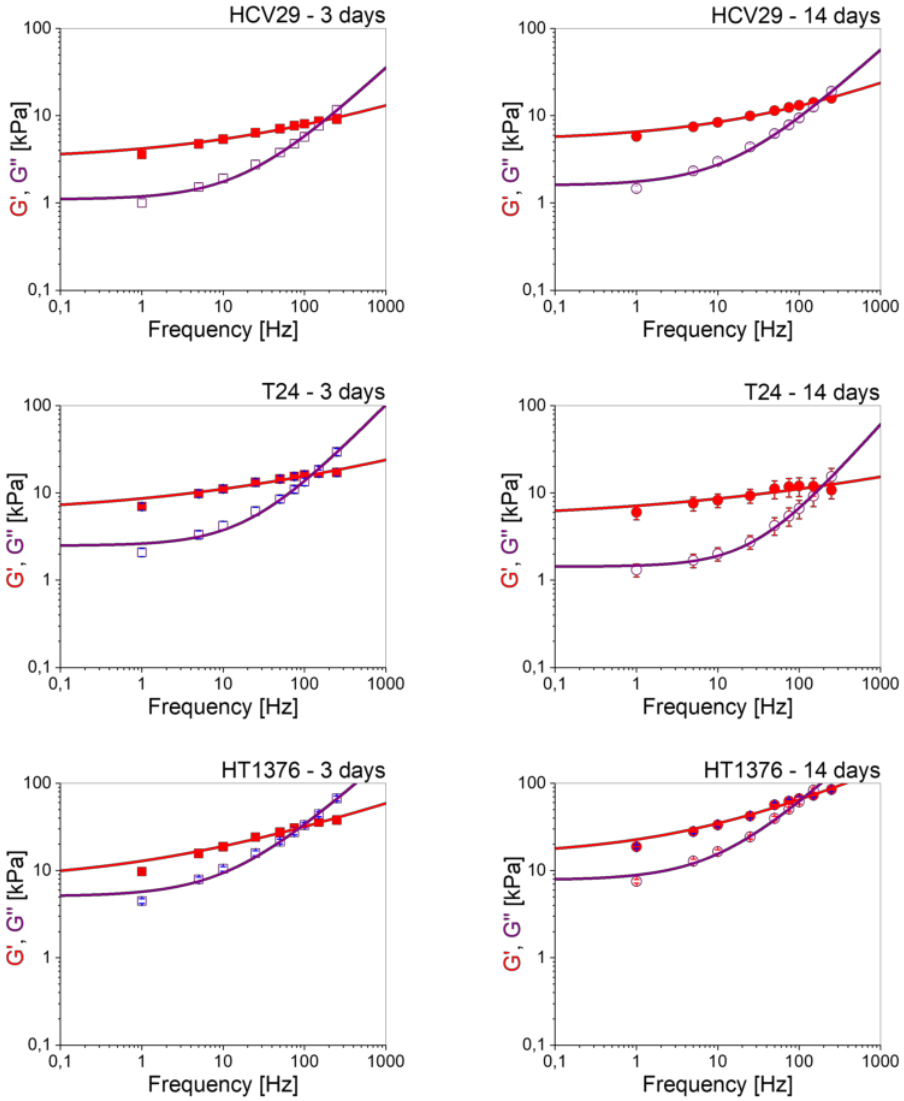

Figure 7.4: **Storage *G'* and loss *G"* modulus plotted as a function of the oscillation frequency for 3- and 14-day spheroids.** The oscillation amplitude was kept constant at 50 nm, and the frequency varied from 1 - 250 Hz. NSC36 cantilevers were applied. Each point denotes the mean ± standard error of the mean. To the data, the power law was fitted (line).

The microrheological properties of aging spheroids showed storage and loss modulus changes in a spheroid-type and time-dependent manner. For spheroids formed from non-malignant HCV29 cells, aging induces stiffening. Both storage and loss moduli increased within the frequency range. For spheroids formed transitional cell carcinoma T24 cells, a softening was obtained. Storage and loss moduli decreased within the frequency range, while for carcinoma HT1376 cells, an opposite behavior was observed. Storage and loss moduli increased within a whole frequency range analogously as for spheroids composed of non-malignant HCV29

cells. By fitting the obtained relationships with the power-law function, such parameters as storage modulus, loss modulus, loss factor, transition frequency, and power law exponent were obtained (table 7.2).

Table 7.2: *Parameters describing microrheological properties of bladder cancer cells, monolayers, and spheroids untreated and treated with 5 μM cytochalasin D, obtained from power-law function fitted to relations between storage (loss) modulus and oscillatory frequency, plotted in figures 6.10 and 6.13.*

	HCV29 (3 days)	HCV29 (14 days)	T24 (3 days)	T24 (14 days)	HT1376 (3 days)	HT1376 (14 days)
G_N' [kPa]	3.11 ± 0.38	5.19 ± 0.41	5.74 ± 1.21	4.95 ± 1.61	7.28 ± 2.05	14.78 ± 2.95
G_N'' [kPa]	1.09 ± 0.09	1.59 ± 0.15	2.49 ± 0.28	1.43 ± 0.11	5.07 ± 0.66	7.79 ± 0.69
Loss factor	0.35 ± 0.09	0.31 ± 0.11	0.43 ± 0.09	0.29 ± 0.02	0.69 ± 0.22	0.53 ± 0.12
ω_T [Hz]	176.50 ± 2.39	183.91 ± 2.99	123.02 ± 5.03	194.89 ± 5.64	87.19 ± 8.58	110.48 ± 15.10
α @ G'(ω)	0.32 ± 0.05	0.38 ± 0.04	0.26 ± 0.06	0.23 ± 0.11	0.32 ± 0.05	0.40 ± 0.05

The storage modulus of HCV29 spheroids from 3.11 ± 0.38 kPa (n = 25 maps, 3-day) to 5.19 ± 0.41 kPa (n = 32 maps, 14-day; p = 0.0007). An analogous change was observed for the loss modulus: from 1.09 ± 0.09 kPa (n = 25 maps, 3-day) to 1.59 ± 0.15 kPa (n = 32 maps, 14-day; p = 0.0013). Despite the increase in storage and loss moduli, the loss factor shows no significant difference between spheroids collected at 3-day and 14-days (0.35 ± 0.09 versus 0.31 ± 0.11). It indicates a similar viscous contribution independent of the spheroid culture time. For cancer spheroids, two distinct ways of changes are observed. For spheroids formed from cancerous T24 cells, longer culture time did not induce significant changes in the storage modulus: 5.74 ± 1.21 kPa (n = 30 maps, 3-day) versus 4.95 ± 1.61 kPa (n = 25 maps, 14 day; p = 0.1849). Interestingly, there is a time-related change in viscous contribution as loss modulus decreases for 14-day spheroids, from 2.49 ± 0.28 kPa (n = 30 maps) to 1.43 ± 0.11 kPa (n = 25 maps; p = 0.0017). Consequently, the loss factor decreased for spheroids from 0.43 ± 0.09 (3-day) to 0.29 ± 0.02 (14-day), pointing to the loss of viscous contribution over this time. Microrheological properties of spheroids formed from carcinoma HT1376 cells resemble that of spheroids formed from non-malignant HCV29 cells. Both storage and loss modulus increased with culture time, from 7.28 ± 2.05 kPa (n = 32 maps, 3-day) to 14.78 ± 2.95 kPa (n = 28 maps, 14-day), and from 5.07 ± 0.66 kPa (n = 32 maps, 3-day) to 7.79 ± 0.69 kPa (n = 28 maps, 14-day), respectively. However, the large values of loss factors, i.e., 0.69 ± 0.22 (3-day) versus 0.53 ± 0.12 (14-day; p = 0.0001), indicate a much larger viscous component as compared to that observed for spheroids composed of non-malignant HCV29 and cancerous T24 cells.

The microrheological parameters, i.e., transition frequency and power-law exponent, were determined to evaluate the effect of aging on spheroids (figure 7.5).

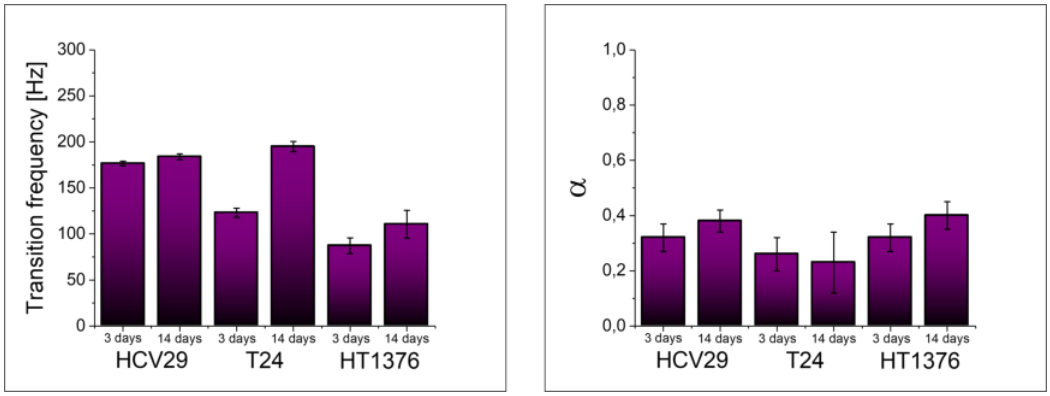

Figure 7.5: **Changes in transition frequency and power-law exponent determined for the aging spheroids formed from bladder cancer cells (after 3 and 14 days of spheroid growth).**

Despite softening and stiffening of spheroids that could be deduced from changes of storage and loss moduli, the transition frequency increased, regardless of the type of cells used to make spheroids. The change for aging spheroids was the smallest for spheroids formed from non-malignant HCV29 cells and larger for spheroids formed from cancerous cell lines. These results support the hypothesis that cancer cells behave like fluid-like materials at frequencies at which non-malignant or healthy cells are still behaving as solid-like [75] [128]. The aging hides the difference between spheroids formed from cells possessing thick actin bundles in their structures, i.e., HCV29 and T24 cells. The transition frequency for these cells was similar, while the transition frequency obtained for spheroids formed from HT1376 cells (no thick actin bundles present in the cell cytoskeleton) remained lower. The power-law exponent turned out to be a parameter burden by a large error, making it less sufficient and non-reliable to describe the microrheological properties of aging spheroids.

7.4 Mechanical properties of bladder spheroids by HFS

The main characteristic of microrheological measurements realized by AFM is their local character limited by the size of the recorded elasticity maps and the level of their averaging. Thus, in parallel to AFM, hydraulic force spectroscopy (*HFS, details about the data analysis are included in section 2.2.3*) was applied to measure the mechanical properties of aging spheroids. The main difference between AFM and HFS is that, in HSF, it is possible to get the signal from a broader area, including several cells. It allows investigation of how cells forming the spheroid behave collectively and how the obtained results are related to the way they are organized and linked to each other in the 3D structure. The spheroids were cultured similarly to the AFM measurements, but they were measured in PBS buffer at room temperature, not in their culture medium like for AFM. The aspirated length of the sample was about 50 μm, and every time a new area was captured with the probe around the spheroid. The elastic modulus calculated from HFS measurements reveals a similar trend as observed in the AFM data (figure 7.6).

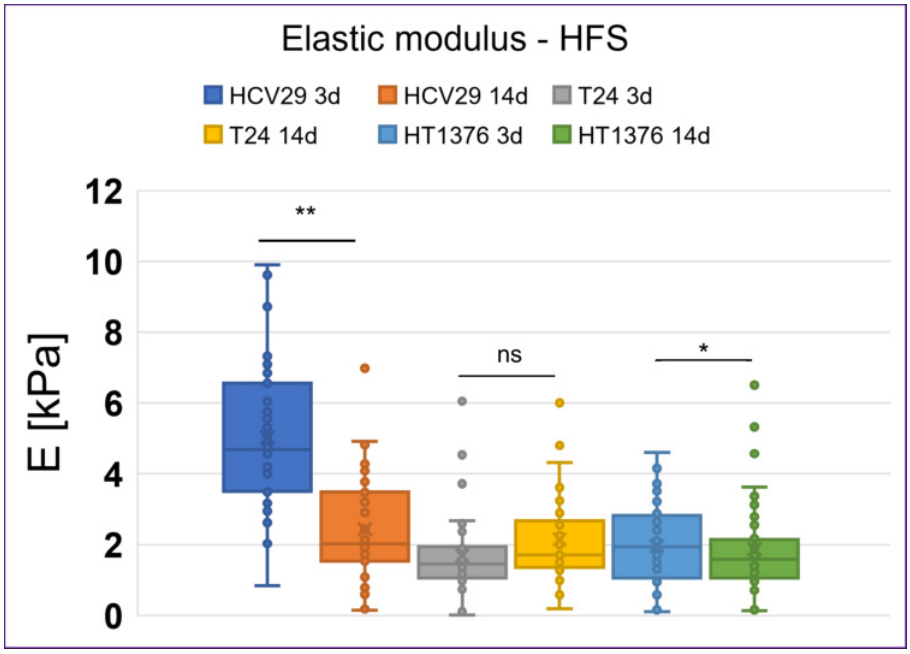

Figure 7.6: **Age-related changes in elastic modulus determined for spheroids formed from distinct bladder cancer cells by HFS.** The aging effect was assessed by comparing spheroids culture for 3 and 14 days. For each spheroids type, 40 elasticity curves were acquired in individual areas around the spheroids within the scan area of 50 μm x 50 μm. The line indicates the median; error bars represent 10 % and 90 % percentile. (*** $p < 0.001$).

Comparison of the mechanical properties of 3-day spheroids showed a similar relation as for the AFM indentation measurements of spheroid mechanical properties. Spheroids formed from non-malignant HCV29 cells were stiffer than spheroids composed from both cancer cells (T24 and HT1376 cells). Moreover, both cancer cells were characterized by similar Young's modulus values analogously as for AFM results. The aging effect was fully distinct from that observed in the AFM results. The AFM results show that Young's modulus increases for spheroids grown for 14 days, regardless of the cell type used to form spheroids, while HFS measurements show cell-type dependent changes in the spheroid Young's modulus (table 7.2).

Table 7.2: *Elastic modulus determined for bladder spheroids based on HFS measurements. Results are expressed as mean ± standard deviation from n = 40 elasticity curves.*

Cell type	3 days	14 days
HCV29	5.03 ± 1.98 kPa	2.44 ± 1.50 kPa
T24	1.69 ± 1.33 kPa	2.15 ± 1.20 kPa
HT1376	1.96 ± 1.16 kPa	1.88 ± 1.31 kPa

The largest decrease was obtained for spheroids composed of HCV29 cells and the smallest for HT1376 cells. Elastic modulus decreased from 5.03 ± 1.98 kPa to 2.44 ± 1.50 kPa ($p = 0.05$). Spheroids composed of HT1376 cells show a small but statistically significant decrease from 1.96 ± 1.16 kPa to 1.88 ± 1.31 kPa ($p = 0.04$). For these spheroids, a softening was observed. HSF results show no significant difference for spheroids composed of T24 cells, i.e., 1.69 ± 1.33 kPa (3-day) versus 2.15 ± 1.20 kPa (14-day; $p = 0.12$).
The discrepancy between AFM and HFS results can be related to probe geometry, averaging over the large area, and age-related changes in the outermost layer of the spheroid.

7.5 Histological analysis of bladder cancer spheroids

Histological analysis of the spheroid sections was conducted to gather information on the spheroids' extracellular matrix (ECM). Three different types of staining were performed: *(1)* hematoxylin and eosin (H&E), *(2)* Masson's Trichrome (MT), and *(3)* Sirius Red (SR). H&E stains the cell nuclei in purple-blue and the cytoplasm in pink. MT staining allows the visualization of the connective tissue (in blue), while collagen can be localized by applying SR (in red). The images from the histological staining are presented in figures 7.7 (HCV29 spheroids) 7.8 (T24 spheroids) 7.9 (HT1376 spheroids).

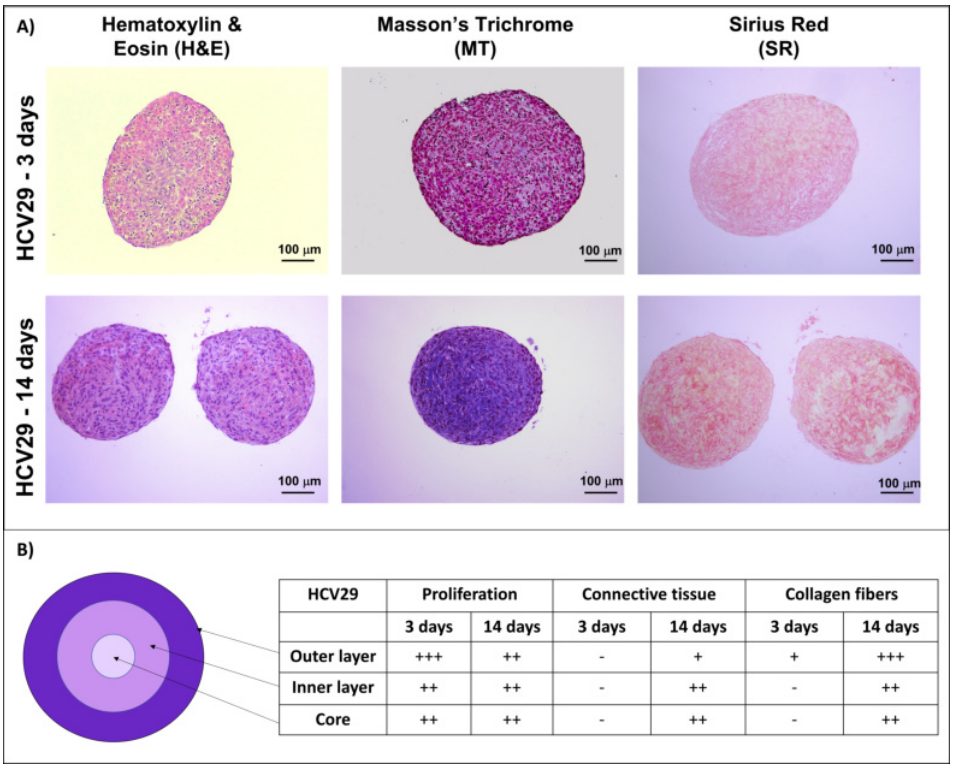

HCV29	Proliferation		Connective tissue		Collagen fibers	
	3 days	14 days	3 days	14 days	3 days	14 days
Outer layer	+++	++	-	+	+	+++
Inner layer	++	++	-	++	-	++
Core	++	++	-	++	-	++

Figure 7.7: **Histological assessment of 3-days and 14-day HCV29 spheroids.** A) Cross-sections of spheroids formed by the non-malignant HCV29 cells, stained with hematoxylin and eosin (H&E), Masson's Trichrome (MT), and Sirius Red (SR). B) Schematic representation of the three layers of a spheroid and the corresponding table with the relative range of proliferation, presence of connective tissue, and collagen fibers for the 3-days and 14-day spheroids.

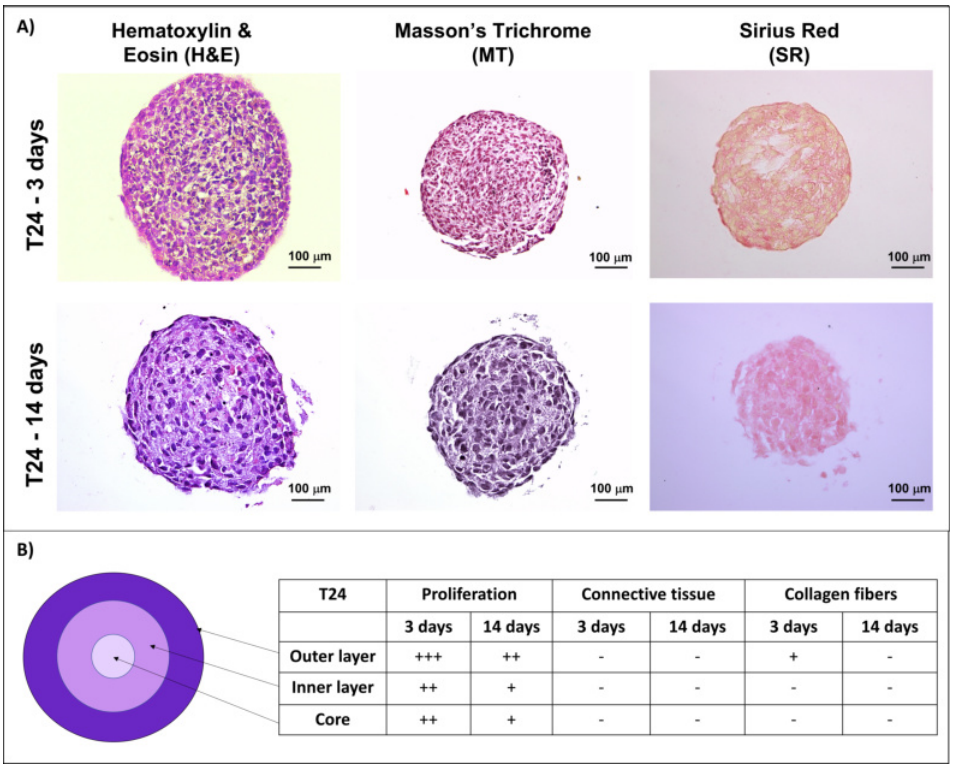

T24	Proliferation		Connective tissue		Collagen fibers	
	3 days	14 days	3 days	14 days	3 days	14 days
Outer layer	+++	++	-	-	+	-
Inner layer	++	+	-	-	-	-
Core	++	+	-	-	-	-

Figure 7.8: **Histological assessment of 3-days and 14-days T24 spheroids.** A) Cross-sections of spheroids formed by the transitional cell carcinoma T24 cells, stained with hematoxylin and eosin (H&E), Masson's Trichrome (MT), and Sirius Red (SR). B) Schematic representation of the three layers of a spheroid and the corresponding table with the relative range of proliferation, presence of connective tissue, and collagen fibers for the 3-days and 14-day spheroids.

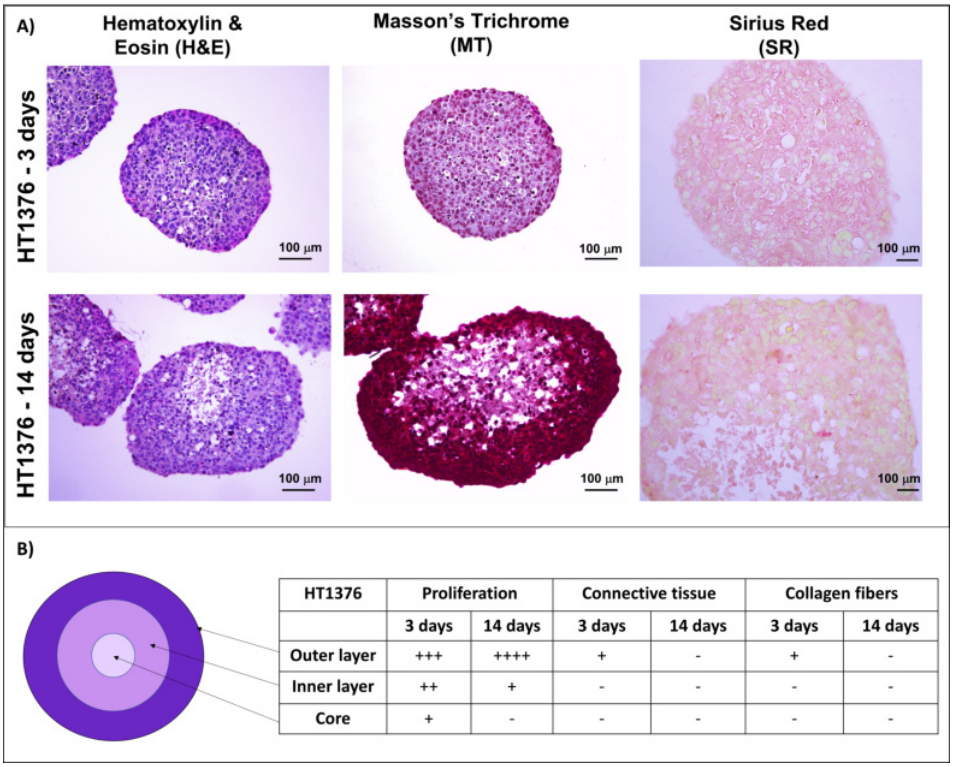

HT1376	Proliferation		Connective tissue		Collagen fibers	
	3 days	14 days	3 days	14 days	3 days	14 days
Outer layer	+++	++++	+	-	+	-
Inner layer	++	+	-	-	-	-
Core	+	-	-	-	-	-

Figure 7.9: **Histological assessment of 3-days and 14-days HT1376 spheroids.** A) Cross-sections of spheroids formed by the carcinoma HT1376 cells, stained with hematoxylin and eosin (H&E), Masson's Trichrome (MT), and Sirius Red (SR). B) Schematic representation of the three layers of a spheroid and the corresponding table with the relative range of proliferation, presence of connective tissue, and collagen fibers for the 3-days and 14-day spheroids.

The main information that could be gained from the above histological images are:

- The internal structure of a multicellular spheroid is visible in all the analyzed samples. An outer layer is defined by the highly proliferating cells indicated by the high density of cell nuclei in that region. The inner spheroid layer with less dense nuclei may indicate a quiescent area characterized by a less proliferating rate. The core of the 3-day spheroids still exhibits proliferating cells, even if in a lower amount compared to the other two layers.

- In spheroids formed by HCV29 and T24 cells, the number of cell nuclei after 3 days of culture is much higher than after 14 days of growth, which can be associated with the growth pattern of these spheroids, as shown in figure 7.1. In the beginning, the cells grow and divide fast, and afterwards, cells divide slowly, allowing them to form a stable spheroid structure (the plateau). Unlike these two, the HT1376 spheroids show a higher density of cell nuclei in the outer layer of the 14-day cross-sections, a sign of their continuous proliferation and enlargement over time.

- The necrotic core is visible neither in spheroids formed from non-malignant HCV29 cells nor in spheroids formed from cancer T24 cells, even after 14 days of culture. It appears only in spheroids formed from HT1376 cells after 14 days of culture. These spheroids are characterized by the presence of well-defined circular structures here and there in the inner area (indicated in red in figure 7.9), which could be some forms of vacuoles that initiates the formation of the necrotic area.

- The connective tissue, particularly the collagen fibers (obtained from the MT and SR staining), are present mainly in 14-day spheroids composed of non-malignant HCV29 cells.

The differences in the elastic modulus that were observed with the HFS measurements for the 14-day spheroids formed by the non-malignant HCV29 cells and the carcinoma HT1376 cells can be associated with the presence of connective tissue in HCV29 spheroids and the necrotic core in HT1376 spheroids, that somehow change the cell-cell interactions that reflect in the observed softening during the aging process.

7.6 Actin organization in aging spheroids

To further explain the differences between the results obtained from both AFM and HFS measurements, the organization of the actin cytoskeleton for cells forming the spheroids was visualized by a confocal microscope. F-actin (a polymerized form of actin) was stained with phalloidin conjugated with Alexa Fluor 488 (figure 7.10).

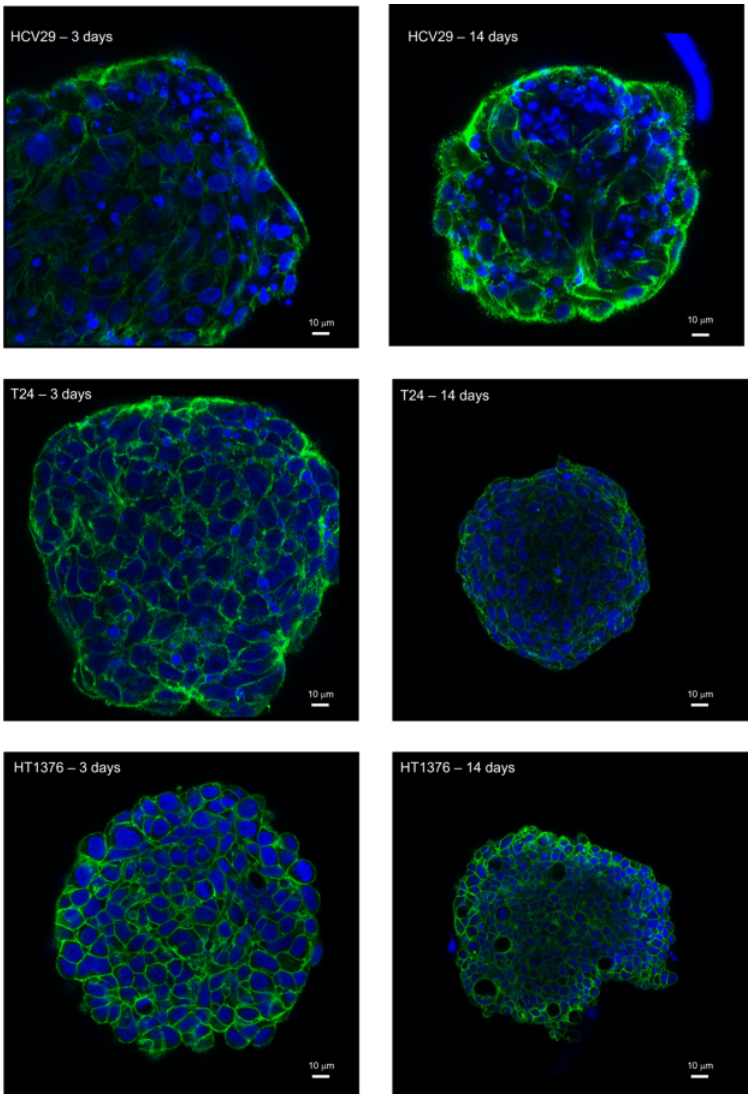

Figure 7.10: **Confocal images of bladder cancer spheroids recorded for spheroids cultured for 3 and 14 days.** Staining: blue (nucleus) – Hoechst 33342, green (F-actin) – phalloidin conjugated with Alexa Fluor 488. One slice from the Z-stack of each cell line is presented. The scale bar is 10 μm.

As already described in chapter 6, when cells are cultured as spheroids, F-actin is mainly grouped around the cells. It is still possible to see some actin fibers in

the 3-day spheroids formed by HCV29 and T24, while the HT1376 spheroids are nicely organized in a shell-like manner.
Interestingly, there are clear effects of aging in the 14-day HCV29 spheroids: the actin cytoskeleton is organized irregularly compared to the 3-day spheroids, and there are cells with a condensed nucleus (smaller size and much more intense blue signal), a sign of apoptotic cells. Again, this is consistence with the fact that after 14 days of culture, the diameter of HCV29 reduces, meaning that cells are not dividing as in the initial phase of growth. As for the spheroids formed by T24 spheroids, there is no significant difference in the actin organization between 3-days and 14-days. Regarding the spheroids formed by HT1376 cells, it is worth mentioning that the vesicle structures observed in the histological staining are also evident in these confocal images. Those circular structures could indicate the necrotic core's establishment.

7.7 Mechanics of aging spheroids - summary

Tumor spheroids grow similarly to solid tumors; therefore, they are the perfect model system mimicking cancer progression. Lots are known about tumor growth from the biological point of view [41] [43] [46], but their biophysical properties are less studied. Therefore, this chapter focused on the mechanical and microrheological properties of the aging process in spheroids. Spheroids collected at 3 and 14 days of culture were used as a model to mimic the early (3-day) and late (14-day) stages of tumor formation. The changes in the biophysical properties of cells during cancer progression were investigated in correlation with the internal structure of the multicellular spheroids.

The growth of the spheroids formed from the three studied bladder cancer cells was monitored over 15 days. Only the spheroids formed by HCV29 and T24 cells presented a growth pattern like that for solid tumors, with a fast initial growth phase followed by a plateau. At the former, the spheroid diameter increased linearly with time, while at the latter, the diameter remained constant. Spheroids formed by HT1376 cells monotonously increased diameter with culture time. These differences can be related to the different cadherin expressions in these cell lines: HCV29 and T24 cells expressed N-cadherin, while HT1376 cells expressed only E-cadherin.

The mechanical and microrheological properties of bladder cancer spheroids were determined at different scales, i.e., locally probed with the AFM and globally by employing HFS. The AFM results show the increased rigidity of spheroids

collected at 14-day, regardless of the type of cells used to form them. However, regardless of the days of culture, the spheroids composed of cancer cells, T24 and HT1376 cells, were softer and more deformable than those formed from non-malignant HCV29 cells. Additionally, the results from the microrheological measurements by AFM confirmed the more fluidic-like behavior of cancer spheroids with respect to those composed of non-malignant HCV29 cells. It was also confirmed that spheroids formed from HT1376 cells are the most viscous among the three, showing the highest value of loss factor and the lowest value of the transition frequency, both for spheroids collected at day 3 and 14.
The HFS measurements showed a decrease in the elastic modulus for spheroids composed of HCV29 and HT1376 cells cultured for 14 days and no significant difference between 3-day and 14-day T24 spheroids. This result is opposite to the AFM one. Notwithstanding, also, in this case, the cancerous cell lines were proved to be more deformable than the non-malignant cell line.

To understand the mechanical differences observed in the three types of spheroids, their inner structure was assessed using histological staining. It was seen that the spheroids formed by HCV29 cells produced ECM and presented collagen fibers after 14 days of culture. The HT1376 14-day spheroids were the only ones characterized by the presence of a necrotic core. These features could explain the softening of the spheroids formed by these two cell lines observed by HFS. This suggests that the cell-cell and cell-ECM interactions may play a key role in determining the mechanical properties of the spheroids. On the contrary, as for the mechanical results from HFS, also from the histological images of T24 spheroids, no relevant differences were observed between 3-days and 14-days spheroids.

Chapter 8

Effects of docetaxel on mechanical properties of bladder spheroids

8.1 Objectives

One of the main applications of multicellular spheroids is in the drug discovery field, as they are known to be good *in vitro* models for mimicking solid tumors. In this part of the study, spheroids made from the bladder cancer cell lines were treated with docetaxel (DTX), an anticancer drug that is very well used to treat several types of cancer, including bladder cancer. The main purpose of the current part of the study is to understand the mechanical alterations caused by this drug on the spheroids. For this aim, HFS was used. Figure 8.1 shows the schematic representation of the timeline of the experiments conducted.

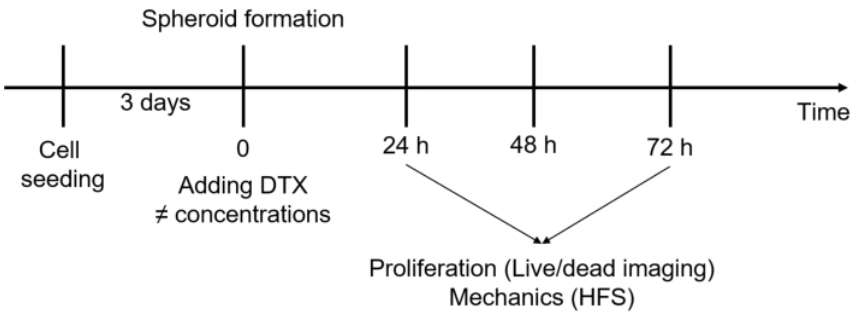

Figure 8.1: **Timeline of the DTX treatment.** The spheroids cultured for 3 days were treated with DTX at the desired concentration, and then after 24 hours and 72 hours of treatment, the effects of the drug were tested with live/dead staining, while the mechanical properties were determined using HFS.

8.2 Microtubule distribution in bladder cancer cells

In this study, bladder cancer spheroids were treated with docetaxel, an anti-tumor compound stabilizing the microtubules. In the first step, the microtubule organization and the actin cytoskeleton inside the studied bladder cancer cells, cultured both as 2D and 3D, were visualized using a confocal microscope. The exemplary confocal images are shown in figure 8.2.

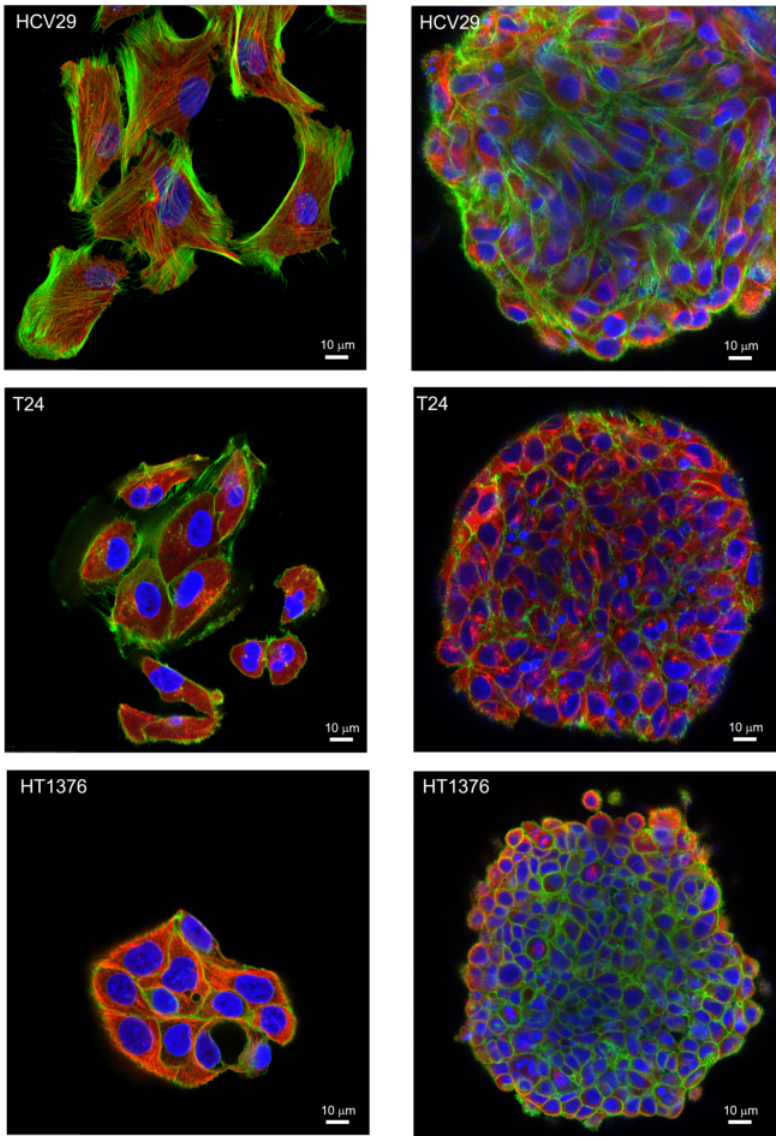

Figure 8.2: **Confocal images of cytoskeletal elements present in bladder cancer cells (2D versus 3D).** Staining: cell nucleus (blue) – Hoechst 33342, F-actin (green) – phalloidin conjugated with Alexa Fluor 488, and microtubules (red) – anti-β-Tubulin-Cy3. On the left, the cells cultured in the 2D, and on the right, the corresponding 3D spheroids are represented. The scale bar is 10 μm.

The actin cytoskeletal organizations observed in the above confocal images from the three cell lines are the same as those obtained previously (figures 6.1 & 6.2). The non-malignant HCV29 and transitional cell carcinoma T24 cells present well-differentiated actin filaments, with the presence of thick actin bundles in higher quantities in HCV29 cells. Carcinoma HT1376 cells display a much lower amount of actin and no evidence of any thick actin bundles. When moving to the 3D structures, F-actin is mainly distributed around the cells. In particular, it is organized in a shell-like shape to the cells forming the HT1376 spheroids. Meanwhile, in HCV29 spheroids, some thick actin bundles are still spanning over the cells. The microtubules are evenly distributed in the three cell lines, cultured both as 2D and 3D. Thus, the organization of the microtubules in the untreated cells is nicely preserved in the three bladder cancer cell lines. Importantly, the confocal imaging showed that the penetration of the staining dyes is limited to the surface layer of the spheroids. This is similar to the reduced drug penetration effect observed when moving from the outside to the inside of the spheroids [159].
Interestingly, from confocal images, it was possible to observe the ongoing mitosis (cell division) in the cells present in the outer layer of spheroids, a clear sign of active proliferation. An exemplary image is shown for the cells forming the HT1376 spheroids (figure 8.3).

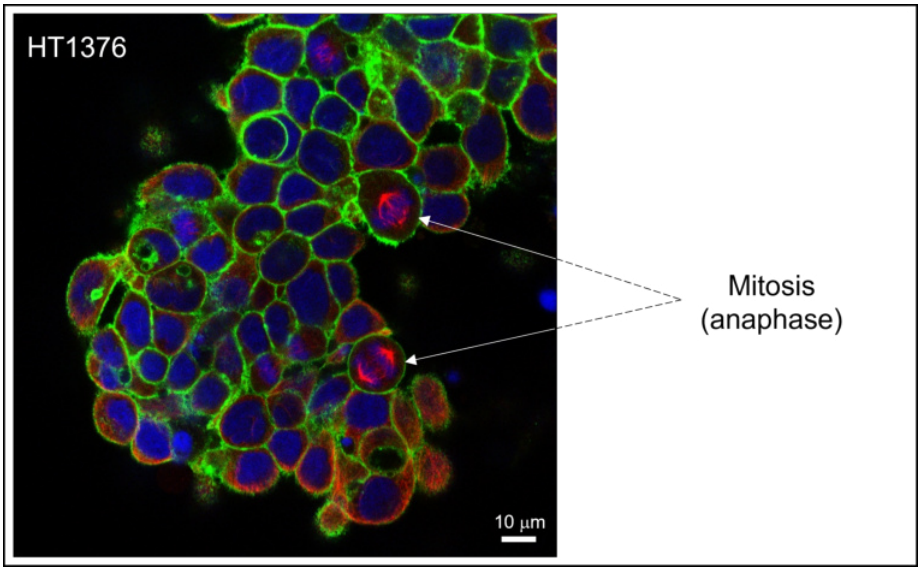

Figure 8.3: **Confocal image of HT1376 spheroid, showing ongoing mitosis.** The cytoskeletal structure of the spheroid is shown. Staining: cell nucleus (blue) – Hoechst 33342, F-actin (green) – phalloidin conjugated with Alexa Fluor 488, and microtubules (red) – anti-β-tubulin-Cy3. The scale bar is 10 μm.

In the outer layer of the spheroid, ongoing cell division is observable by the

presence of cells in anaphase of mitosis, which is represented by the separating nucleus (blue) and the microtubule filaments located at each pole of the cell (red).

8.3 Effects of DTX treatment on bladder cancer spheroids

Until now, there have been very few studies on the effects of DTX on bladder cancer cell lines used in the current study, and they were all conducted on cell monolayers [160] [161]. From those studies, it is known that the EC50 of DTX (concentration required to obtain the 50 % effect of a drug) for HT1376 cells is 4.2 nM and 3.8 nM for the T24 cells. There are no data to refer to the HCV29 cell line. Therefore, some preliminary experiments needed to be done to assess the toxicity level of the drug on the three bladder spheroids. The MTS test performed on spheroids did not give successful results. In the first attempt, the test was done on single spheroids, which gave a very low intensity of absorbance, and most of the time, it was impossible to get any signal at all. Afterwards, 10 spheroids were pooled together, and an MTS test was done on them, giving a higher signal intensity. Despite this, it was not always possible to fit the data to a sigmoidal function and obtain the EC50 (app-chapter8). For this reason, in parallel, the effects of DTX on spheroids were analyzed by observing the light and live/dead images acquired after each time point (24 and 72 hours) at the various concentrations of the drug (figures 8.4 - 8.6).
The easiest way to observe the effects of DTX on spheroids is by checking their size after every dose of treatment. In the case of the three bladder cancer spheroids, by using low concentrations close to EC50 obtained in cell monolayers, it was impossible to observe any significant changes in the spheroids. Therefore, higher concentrations of DTX were used. Moreover, the treatment was monitored immediately after the treatment (24 hours) and after 72 hours to observe the spheroid response to longer exposure to the drug. A common observation for all types of spheroids is that after 72 hours, there was a clear increase in the number of dead cells (red signal from live/dead images).

In figure 8.4, the results from HCV29 spheroids are shown.

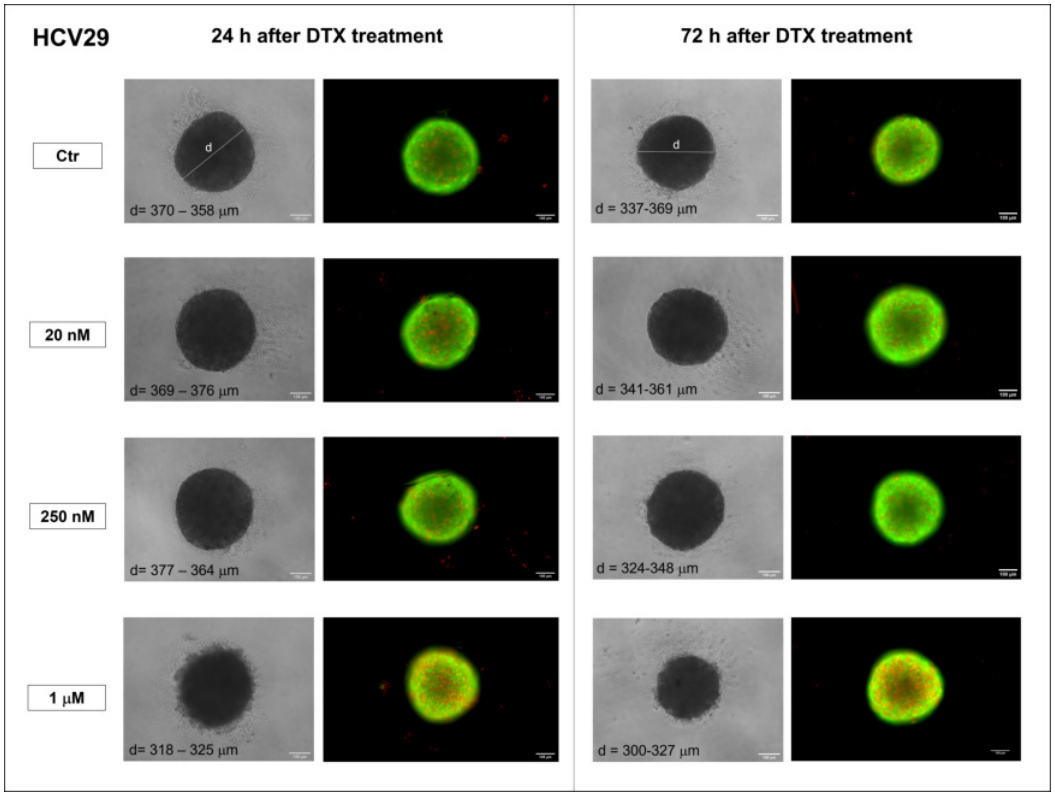

Figure 8.4: **Analysis of live/dead cells from spheroids formed by non-malignant HCV29 cells.** Spheroids were treated with different concentrations of DTX, a microtubule-stabilizing anticancer drug. After 24 and 72 hours from the treatment, cells were stained with a solution containing calcein (live cells – green) and propidium iodide (dead cells - red). Images were taken using light and fluorescence microscopes. Treatment with DTX caused an increased number of dead cells (red) at high drug concentrations. The scale bar is 100 μm, and the spheroid diameter is indicated after each treatment with DTX.

For spheroids formed by non-malignant HCV29 cells, up to for concentrations of 250 nM DTX, there were no significant changes in the size after neither 24 hours nor 72 hours. A clear sign of disruption appears at 1 μM DTX. Thus, the spheroids formed by HCV29 required a high dosage to show some effects visually.

In figure 8.5, the results for the spheroids formed by T24 cells are shown.

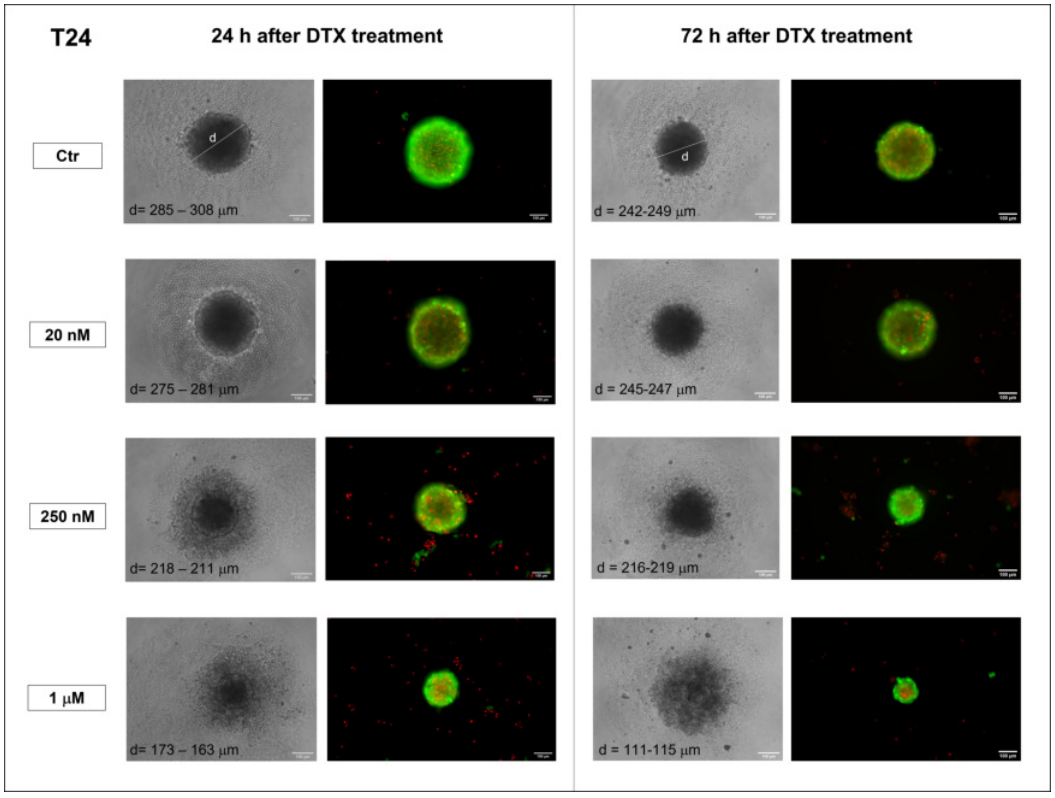

Figure 8.5: **Analysis of live/dead cells from spheroids formed by transitional cell carcinoma T24 cells.** Spheroids were treated with different concentrations of DTX, a microtubule-stabilizing anticancer drug. After 24 and 72 hours from the treatment, cells were stained with a solution containing calcein (live cells – green) and propidium iodide (dead cells - red). Images were taken using light and fluorescence microscopes. Treatment with DTX caused an increased number of dead cells (red) at high drug concentrations. The scale bar is 100 μm, and the spheroid diameter is indicated after each treatment with DTX.

The spheroids formed by the transitional cell carcinoma T24 cells had a continuous decrease in diameter starting from treatment with 20 nM DTX. After continuous exposure to the drug, unlike the other two types of spheroids, T24 spheroids did not maintain their size, and their diameter kept decreasing with the dosage increase. In particular, at the two highest concentrations, they became so small that little information could be obtained regarding their structure.

Figure 8.6 illustrates the effects of DTX on HT1376 spheroids.

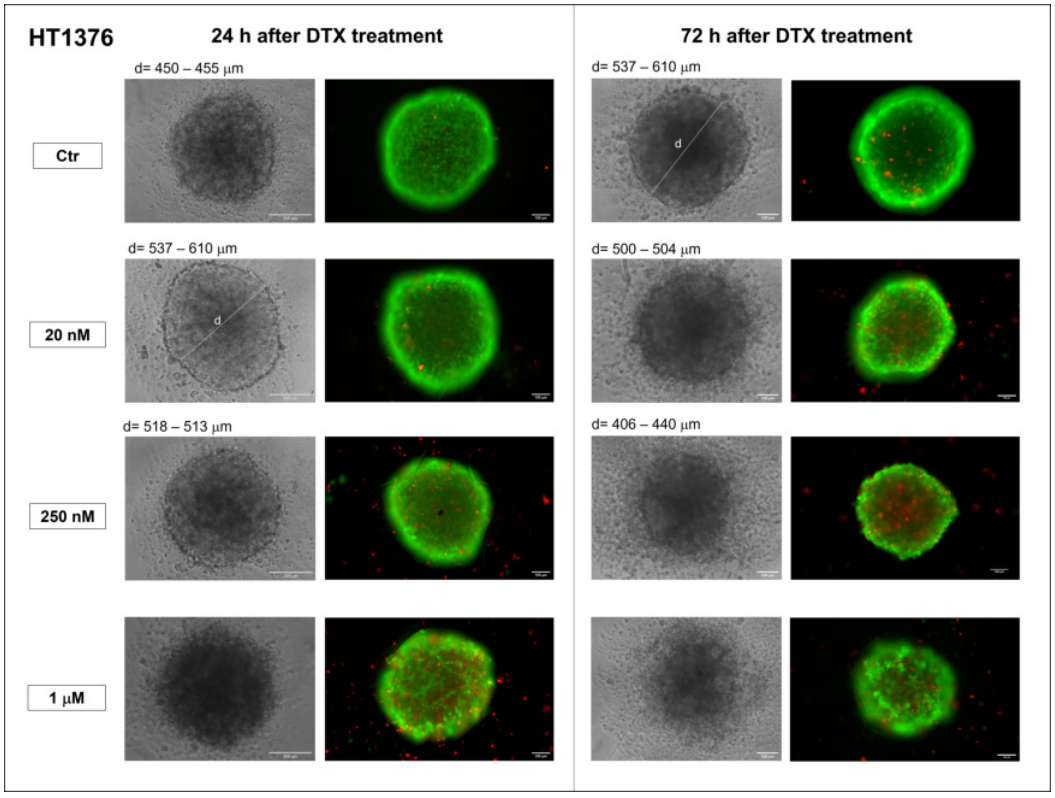

Figure 8.6: **Analysis of live/dead cells from spheroids formed by carcinoma HT1376 cells.** Spheroids were treated with different concentrations of DTX, a microtubule-stabilizing anticancer drug. After 24 and 72 hours from the treatment, cells were stained with a solution containing calcein (live cells – green) and propidium iodide (dead cells - red). Images were taken using light and fluorescence microscopes. Treatment with DTX caused an increased number of dead cells (red) at high drug concentrations. The scale bar is 100 μm, and the spheroid diameter is indicated after each treatment with DTX.

Similar to HCV29 spheroids, those formed by HT1376 did not have significant effects at low dosage, but their structure changed at a smaller concentration compared to the HCV29 spheroids, 250 nM. Interestingly, these spheroids also did not change their size after long exposure to low concentrations of DTX.

8.4 Viscoelastic properties of DTX-treated spheroids by HFS

The analysis of live/dead images allowed a qualitative comparison between the three spheroids and observe the visible effects of DTX on their structure at different concentrations. Based on this information, the concentrations of DTX used for the mechanical measurements by HFS were chosen differently for each cell line. For instance, in spheroids formed by HCV29, there were no significant effects for concentrations lower than 1 μM. Thus, for these cell lines, the measurements were done from 5 nM to 1 μM concentration. Differently, for the spheroids formed by T24 cells, the HFS measurements were done from 5 nM to 250 nM. Moreover, for HT1376, 1nM to 500 nM dosages were used.

The measurements by HFS were performed in the time domain (details in chapter 2), and two parameters were chosen to describe the viscoelastic properties of the treated and not-treated spheroids: fluidity index, α, and the fractional compliance, A. The two parameters are interdependent. When α equals 0, the material is purely elastic, while when α equals 1, the material is purely viscous.

The results for the spheroids formed by the non-malignant HCV29 cells are shown in figure 8.7

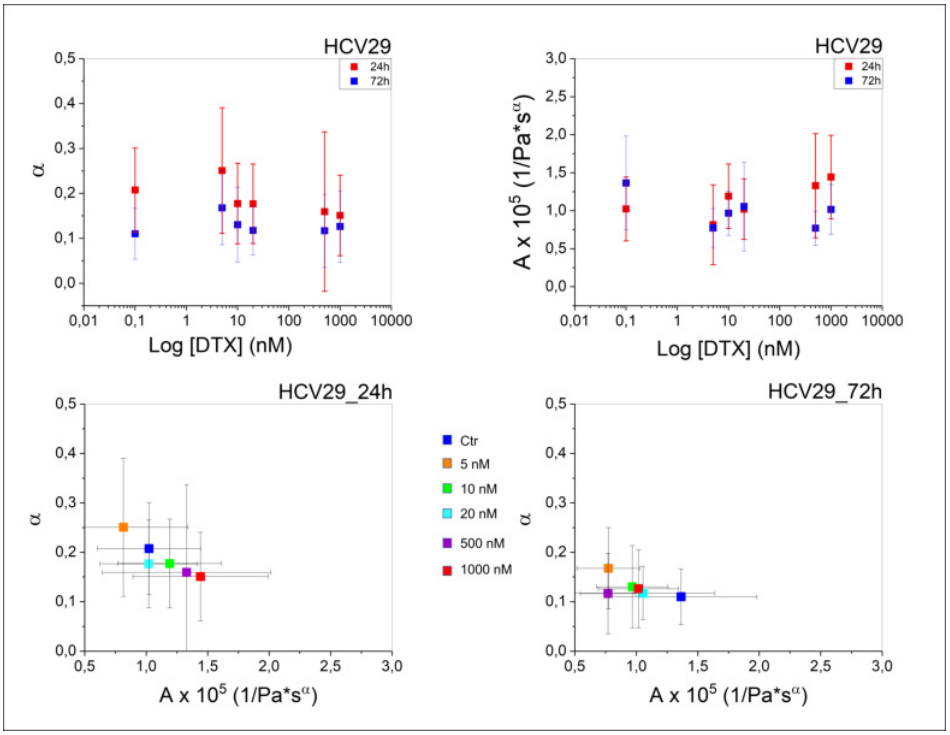

Figure 8.7: **Viscoelastic properties of bladder cancer spheroids formed by non-malignant HCV29 cells.** Spheroids were treated with several concentrations of DTX (from 5 nM to 1000 nM). After 24 and 72 hours, time domain viscoelasticity measurements were performed using HFS. The fluidity index (α) and the fractional compliance (A) are plotted in function of the DTX concentration (1-2), in logarithmic scale, where 0.1 corresponds to the untreated cells (ctr). The fluidity index (α) was plotted in relation to the fractional compliance (A) after 24 hours (3) and 72 hours (4) of treatment with DTX. Each point denotes the mean ± standard deviation of the mean calculated from 10 spheroids (2 measurements/spheroid).

When considering the values of the fluidity index and the fractional compliance, there is an overall tendency to decrease after 72 hours of treatment, indicating that the cells are becoming more solid-like upon prolonged treatment with DTX. Looking into the plots showing the values of the fluidity index in relation to the fractional compliance, the spheroids treated with DTX, after 72 hours, show a shift towards the value corresponding to that of the initial untreated spheroids, indicating a clear return to the original viscoelasticity. The significance of this shift was confirmed by doing an unpaired t-test, which showed that the results were very significant for the low concentrations of DTX.

The HFS results for the cancer T24 spheroids are shown in figure 8.8

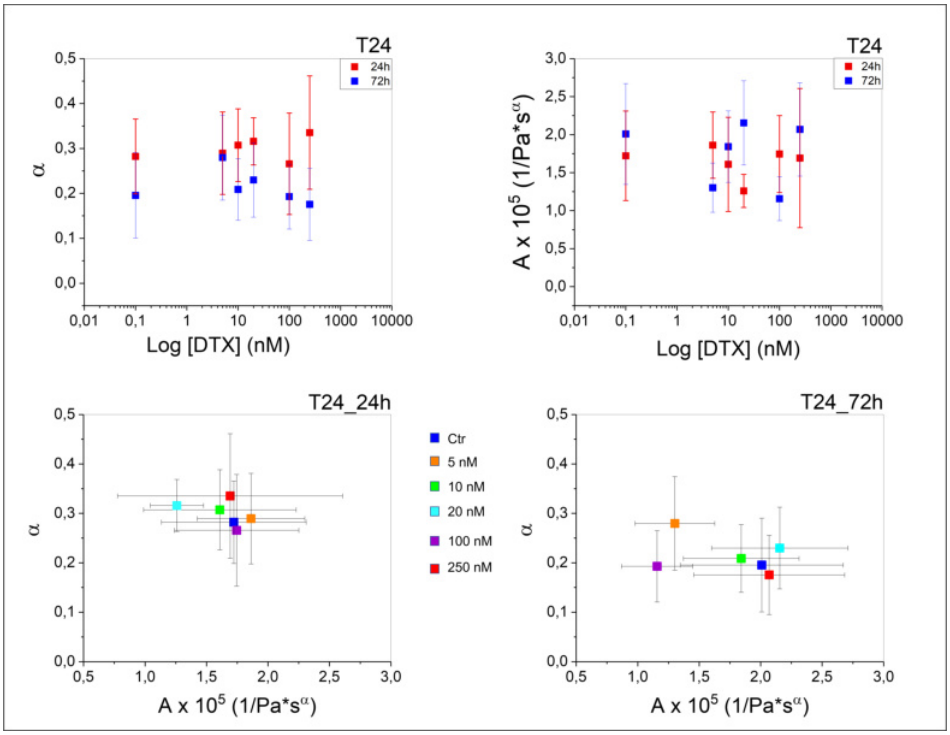

Figure 8.8: **Viscoelastic properties of bladder cancer spheroids formed by transitional cell carcinoma T24 cells.** Spheroids were treated with several concentrations of DTX (from 5 nM to 250 nM). After 24 and 72 hours, time domain viscoelasticity measurements were performed using HFS. The fluidity index (α) and the fractional compliance (A) are plotted in function of the DTX concentration (1-2), in logarithmic scale, where 0.1 corresponds to the untreated cells (ctr). The fluidity index (α) was plotted in relation to the fractional compliance (A) after 24 hours (3) and 72 hours (4) of treatment with DTX. Each point denotes the mean ± standard deviation of the mean calculated from 10 spheroids (2 measurements/spheroid).

The spheroids formed by T24 cells do not show a clear pattern on the fluidity index and compliance, neither depending on the concentrations of DTX nor the two analyzed time points. Their values are distributed irregularly, which does not clearly explain the mechanical effects of DTX in these cells. From live/dead images, the number of dead cells increased by increasing the drug concentration and exposure time. However, it is hard to correlate the observed effects with the results from HFS.

Finally, the results from the spheroids formed by cancer HT1376 cells are shown in figure 8.9

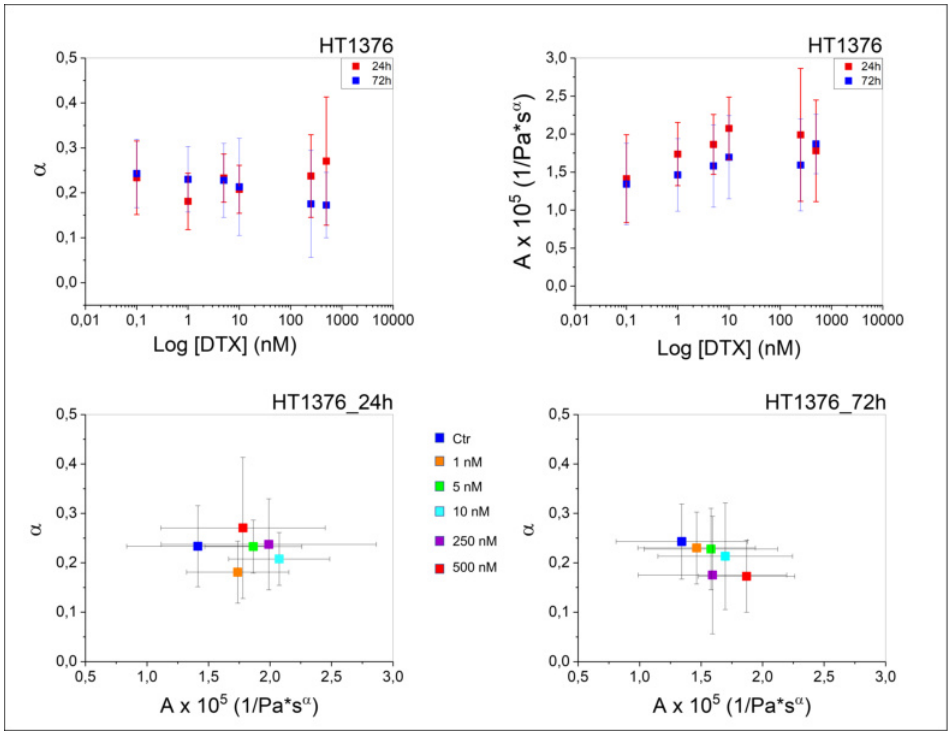

Figure 8.9: **Viscoelastic properties of bladder cancer spheroids formed by carcinoma HT1376 cells.** Spheroids were treated with several concentrations of DTX (from 1 nM to 500 nM). After 24 and 72 hours, time domain viscoelasticity measurements were performed using HFS. The fluidity index (α) and the fractional compliance (A) are plotted in function of the DTX concentration (1-2), in logarithmic scale, where 0.1 corresponds to the untreated cells (ctr). The fluidity index (α) was plotted in relation to the fractional compliance (A) after 24 hours (3) and 72 hours (4) of treatment with DTX. Each point denotes the mean $\pm$ standard deviation of the mean calculated from 10 spheroids (2 measurements/spheroid).

From the live/dead images, it was clear that the structure of HT1376 spheroids was compromised at high concentrations of DTX. Apart from this, when looking at the data from the low concentrations of DTX, interestingly, the values of the fluidity index are very similar for 24 hours and 72 hours, indicating that there is no difference in the viscoelastic properties of these spheroids at the two time points. Moreover, this is the only cell line where the untreated cells show the exact value of the fluidity index at 24 h and 72 h. It was not the case in HCV29 and T24 spheroids. It could be because both HCV29 and T24 cells go through compaction, a reduction in their size, over time. In addition, previously, it was shown that HCV29 spheroids produce ECM. Therefore, the cell-cell and cell-ECM interactions may change after 72 hours also in the untreated spheroids, which could explain the differences observed in their viscoelasticity indexes.

To further understand the HFS results, confocal images were taken after 24 hours (figure 8.10) and 72 hours (figure 8.11) of DTX treatment at concentrations ranging from 1 nM to 250 nM.

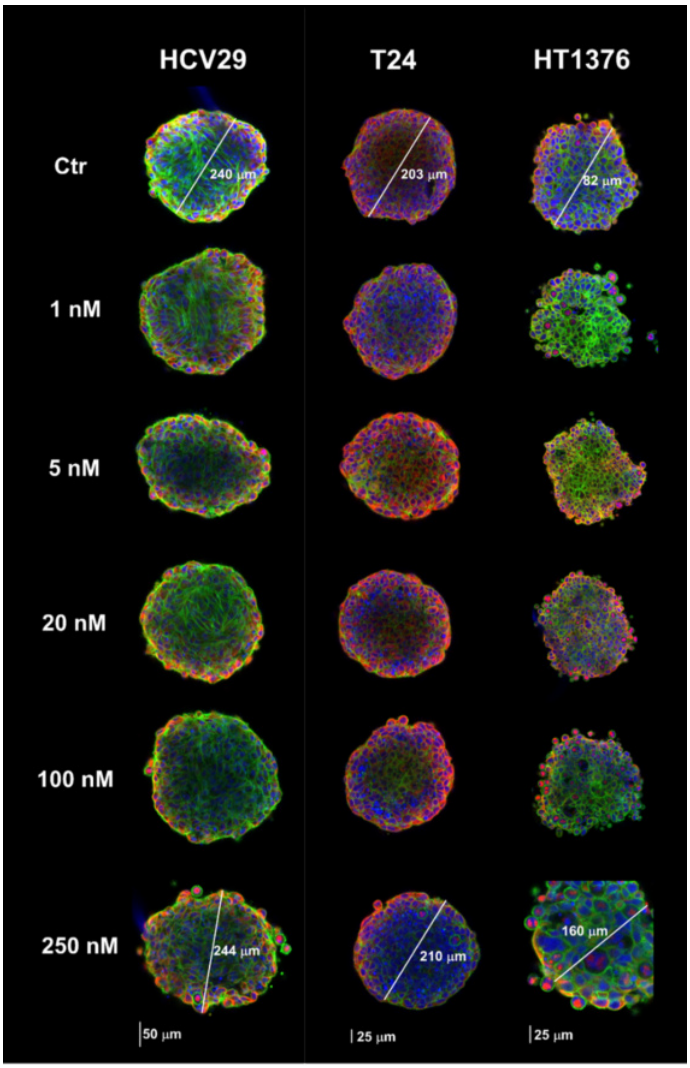

Figure 8.10: **Confocal images of cytoskeletal elements present in bladder cancer cells upon 24-hours DTX treatment.** Spheroids formed by HCV29 (non-malignant), T24 (transitional cell carcinoma) and HT1376 (carcinoma) cells were treated with different concentrations of DTX (from 1nM to 250 nM). After 24 hours, images were taken using the confocal microscope. The cellular structures are shown. Staining: cell nucleus (blue) – Hoechst 33342, F-actin (green) – phalloidin conjugated with Alexa Fluor 488 and microtubules (red) – anti-β-Tubulin-Cy3.

At 24 hours of treatment, as expected, there are no differences in the cytoskeletal organization of spheroids formed by HCV29 cells. In spheroids formed by T24 cells, it is possible to see an overall increase of dead cells at the dosage

increase, especially at 250 nM concentration. Moreover, it is possible to see that the intensity of the red signal is higher here, compared to the other two cell lines, probably due to the easier penetration of the staining dye. However, it is difficult to compare the microtubule organization of the spheroids treated with the different concentrations of DTX. In the spheroids formed by HT1376 cells, even those treated with 1nM DTX, it is possible to see that the microtubule structure is disrupted. The effects of the drugs are more prominent at higher concentrations. It is noticeable that the spheroids treated with 250 nM DTX have a destroyed structure. The signature shell-like structure of HT1376 spheroid is no more present after the treatment with DTX. Unfortunately, confocal images were also taken after 72 hours of DTX treatment, only for two concentrations, one low (1 nM) and one high (250 nM). Representative images are shown in figure 8.11.

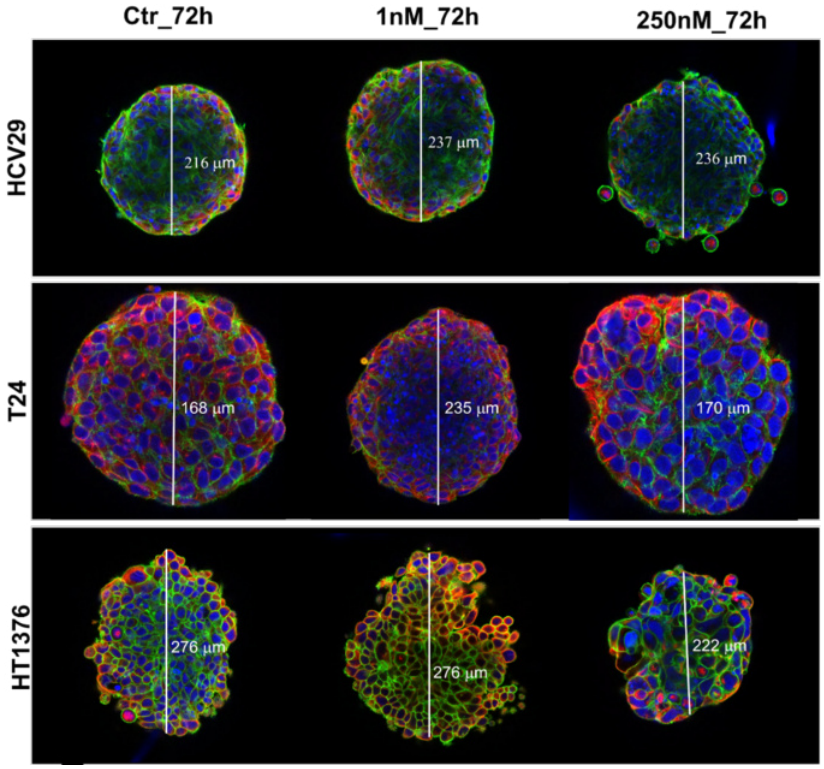

Figure 8.11: **Confocal images of cytoskeletal elements present in bladder cancer cells upon 72-hours DTX treatment.** Spheroids formed by HCV29 (non-malignant), T24 (transitional cell carcinoma) and HT1376 (carcinoma) cells were treated with different concentrations of DTX (from 1nM to 250 nM). After 72 hours, images were taken using the confocal microscope. The cellular structures are shown. Staining: cell nucleus (blue) – Hoechst 33342, F-actin (green) – phalloidin conjugated with Alexa Fluor 488 and microtubules (red) – anti-β-Tubulin-Cy3. The diameter of each spheroid is indicated.

From the confocal images, after 72 hours upon treatment with DTX, it is evident that, for spheroids formed by HCV29 and HT1376 cells, the cytoskeletal organization is similar to the one seen in the spheroids observed after 24 hours of treatment. Unlike these two, T24 spheroids treated with 250 nM DTX show a worsening in the effects of the drug compared to 24 hours, with much more apoptotic nuclei.

8.5 Effects of DTX on mechanics of bladder spheroids - summary

In this final chapter, the bladder cancer spheroids formed by HCV29, T24, and HT1376 cells were treated with different concentrations of DTX, and their viscoelastic properties were elaborated using HFS. Using live/dead images and confocal images, the drug effects on the spheroid structure were studied. It was observed that spheroids formed by HCV29 required a very high amount of the drug to see changes in their structure visibly. It could be related to the fact that these cells produce ECM; thus, they cause difficulties in drug penetration, affecting only the outer layer of the spheroid. Moreover, even after continuous treatment with DTX, these spheroids maintained their shape and size. It could be explained by the fact that the cells underneath the superficial layer are not affected by the drug; thus, they restart proliferating, determining this regenerative effect on the HCV29 spheroid. This hypothesis was confirmed by the HFS results, where after 72 hours, apart from the spheroids treated with the highest amounts of DTX, the viscoelastic parameters of the treated spheroids become like those of the 24 hours spheroids, closer to the values of the untreated cells. Analogously, the HT1376 spheroids were destroyed only at high concentrations of DTX, while at lower concentrations, they showed the recovery phenomena like the HCV29 spheroids. It was as well as confirmed by the HFS results. On the contrary, the mechanical results from T24 spheroids were difficult to be interpreted. From the live/dead images and the confocal images, it was clear that the drug had a significant effect on these spheroids, even at lower concentrations. And after continuous exposure to the drug, their condition became even worse. However, from the biophysical point of view, the viscoelastic parameters were overall randomly distributed, and a clear correlation between the drug treatment and changes in the mechanical properties of these cells was not found. Nevertheless, these experiments showed that the three spheroids, representing three different stages of bladder cancer, reacted uniquely to the treatment with the same drug.

It could be explained by the fact that their cytoskeletal structure is organized differently, HCV29 spheroids are the only ones to produce ECM, and HT1376 are the ones that lack thick actin bundles and express E-cadherin. Altogether, these elements could influence the drug action on the spheroids. Therefore, it can be concluded that multicellular spheroids are a good model for studying the effects of anticancer compounds on various types of bladder cancers. HFS could be a suitable tool to explore the mechanical signature of the spheroids upon drug treatment, and it may detect the effects of the drugs on cells before the biological effects induced by the drug become visible.

Part IV

Discussion and conclusions

Chapter 9

Discussions and conclusions

A living cell is a dynamic structure, changing in response to its functioning and various microenvironmental conditions. The viscoelastic nature of living cells derives from their internal structure, composed of both fluid and solid phases. The viscoelasticity of cells results from the water content (i.e., cell cytosol that contains the majority of fluid cellular constituents) interlaced with the polymerized solid structures (such as cell cytoskeleton). Therefore, as reported in numerous papers, the mechanical and rheological properties of cells are very complex and challenging to be fully understood [162] [163]. One of the main methods used to assess the mechanical properties of living cells at the single-cell level is the atomic force microscope (AFM). AFM has been widely used as a relevant method to distinguish cancerous cells by studying the correlation between the elastic modulus of cells and the process of cytoskeleton reorganization [126] [164]. It has been demonstrated that the mechanical properties of cells are mainly dependent on the actin cytoskeleton, which is known to behave like a viscoelastic material [165] [166]. Thus, both elastic and viscous components must be considered to obtain a complete description of cell mechanics.

The aim of the thesis was to evaluate the mechanical properties of spheroids formed from bladder cancer cells. The nanomechanical and rheological properties of bladder cancer cells deriving from different stages of tumor progression were compared. The chosen cell lines originated from early (non-malignant cell cancer of the ureter, HCV29 cells) and advanced (bladder carcinoma HT1376 cells and transitional cell carcinomaT24 cells) stages of cancer progression. A distinct actin cytoskeleton organization characterizes each chosen cell type, and, more importantly, nanomechanical properties at the single-cell level have already been known [111] [112] [114]. The results showed the highest Young's modulus value for non-malignant HCV29 cells and the lowest for cancerous cells (HT1376

and T24 cells). This makes them a suitable model for studying the mechanics of spheroids. The driving hypothesis assumes that single-cell mechanics translates into spheroid mechanics while preserving the relationship between non-malignant and cancerous cells, i.e., spheroids formed from non-malignant cells are stiffer than spheroids composed of cancer cells. Moreover, the mechanical resistance of spheroids is postulated to be maintained by actin filaments. Therefore, mechanical and microrheological properties were assessed to find the biophysical responses of bladder cancer spheroids to compressive and shear forces. The results were compared to already-known results obtained for bladder cancer cells.

9.1 Mechanical properties of bladder cancer cells

Bladder cancer cells have been extensively measured in AFM-based nanoindentation experiments, showing that the non-malignant cells are stiffer than the cancer cells [112] [114] [113]. Most of those measurements were conducted only at the single-cell level. Additionally, it has been demonstrated that the content of β-actin in cancer cell lines was 35 % and 42 % for HT1376 and T24 cells, correspondingly. The β-actin content was normalized to the β-actin in non-malignant HCV29 cells [112]. These previous results implied that the actin content decreases in the cancer cells, which can be responsible for higher cellular deformability (i.e., softening of cancer cells).

Although the bladder cancer cells have already been measured, there is always a need to remeasure them due to the large relativeness of Young's modulus. It has been discussed in various papers that AFM delivers the apparent Young's modulus value depending on the probing tip geometry and mechanical model applied [140] [141]. Moreover, the experimental conditions, such as the load speed, load force, number of force curves acquired during AFM measurements, and factors involved in data analysis, such as the contact point determination, have a big influence on the calculation of Young's modulus value [145].
Considering the relativeness of Young's modulus, the nanomechanical and rheological properties of bladder cells were conducted using a cantilever with a mounted pyramidal probe. The AFM measurements were performed as a function of culture conditions, i.e., single cells or monolayers. The results confirmed that cancer HT1376 and T24 cells are softer (more deformable) than non-malignant HCV29 cells. The studies were accompanied by fluorescent visualization of actin filaments (formed from the polymerized form of actin – F-actin). Inside cells, the actin cytoskeleton is composed of two main fractions: *(i)* a mesh created

from short filaments that, in fluorescent microscopy, are seen as a green shadow without specific structure, and *(ii)* a network of clearly visible long actin filaments, often bundled that could be attributed to stress fibers. Among the three studied bladder cell lines, only thick actin bundles in HCV29 and T24 cells were observed, while in HT1376 cells, only a mesh formed from short actin filaments was visible. The nanomechanical analysis performed via indentation shows that non-malignant cells are more rigid than cancerous cells, which agrees with already published results. Moreover, it was impossible to attribute the mechanical properties to the organization of actin filaments inside the cells, confirming that a 2D network of actin filaments cannot explain changes in the mechanical properties of bladder cancer cells. These results were obtained on single isolated cells that, although such measurements are widely accepted in the AFM community, not necessarily can be translated into more physiological conditions in which cells are interconnected. Therefore, further experiments were needed. This gap was filled by performing the AFM nanoindentation experiments on monolayers formed by all studied cell lines (monolayer was assumed to be more physiological state than single isolated cells). The results showed that actin filaments played an important role in maintaining the mechanical properties of cell monolayers. Only these cells (HCV29 and T24 cells), in which thick actin bundles were observed, became more rigid, while the mechanical properties of HT1376 cells remained similar to the properties of single cells. Therefore, the observed difference in cell mechanics could be associated with the presence and absence of thick actin bundles and with the presence of intercellular connections. Notwithstanding, Young's modulus for HCV29 cell monolayer was the highest, while its value for cancer cells was similar; thus, it was impossible to distinguish HT1376 cells from T24 cells. The non-malignant HCV29 cells remained stiffer than the two cancer cells regardless of the culture conditions making Young's modulus a potential tool to distinguish malignant and non-malignant bladder cancer cells.

9.2 Microrheological properties of bladder cancer cells

To find a better parameter describing the changes in the mechanics of bladder cancer cells, the works by Abidine et al. were taken into account. In two previous works, rheological properties of moderately differentiated RT112 bladder cancer cells and poorly differentiated transitional cell carcinoma T24 and J82, with a higher malignancy potential, were compared. The authors suggested that

changes in cell rheology may be a signature of cancer metastasis and correlate with different bladder cancer invasiveness [128] [129]. Because of how AFM probes, cell rheological properties are also related to the actin cytoskeleton. Typically, an indentation below 1 micron and an oscillation amplitude of 50 nm are applied [75]. Thus, in the next step, it was postulated that the rheological properties are related to the amount of monomeric G-actin (a non-polymerized form of actin), which could contribute to the viscous component of the cell. Although the correlation between cell mechanics (nanoindentation) and the expression of G-actin was not always evident when considering the mechanical properties of cells in monolayers, the largest deformability was observed for carcinoma HT1376 cells, for which the amount of G-actin was 2-3 larger than in the other two cell lines. Consequently, it could be assumed that the single cell and monolayer softening in regards to non-malignant HCV29 cells resulted from low actin content and large G-actin expression.
The results from microrheological experiments followed Young's modulus obtained from nanoindentation experiments. HCV29 and T24 cells become stiffer, presenting higher storage modulus values. An opposite behavior was observed for the HT1376 cells (storage modulus was lower). Considering that the shear storage modulus followed the same trend as Young's modulus, it was clear that thick actin bundles contributed to the mechanical resistance of cells undergoing shear stress. Young's and storage moduli describe only the elastic component of cells induced by deformation forces, which indicates that the non-malignant HCV29 cells are more resistant to compressive and shear forces than cancerous T24 and HT1376 cells. The viscoelastic component can be described by analyzing the loss modulus, which constituted c.a. 20 % to 50 % of the storage modulus, depending on the cell type and culture conditions (single cells or monolayers).

One can recall that storage and loss moduli depend on the frequency of oscillations. Their values increase with the increasing frequency following the single or double power-law functions [167]. To be independent of the frequency, two other parameters can describe the viscous component of living cells. There are loss factors, power law exponent, and/or transition frequency. In the presented thesis, both were evaluated, aiming at the ultimate goal of assessing which could be a better descriptor of the viscous component. The loss factor is the ratio between the loss and storage modulus. Among the studied bladder cell lines, HT1376 cells showed a considerably high loss factor value compared to the HCV29 and T24 cells. It indicates that this cell line has the largest viscous component compared to other studied cell lines, which is consistent with the absence of thick

actin bundles and a poorly differentiated actin cytoskeleton in this cell line. Regarding the transition frequency (frequency at which storage modulus equals loss modulus), the results showed the highest value for the non-malignant HCV29 cells, compared to T24 and HT1376 cells, regardless of the culture conditions. For HCV29 cells, transition frequency increases when moving from single cells to monolayers. An analogous but smaller increase was also observed for T24 cells. On the contrary, when the confluency altered, the HT1376 cell lines maintained their transition frequency value, thus their viscoelastic properties. These results could be explained by the cytoskeleton structure and composition differences. Similarly, the values of the power-law exponent confirmed the results described by the transition frequency. For instance, when there was a decrease in the transition frequency (HT1376 cells), there was an increase in the power-law exponent, confirming the fluid-like characteristic of that cell line.
To strengthen these results, microrheological measurements were conducted for cells treated with cytochalasin D, i.e., an agent inhibiting the formation of actin filaments. Upon preventing the polymerization of the actin filaments, a drop in the storage and loss moduli, and the transition frequency, was observed for all studied bladder cancer cells, indicating the increase in the viscous component. This is in good relation with previous work showing that cancer cells become more fluid-like after the treatment with compounds that disrupt the actin filaments [128] [166]. Simultaneously, the inhibition of actin filaments followed by changes in the rheological properties of cells demonstrates that thick actin bundles are responsible for maintaining the mechanical resistance of cells. Moreover, transition frequency was characteristic for each cell line, which indicates a potential to use it as a biomarker for classifying the cancer type.

9.3 Mechanical properties of multicellular spheroids

3D cell cultures, such as multicellular spheroids, can be applied to mimic the physiological environment of cells in solid tumors better than 2D cultures [48]. Only recently, the mechanical properties of spheroids became an interest of AFM studies due to their complex and multilayer structure [168] [169] [170]. Even fewer are the AFM mechanical studies performed on bladder cancer spheroids [129] [171] [172]. These studies were done on spheroids formed from transitional cell carcinoma T24 cells, in which the role of collagen in maintaining spheroid mechanics was assessed. In the thesis, a comparison of spheroids composed of the chosen panel of bladder cancer cells was performed. The spheroids formed from HT1376

cells have already been used in bladder cancer therapy [173] [174] [175], but such biomechanical and microrheological measurements were evaluated. Moreover, the goal was to compare these properties with reference, non-malignant HCV29 cells to verify how mechanics performed at the single, isolated cells translate to the mechanics of spheroids.

There are not many studies conducted on spheroids. Therefore, it was initially necessary to define the protocols to perform AFM experiments and understand the cytoskeleton-related changes. For this purpose, two cell lines were chosen as a basis for spheroid formation: *(i)* healthy lung fibroblast (NHLF), characterized by a well-differentiated actin cytoskeleton with thick and long actin bundles spanning over the cell body, and *(ii)* small-lung cancer cells (A549) with a poorly differentiated actin cytoskeleton and round morphology. The measurements were conducted using cantilevers of different geometry, i.e., cantilevers with mounted pyramidal and spherical tips and without tips (so-called tipless cantilevers). The results showed that the spheroids formed by NHLF cells have a higher value of Young's modulus than those formed by the cancerous A549 cells. The results were independent of the type of AFM probes. However, the magnitude of changes was related to the probing geometry. A most significant difference was observed for spherical probes and large indentation of 4-5 microns.

The probing geometry is defined by the contact area, which remains similar if the shape of the probing tip remains the same. Therefore, to be comparable with the measurements conducted on single cells and monolayers and simultaneously, to provide larger indentation depth, spheroids' mechanical and rheological properties were measured using cantilevers with mounted four-sided pyramids. The pyramids were characterized by an open angle of 40° as those used for measuring single, isolated cells and monolayers. The main difference was the length of the probing tip, which was c.a. 13 microns [125], which enabled large indentation depths.

The results of Young's modulus determination showed that 3-day spheroids formed from non-malignant cells are stiffer than spheroids composed of cancer cells, which correlates with the results obtained for single, isolated cells and monolayers. The storage modulus agrees with Young's modulus obtained from the indentation experiments. Its value is the largest for spheroids formed from non-malignant HCV29 cells and lower for spheroids made of cancer cells. It indicates the larger deformability of cancer spheroids during the indentation and when shear forces are applied. A similar tendency is observed for loss modulus, which describes how much energy is dissipated in the sample. HT1376 cells were characterized

by the highest loss factor, indicating that this cell line reveals the largest viscous component. It is again in a good relationship with the cytoskeletal organization (lack of stress fibers) and high G/F ratio (more monomeric G-actin).

9.4 Mechanical and microrheological properties of aging spheroids

Following the characterization of the mechanical and microrheological properties of spheroids after 3 days of culture, the aging process was investigated. Spheroids are known to have a growth similar to solid tumors, with an initial fast-growing phase followed by a plateau [44] [46] [50]. The spheroid growth was monitored by measuring the diameter as a function of culture day, obtaining a growth curve. By tracing the growth of bladder spheroids over two weeks, the growth curve showed that spheroids formed by both HCV29 and T24 cells grow like solid tumors do, while the spheroids formed by HT1376 cells were not. The latter required a small number of cells to form spheroids compared to HCV29 and T24 cells. To verify that the formed spherical structures are spheroids, the expression level of cadherins was evaluated. Cadherins are one of the key elements keeping cells together. E-cadherin is typical of non-invasive tumor cells. Loss of E-cadherin expression is observed during the transition to an invasive state due to the disruption of tight cell-cell contacts [158]. The Western blot results from the bladder cancer cell spheroids confirmed this hypothesis, showing that the HT1376 cell line is the only cell line expressing E-cadherin. There is a tighter cell-cell contact mechanism in the spheroids formed by HT1376 cells, which facilitates the spheroid formation and their growth over time. Both HCV29 and T24 cells express N-cadherin. Although HCV29 are non-malignant cell lines, and T24 are highly invasive cancer cells [176] [177], the difference between the two cell lines may reside in the binding stability of N-cadherin. The unbinding forces of N-cadherin complexes were studied using the AFM, and it was shown that the two cell lines exhibited different interaction forces of N-cadherin complexes, suggesting the malignant nature of T24 cells depended on it. It could partially also explain their pattern of spheroid formation, where T24 cells require a higher number of initial cells to form spheroids of a similar size as in the case when HCV29 cells were used.

Evaluation of changes induced by the aging effect was obtained by comparing the mechanical and rheological properties of spheroids collected after 3 days (mimicking the early stage of tumor progression) and after 14 days representing

the late stage of tumor progression. For the nanomechanical measurements, the AFM was applied, while for the macroscale level measurements, HFS was used. These results were then correlated to the internal structure of the spheroids analyzed from histological analysis and confocal imaging. Both techniques apply a compressive force to spheroids; however, AFM is a surface-based technique that can reach only small indentation depths. Thus, it can detect only the mechanical properties of a spheroid outer layer composed of proliferating cells [168] [170]. By increasing the radius of the pipette, HSF may deliver information on the viscoelastic properties of spheroids at the macroscale [178] [179]. HFS is a novel, less time-consuming micropipette aspiration technique that uses an interferometric optical readout to make real-time pressure and displacement measurements [130].

By probing the spheroids locally with the AFM, it was observed that, regardless of the days of culture, compared to the HCV29 spheroids, the cancer spheroids (formed from T24 and HT1376 cells) remained softer and much more deformable. Microrheological measurements were performed using AFM, and the results from the sinusoidal oscillation experiments confirmed that a more fluid-like behavior characterizes the cancer spheroids. In the case of aging spheroids, the HT1376 spheroids were characterized by the highest loss factor value and the lowest transition frequency value, confirming that these spheroids are the most viscous. Simultaneously, it was noticed that spheroids, regardless of the cell type used to form them, become more rigid when moving from 3 days to 14 days of culture. The increased stiffness could explain this due to the aging effect of the spheroids. It is very well known that the aging process affects the biomechanical properties of many cell types [180] [181] [182] [183]. It has been suggested that the age-associated mechanical changes are related either to the altered polymerization of the actin cytoskeleton [184] or to the density of cytoskeletal fibers [181]. To our knowledge, the alterations in the biomechanical properties of bladder cancer cells have not been reported to date. Thus, the results obtained in the current study cannot be compared to any previous data. However, based on the studies on other types of cells, the cytoskeletal organization of the three bladder spheroids was analyzed using confocal images. A clear effect of aging was visible in the spheroids formed by HCV29 cells: after 14-days of culture, the actin cytoskeleton was organized irregularly, compared to the 3-day spheroids, and there was significant evidence of apoptotic cells. The spheroids formed by HT1376 cells show actin fibers which are nicely organized in a shell-like manner, along the borders of the cells. After 14 days, it was possible to observe changes in the actin

cytoskeleton, which created some rounded structures here and there in between cells. It could be a mechanism found by the cells to escape from the inner area of the spheroids, where the nutrients and oxygens are lacking, as well as explaining their enlargement over time, unlike the other two types of spheroids. Meanwhile, there was no clear difference in the actin cytoskeleton between the 3- and 14-day spheroids formed by T24 cells.

Next, the elastic properties of the spheroids were determined at the macroscale using HFS. The results showed a significant decrease in the elastic modulus for the spheroids formed by HCV29 cells, a less significant decrease for those formed by HT1376 cells, and no significant differences between 3-days and 14-day T24 spheroids. The relevant result is that, in this case, the cancerous cells were more deformable than the non-malignant cell line.

The spheroid inner structures were analyzed using histological staining to understand further the different results obtained at the macroscale. From the analysis of spheroids formed by T24 cells, no considerable differences could be observed between 3-days and 14-days of spheroid culture, except for the number of cell nuclei which was higher in 3-day spheroids than in 14-day ones. It is in good relationship with the observation of the growth of these spheroids, i.e., the diameter became smaller with the culture time, which indicates that cells formed a stable structure. The same trend can be seen in the HCV29 spheroids. Unlike these two cell lines, the spheroids formed by HT1376 cells showed a higher density of cells in the outer layer of the 14-day spheroids, indicating a continuous proliferation and enlargement over time. In contrast to T24 spheroids, those formed by HCV29 and HT1376 cells showed some interesting features. The spheroids formed by HCV29 cells, after 14-days of culture, produced a high amount of ECM, composed mainly of collagen fibers. At the same time, the spheroids formed by HT1376 cells were the only ones to form a necrotic core after 14 days of culture. These results could explain the softening observed by HFS, confirming that the cell-cell and cell-ECM interactions play a key role in the mechanical properties of the spheroids. During cancer progression, alterations in cell-cell adhesion and cell-ECM interactions are known to stimulate cytoskeleton remodeling, which induces the mechanotransduction of cancer cells to activate signaling pathways, allowing them to fulfill their survival needs [38].

Last but not least, to understand how the lack of actin cytoskeleton reorganization in the T24 spheroids is linked with mechanical properties, AFM indentation measurements were performed on the spheroid cross-sections. The spheroids were cut into 20 μm thick sections, and elasticity measurements were conducted on sec-

tions from the 3-day and 14-day spheroids. The obtained results confirmed the stiffening of these cells after 14 days of culture. Moreover, from the confocal images of the cross sections, it was possible to see a different cytoskeletal organization in 3-days and 14-day spheroids. Surprisingly, the 14-day spheroid section showed a more organized and uniform structure than the 3-day spheroids. However, it was difficult to make proper correlations between the actin cytoskeleton and the mechanical results because of the possible discrepancies introduced during the cryosection of spheroids. The main advantage of using the spheroid sections was that it allowed the mechanical analysis of the different layers constituting the spheroid: proliferating (outer) area, quiescent (inner) area, and core. Thus, it was verified whether cells in the different areas exhibited different mechanical properties. It was interesting to notice how cells increased their stiffness when moving from the inside of the spheroid to the outer layer, demonstrating that cells that are in proliferation and highly metabolically active are stiffer than the cells with an inactive metabolism and in a senescent state.

9.5 Effects of DTX on mechanical properties of bladder spheroids

The major application of the MCSs is in the field of anticancer drug development because, unlike the traditional 2D cultures, MCSs can better mimic the 3D structure of a tumor mass and also the microenvironment to which cancer cell are exposed to [185]. The results show how spheroid mechanical and microrheological properties change while mimicking solid tumor growth. It was possible to conclude that spheroids' mechanical and microrheological properties can be used as a good biomarker to identify stages of tumor progression. Thus, multicellular spheroids are shown to be a good in vitro model for bladder cancers, which could be applied to the investigations on the effects of anticancer compounds. The rheological properties of bladder cancer spheroids were measured to demonstrate such applicability. Only HSF was used because of its macroscale character. For this purpose, docetaxel (DTX), a microtubule-stabilizing compound, was chosen to treat the spheroids. The effects of docetaxel on bladder cancer cells were previously shown in HT1376 and T24 cells cultured as monolayers [160]. The IC50 for HT1376 and T24 cells treated with DTX was 4.18 nM and 3.78 nM, respectively. Another study on HT1376 cells treated with DTX revealed the apoptotic events induced by the microtubule-interfering agent [161]. It showed that DTX had an antiproliferative effect on HT1376 cells starting from the concentration of 37 nM,

both after continuous exposure of 24 hours to the drug and a 1-hour treatment followed by a 23-hour wash-out. To see the necrosis effects, they used 3.7 μM, which is the concentration of DTX used in in vivo treatment of patients [186]. Using a flow cytometry gave information on the order of the apoptotic events in HT1376 cells upon DTX treatment, and the order was: 1) cell cycle arrest; 2) loss of mitochondrial membrane potential; 3) cell shrinkage and decrease in granularity; 4), DNA fragmentation 6) loss of membrane integrity and 7) further DNA fragmentation [161]. However, the limitation of this method is that it does not consider the fact that not all cells die simultaneously after drug treatment, as death is dependent on factors such as the cell cycle status and the individual energy level of a cell. Therefore, in 2D cultures, there is a population of asynchronously growing cells, cycling cells, cycle-arrested cells, and cells undergoing apoptosis, implying that it is not easy to detect the effects of a drug on cell culture. When it comes to the 3D models, there is an interesting study on spheroids formed by HeLa (human cervical) and HT29 (colon) cancer cells [187]. The authors have demonstrated that cells cultured as spheroids are more resistant to the drug treatment than those cultured as monolayers. The poor penetration of DTX explained it in the spheroids [188].

Few studies showed the mechanical behaviors of cells upon treatment with anticancer drugs, and they all showed stiffening of cells as a response to the drug treatment [189]. In the current work, the effects of an anticancer drug on the mechanical properties of bladder cancer cells, not in 2D, but 3D models, were investigated. To obtain the collective response from cells, instead of AFM, HFS was used. Spheroids formed by HCV29, HT2376, and T24 cells were treated with both low (1-20 nM) and high (250-1000 nM) concentrations of DTX. The effects of the drug were tested after 24 hours and 72 hours of treatment by analyzing *(1)* the size of the spheroids (by simply visualizing them on an optical microscope); *(2)* the amount of live/dead cells (fluorescent microscope); *(3)* cytoskeleton rearrangement (confocal images); *(4)* viscoelastic properties of cells (time domain viscoelasticity by HFS).

In all cell lines, after 24 hours of treatment, a visible decrease in the spheroid diameter was observed only at high concentrations of DTX. After 72 hours of treatment, the HCV29 spheroids became smaller only at 1 μM concentration of the drug, while T24 spheroids became smaller in size at both high and low concentrations. Similarly, the HT1376 spheroids showed a reduced diameter at high concentrations of DTX. From the live/dead images, it was clear that the number of dead cells increased in all cell lines after 72 hours of treatment, except for

HCV29 spheroids, which roughly showed the same amount at the two-time points. Unlike HCV29 spheroids, those formed by HT1376 and T24 cell lines presented a completely disrupted structure of the spheroids at high concentrations of DTX. Afterward, the viscoelastic properties of the treated and untreated cells were obtained by HFS, and they were described using two interdependent parameters: fluidity index and fractional compliance. The results from HFS were peculiar for each type of spheroids. Starting with HCV29 spheroids, when comparing the results from 24-hour and 72-hour treatments, the fluidity index decreased at all DTX concentrations, indicating a modification towards a solid-like behavior. Interestingly, when plotting the fluidity index versus the fractional compliance, after 72 hours, there was an overall shift of the treated samples towards the values of the 24 hours untreated sample, meaning that their viscoelasticity became similar to the untreated spheroids. It could be a sign of recovery effect, and it is in good terms with the live/dead images and the confocal images, where, apart from the HCV29 spheroids treated with 1 μM DTX, there were no significant differences between the treated spheroids after 24 hours and 72 hours. It could be explained by the fact that HCV29 spheroids produce ECM. It is very well known that the cell-ECM interactions create a barrier that prevents the penetration and distribution of anticancer drugs in the tumor mass [190] [191]. Thus, it may be the reason why in the HCV29 spheroids, there were no important differences between the control and the treated samples, and a very high concentration of DTX was necessary to see some relevant visible changes. Despite this, the HFS could detect the viscoelastic changes induced by the drug even at smaller concentrations, thus, providing information about drug action a priori to biological assays.

Looking at the results for the T24 spheroids, there were no consistent relationships between the viscoelastic parameters and the DTX concentrations, and no clear trend was present between spheroids treated for 24 hours and 72 hours. T24 cells are characterized by a doubling time of 21 hours [192]. It is possible that the T24 spheroids were composed of asynchronously growing cells, cycle-arrested cells, and cells undergoing apoptosis, making it difficult to detect the effects of DTX on the whole structure.

Next, the spheroids formed by HT1376 cells at lower concentrations of DTX showed a similar fluidity index and fractional compliance after 24 and 72-hour treatments. At high concentrations, as indicated in the live/dead and confocal images, the whole structure of the spheroid is compromised. Interestingly, after 72 hours, when plotting fractional compliance versus fluidity index, the lower concentration values shift towards the value of the untreated sample, implying a clear

recovery phenomenon. This result is supported by the diameter increase of the HT1376 spheroids after 72 hours of treatment with low concentrations of DTX (the doubling time of HT1376 is 31 hours [192]). The HFS measurements provided sufficient information to distinguish between the various spheroids treated with DTX based on their dynamic changes. The observed changes in the mechanical properties may be caused by DTX that leads to microtubule remodeling and membrane protein aggregation, which affects cell microstructure and increases cell strength.

9.6 Conclusions

From all these results, we can conclude that the multicellular spheroids can be used as a good *in vitro* model to represent different stages of bladder cancers, and, assuming that under compression and shear stress cancer cells are characterized by a larger deformability, the single-cell mechanics can be translated into spheroids mechanics, i.e., spheroids formed from non-malignant cells are stiffer than spheroids composed of cancer cells. Our findings show that the remodelling of actin filaments is mainly responsible fot the softening and fluidization of bladder cancer spheroids. In addition, we confirm that also the cell-cell and cell-ECM interactions play an important role in the mechanical properties of spheroids.
To sum up, the measurements of mechanical/rheological properties of spheroids may be used as a method to not only distinguish malignant and non-malignant bladder cancers, but also to detect cellular response to antitumor drugs action before the appearance of biological markers induced by the drug. Therefore, by assessing changes in the physical parameters of spheroids, it would be possible to predict whether particular cells will be more or less resistant to chemotherapeutic agents. In this way, the results from the current study provide a new biomechanical marker and a new tool to evaluate drug activity in tumor models, which may be used in expanded therapy in the future.

Appendix

Appendix A

AFM measurements of T24 spheroids section

So far, all the mechanical measurements have been done on spheroids as a whole. Therefore, it was possible to investigate the outer layer of the cells with a maximum indentation of 8 μm for AFM and an area of 50 μm^2 for the HFS. In any case, we obtained the signal only from the cells in the proliferating area. Knowing that the spheroids have a unique structure, where the cells inside are in a quiescent mode and less metabolically active, to explore the mechanical signals from the different area of the spheroids AFM measurements were performed on spheroid sections. In particular, to understand how the lack of actin cytoskeleton reorganization in the T24 spheroids is linked with mechanical properties, these spheroids were chosen for this type of measurement.
The spheroids formed by T24 cells were cut into sections thick 20 μm (details are in section 3.8) and used for the AFM measurements. In figure A.1 the results for the spheroids section from T24 spheroids, 3 days and 14 days, are shown.
The AFM measurements were performed with the pyramidal tip NSC36-C keeping the indentation lower than 2 μm. Even though only two sections were measured for each time point, from each section 4 maps were measured for each area. The preliminary results in figure A.1 confirm the results that were found out for this cell line from the other measurements. When comparing the results for the outer layers, there is a clear increase of Young's modulus in the spheroids over 14 days, from 2,4 kPa to 8,9 kPa.
Interestingly, the difference between the several areas of the spheroids is visible only in those cultured for 14 days. This is in relation to the fact that, at 3 days, the cells are still in the exponential growth phase and, they have not adequately reached the expected struture. On the other hand, after 14 days, even though

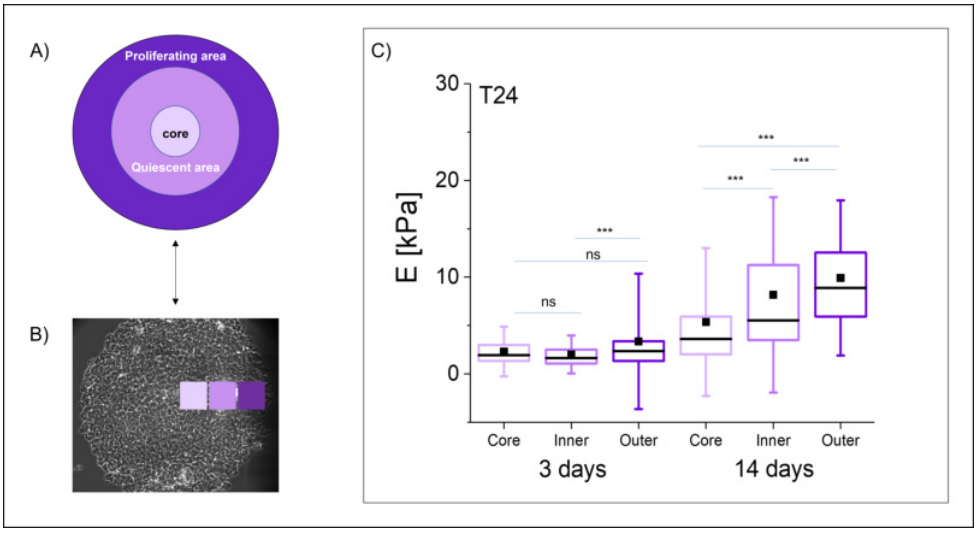

Figure A.1: **Elastic properties of T24 3-days and 14-days spheroid sections.** Box plots showing Young's modulus variability for T24 spheroids cultured for 3 days and 14 days. The black dots and lines are the mean and median, respectively; box denotes standard deviation; error bars represent 10 % and 90 % percentile. (*** $p < 0.001$, ns – not statistically significant). On the right, there is the scheme of the spheroid structure and how the measurements were performed on the section of T24. Two spheroid sections per day and 4 maps (30x30 μm^2)per each area were measured.

there is not present a necrotic core inside the spheroid. In the inner layer, there are cells that are not actively proliferating. Thus, from these preliminary results, it can be confirmed that the proliferating cells in the outer layer are stiffer than than cells less active, and that there is a progress softening when moving from the outside to the inside of the spheroids.

A.0.1 Confocal images of T24 spheroids section

To further analyze the inner structure of the spheroids, confocal images of the T24 sections were taken (figure A.2).
The sections used for the AFM measurements were then fixed and prepared for the staining of the nucleus, the actin filaments and the microtubules. The 3 days section is full of nuclei with different sizes, actin and microtubules organized, indicating different stages of proliferation. On the contrary, the 14 days section shows a more uniform structure, a low amount of actin filaments, and the absence of the microtubules in the inner area.

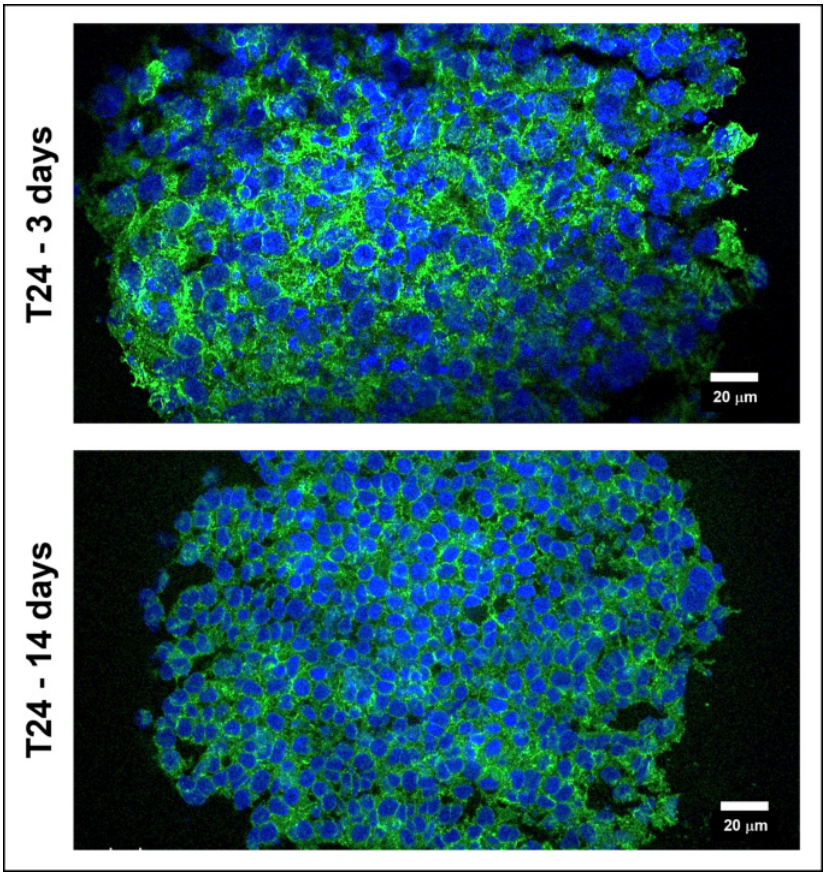

Figure A.2: **Confocal images of T24 spheroids sections, at 3 days and 14 days of culture.** Blue: nucleus - Green: actin filaments - Red: microtubules.

A.0.2 Summary

The AFM measurements were performed in sections of spheroids obtained from T24 and cultured for 3 and 14 days. The main aim was to elaborate on how the mechanical properties change in the outer layer and inner layers of the spheroid. Interestingly, the outer layer of the 14-day spheroids was significantly stiffer than the corresponding layer of the 3-day spheroids, confirming the stiffening of the aging spheroids demonstrated by the measurements on whole spheroids. A gradual stiffening of the cells was observed when moving from the inner layer to the outer layer, indicating that the cells that are metabolically active and highly active in proliferation are stiffer than the inactive and quiescent cells.

Appendix B

MTS results for spheroids treated with DTX

The determination of the EC50 was possible to obtain only for spheroids formed by HCV29 cells after 72 hours of treatment with DTX. The obtained data for the various concentrations were fitted with a dose-response function (figure B.1).

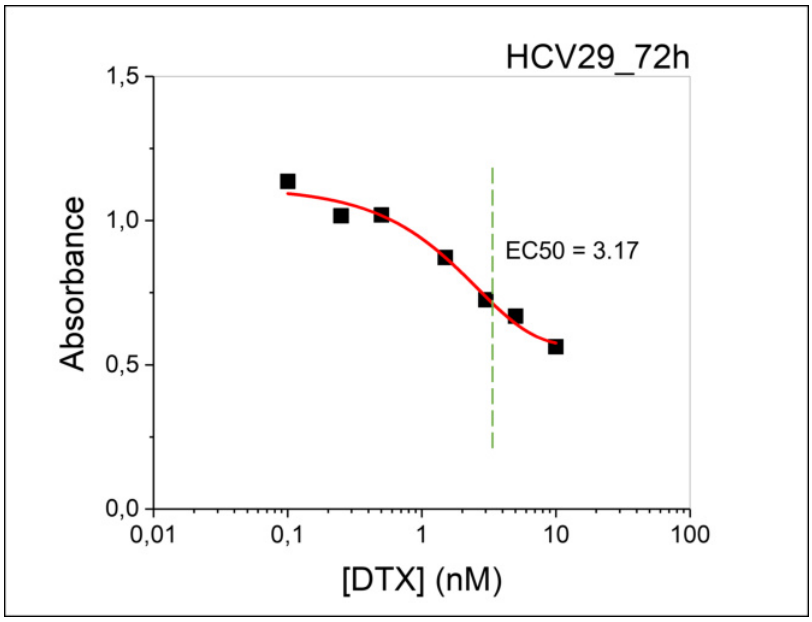

Figure B.1: **MTS assay applied to determine the cytotoxicity level in bladder cancer spheroids formed by HCV29 cells treated with DTX.** Each point corresponds to mean ± standard deviation (n = 2 repetitions). Data are fitted to a dose-response function, and EC50 was determined.

The fitted EC50 value determined for HCV29 cells was 3.1 nM. However, be-

cause the MTS test was unsuccessful in all cases due to their difficult application in multilayer samples like spheroids, there was no assurance that the obtained EC50 corresponded to the real value for HCV29 cells. Thus, the MTS test was not used to determine the cytotoxicity of bladder cancer spheroids.

The remaining results from MTS are shown in figure B.2.

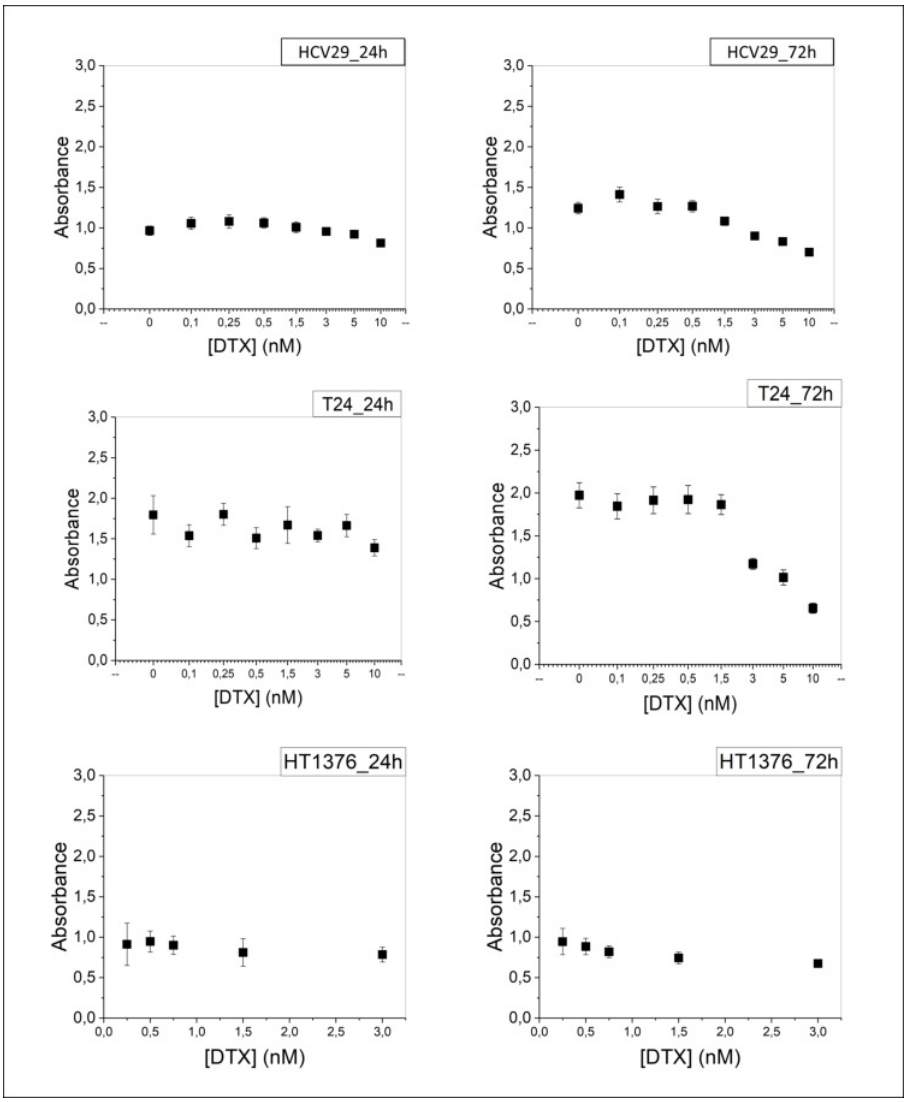

Figure B.2: **MTS assay applied to determine the cytotoxicity level in bladder cancer spheroids treated with DTX.** Each point corresponds to mean ± standard deviation (n = 2 repetitions).

Bibliography

[1] World Health Organization - Global Cancer Observatory.

[2] A. Richters, KKH Aben, LALM Kiemeney, *The global burden of urinary bladder cancer: an update*, World Journal of Urology, **38**, 1895-1904 (2020).

[3] F.H. van Osch, S.H. Jochems, F.J. van Schooten, R.T. Bryan, M.P. Zeegers, *Quantified relations between exposure to tobacco smoking and bladder cancer risk: a metaanalysis of 89 observational studies*, International Journal of Epidemiology, **45**, 857-70 (2016).

[4] J. Mushtaq, R. Thurairaja, R. Nair, *Bladder Cancer*, Surgery, **37**, 529-537 (2019).

[5] K. Saginala, A. Barsouk, J. Aluru, P. Rawla, S. Padala, A. Barsouk, *Epidemiology of bladder Cancer*, Medical Sciences, **8**, 1-12 (2020).

[6] S.P. Jost, J.A. Gosling, J.S. Dixon, *The morphology of normal human bladder urothelium*, Jpurnal of Anatomy, **167**, 103-115 (1989)

[7] P. Khandelwal, S. N. Abraham, G. Apodaca, *Cell biology and physiology of the uroepithelium*, The American Journal of Physiology - Renal Physiology, **297**, F1477-501 (2009).

[8] O. Sanli, J. Dobruch, M.A. Knowles, M. Burger, M. Alemozaffar, M.E. Nielsen, Y. Lotan, *Bladder cancer*, Nature Reviews Disease Primers, **3**, 17022 (2017).

[9] J. Quarles, J. Richmond, V. Swamy, J. Pandey, *Educational Case: Bladder Urothelial Cell Carcinoma TNM Stage, Prognosis and Management*, Academic pathology, **29**, (2021).

[10] M. Lekka, P. Laidler, D. Gil, J. Lekki, Z. Stachura, A.Z. Hrynkiewicz, *Elasticity of normal and cancerous human bladder cells studied by scanning force microscopy*, European Biophysical Journal, **28**, 312-316 (1999)

[11] C. Bernardo, C. Costa, C. Palmeira, R. Pinto-Leite, P. Oliveira, R. Freitas, F. Amado, L.L. Santos, *What we have learned from urinary bladder cancer models*, Journal of Cancer Metastasis and Treatment, **2**, 51-58 (2016)

[12] M. Schmidt-Hansen, S. Berendse, W. Hamilton, *The association between symptoms and bladder or renal tract cancer in priamry care: a systematic review*, British Journal of General Practice, **65**, 769-775 (2015).

[13] L.H.C. Kim, M.I. Patel, *Transurethral resection of bladder tumour (TURBT)*, Transitional Andrology and Urology, **9**, 3056-3072 (2020).

[14] Z. Shen, T. Shen, M.G. Wientjes, M.A. O'Donnell, J.L. Au, *Intravesical treatments of bladder cancer: review*, Pharmaceutical Research, **25** (7), 1500-1510 (2008).

[15] A. Bohle, P.R. Bock, *Intravesical bacille Calmette-Guerin versus mitomycin C in superficial bladder cancer: formal meta-analysis of comparative studies on tumor progression*, Urology, **63** (4), 682-686 (2004).

[16] R., S.S. Selph, D.I. Buckley, K.S. Gustafson, J.C. Griffin, S.E. Grusing, J.L. Gore, *Treatment of muscle-invasive bladder cancer: A systematic review*, Cancer, **122** (6), 842-851 (2016).

[17] M. Manoharan, *Intravescical therapy for urothelial carcinoma of the bladder*, Indian Journal of Urology, **27** (2), 252-261 (2011).

[18] S.A. Hussain, D.H. Palmer, B. Lloyd, S.I. Collins, D. Barton, J. Ansari, N.D. James, *A study of split-dose cisplatin-based neo-adjuvant chemotherapy in muscle-invasive bladder cancer*, Oncology Letters, **3** (4), 855-859 (2012).

[19] H. von der Masse, *Gemcitabine and cisplatin in locally advanced and/or metastatic bladder cancer*, European Journal of Cancer, **36** Suppl 2, 13-6 (2000).

[20] S. Dasari, P.B. Tchounwou, *Cisplatin in cancer therapy: molecular mechanisms of action*, European Journal of Pharmacology, **0**, 364-378 (2014).

[21] B. Alberts, K. Hopkin, A. Johnson, D. Morgan, M. Raff, K. Roberts, P. Walter, *Essential Cell Biology* (2009).

[22] S.J. Singer, G.L. Nicolson, *The Fluid Mosaic Model of the Structure of Cell Membranes*, Science, **175**, 720-731 (1972).

[23] Y. Wang, Y.Z. Ohkubo, E. Tajkhorshid, *Gas Conduction of Lipid Bilayers and Membrane Channels*, Current Topics in Membrane, **60**, 343-367 (2008).

[24] W.R. Loewenstein, M. Nakas, S.J. Socolar, *Junstional Membrane Uncoupling: Permeability transformations at a cell membrane junstion*, Journal of General Physiology, **50**, 1865-1891 (1967).

[25] F.B. Straub, *Purification of malic acid dehydrase and the significance of cell structure in dehydrogenation*, Hoppe-Seylers Zeitschrift Fur Physiologische Chemie, **275**, 63-72 (1942).

[26] T. Svitkina, *The actin cytoskeleton and actin-based motility*, Cold Spring Harbor Perspectives in Biology, **10**, (2018).

[27] M.W. Kirschner, *Implications of Treadmilling for the Stability and Polarity of Actin and Tubulin polymers In Vivo*, Journal of Cell Biology, **86**, 330-334 (1980).

[28] H. Herrmann, H. Bar, L. Kreplak, S.V. Strelkov, U. Aebi *Intermediate filaments: from cell architecture to nanomechanics*, Nature Reviews Molecular Cell Biology, **8**, 562-573 (2007).

[29] T. Hohmann, F. Dehghani, *The Cytoskeleton-A Complex Interacting Meshwork*, Cells, **8**, 362 (2019).

[30] C. Kiani, L. Chen, Y.J. Wu, A.J. Yee, B.B. Yang, *Structure and function of aggrecan*, Cell Research, **12**, 19-32 (2002)

[31] M.A. Garcia, W.J. Nelson, N. Chavez, *Cell-Cell Junctions Organize Structural and Signaling Networks*, Cold Spring Harbor Perspectives in Biology,**10**, (2018).

[32] C. Zihni, C. Mills, K. Matter, M.S. Balda, *Tight junctions: from simple barriers to multifunctional molecular gates*, Nature Reviews Molecular Cell Biology, **17**, 564-580 (2016).

[33] W.H. Evans, P.E.M. Martin, *Gap junctions: structure and function (Review)*, Molecular Membrane Biology, **19**, 121-136 (2002).

[34] M.S. Adil, S.P. Narayanan, P.R. Somanath, *Cell-cell junctions: structure and regulation in physiology and pathology*, Tissue Barriers, **9** (2021).

[35] M. Takeichi, *Cadherins: a molecular family important in selective cell-cell adhesion*, Annual Review of Biochemistry, 237-252 (1990).

[36] L. Kornberg, H.S. Earp, J.T. Parsons, M. schaller, R. L. Juliano, *Cell adhesion or integrin clustering increases phosphorylation of a focal adhesion-associated tyrosine kinase*, Journal of Biological Chemistry, **267**, 23439-23442 (1992).

[37] J.G. Lock, B. Wehrle-Haller, S. Strömblad, *Cell-matrix adhesion complexes: master control machinery of cell migration*, Seminars in Cancer Biology, **18**, 65-76 (2007).

[38] D. Hanahan, R.A. Weinberg, *Hallmarks of cancer: the next generation*, Cell, **144**, 646-674 (2011).

[39] M.R. Junttila, F.J. de Sauvage, *Influence of tumour micro-environment heterogeneity on therapeutic response*, Nature, **501**, 346-354 (2013).

[40] M.I. Khot, M.A. Levenstein, N. Kapur, D.G. Jayne, *A Review on the Recent Advancement in "Tumour Spehroids-on-a-Chip"*, Journal of Cancer REsearch and Practice, **x**, xxx (2019).

[41] F. Pampaloni, E.G. Reynaud, E.H. Stelzer, *The third dimension bridges the gap between cell culture and live tissue*, Nature Reviews Molecular Cell Biology, **10**, 839-845 (2007).

[42] R.M. Sutherland, J.A. McCredie, W.R. Inch, *Growth of multicell spheroids in tissue culture as a model of nodular carcinomas*, Journal of the National Cancer Institute, **46**, 113-120 (1971).

[43] C.R. Thoma, M. Zimmermann, I. Agarkova, J.M. Kelm, W. Krek, *3D cell culture systems modeling tumor growth determinants in cancer target discovery*, Advanced Drug Delivery Reviews, **69-70**, 29-41 (2014).

[44] E.C. Costa, A.F: Moreira, D. de Melo-Diogo, V.M. Gaspar, M.P. Carvalho, I.J. Correia, *3D tumor spheroids: an overview on the tools and techniques used for their analysis*, Biotechnology Advances, **34**, 1427-1441 (2016).

[45] R.Z. Lin, H.Y. Chang, *Recent advances in three-dimensional multicellular spheroid culture for biomedical research*, Biotechnology Journal, **3**, 1172-1184 (2008).

[46] G. Lazzari, P. Couvreur, S. Mura, *Multicellular tumor spheroids: a relevant 3D model for in vitro preclinical investigation of polymer nanomedicines*, Polymer Chemistry, RoyalSociety of Chemistry, **8** (34), 4947-4969 (2017).

[47] R.Z. Lin, L.F. Chou, C.C.M. Chien, H.Y. Chang, *Dynamic analysis of hepatoma spheroid formation: roles of E-cadherin and β1-integrin*, Cell and Tissue Research, **324**, 411-422 (2006).

[48] L.B. Weiswald, D. Bellet, V. Dangles-Marie, *Spherical Cancer Models in Tumor Biology*, Neoplasia, **17** (2015).

[49] L. Alhasan, A. Qi, A. Al-Abboodi, A. Rezk, P.P.Y. Chan, C. Iliescu, L.Y. Yeo, *Rapid enhancement of cellular spheroid assembly by acoustically driven microcentrifugation*, ACS Biomaterials Science and Engineering, **2**, 1013-1022 (2016).

[50] J.P. Ward, J. King, *Mathematical modelling of avascular-tumour growth*, Mathematical Medicine and Biology: a journal of the IMA, **14**, 39-69 (1997).

[51] X. Cui, Y. Hartanto, H. Zhang, *Advances in multicellular spheroids formation*, Journal of the Royal Society Interface, **14**, 20160877 (2017).

[52] J.M. Yuhas, A.P. Li, A.O. Martinez, A.J. Ladman, *A simplified method for production and growth of multicellular tumor spheroids*, Cancer Research, **37**, 3639-3643 (1977).

[53] J. Landra, D. Bernier, C. Ouellet, R. Goyette, N. Marceau, *Spheroidal aggregate culture of rat liver cells: histotypic reorganization, biomatrix deposition, and maintenance of functional activities*, Journal of Cell Biology, **101**, 914-923 (1985).

[54] G.A. Hamilton, C. Westmorel, A.E. George, *Effects of medium composition on the morphology and function of rat hepatocytes cultured as spheroids and monolayers*, In Vitro Cellular and Developmental Biology- Animal, **37**, 656-667 (2001).

[55] T.D. Butcher, T. Alliston, V.M. Weaver,*A tense situation: forcing tumour progression*, Nature Reviews Cancer, **9**, 108-122 (2009)

[56] A. Hall, *The cytoskeleton and cancer*, Cancer Metastasis Review, **28**, 5-14 (2009).

[57] E.Y.H.P. Lee, *Tumor-Suppressor Genes and Their alterations in Breast-Cancer*, Seminars in Cancer Biology, **6**, 119-125 (1995).

[58] M.A. Jordan, L. Wilson, *Microtubules and actin filaments: Dynamic targets for cancer chemotherapy*, Current Opinion in Cell Biology, **10** 123-130 (1998).

[59] M. Makale, *Cellular mechanobiology and cancer metastasis*, Birth Defects Research Part C: Embryo Today: Reviews, **81**, 329-343 (2007).

[60] Z.M. Shao, M. Nguyen, S. Barsky, *Human breast carcinoma desmoplasia is PDGF initiated*, Oncogene, **19**, 4337-4345 (2000).

[61] G. Helmlinger, P.A. Netti, H.C. Lichtenbeld, R.J. Melder, R.K. Jain, *Solid stress inhibits the growth of multicellular tumor spheroids*, Nature Biotechnology, **15**, 778-783 (1997).

[62] Y. Boucher, R.K. Jain, *Microvascular pressure is the principal driving force for interstitial hypertension in solid tumors - implications for vascular collapse*, Cancer Research, **52**, 5110-5114 (1992).

[63] M.D. Basson, C.F. Yu, O. Herden-Kirchoff, M. Ellermeier, M.A. Sanders, R.C. Merrell, B.E. Sumpio, *Effects of increased ambient pressure on colon cancer cell adhesion*, Journal of Cellular Biochemistry, **78**, 47-61 (2000).

[64] S.E. Cross, Y.S. Jin, J. Tondre, R. Wong, J. Rao, J.K. Gimzewski, *AFM-based analysis of human metastatic cancer cells*, Nanotechnology, **2**, 780-783 (2008).

[65] S.M. Kakkad, M. Solaiyappan, B. O'Rourke, I. Stasinopoulos, E. Ackerstaff, V. Raman, Z.M. Bhujwalla, K. Glunde, *Hypoxic tumor microenvironments reduce collagen I fiber density*, Neoplasia, **12**, 608-617 (2010).

[66] D. Fletcher, R. Mullins, *Cell mechanics and the cytoskeleton*, Nature, **463**, 485-492 (2010).

[67] S. Suresh, *Biomechanics and biophysics of cancer cells*, Acta Biomaterialia, **3**, 413-438 (2007).

[68] S. Suresh, J. Spatz, J.P. Mills, A. Micoulet, M. Dao, C.T. Lim, M. Beil, t. Seufferlein, *Connections between single cell biomechanics and human disease states: gastrointestinal cancer and malaria*, Acta Biomaterialia, **1**, 15-30 (2005).

[69] E. Moeendarbary, A. R. Harris, *Cell mechanics: Principles, practices, and prospects*, Wiley Interdisciplinary Reviews: Systems Biology and Medicine, **6**, 371-388 (2014).

[70] L. Wolff, P. Fernandez, K. Kroy, *Inelastic mechanics of sticky biopolymer networks*, New journal of Physics, **12**, (2010).

[71] C. Vertier, J. Etienne, A. Duperray, L. Preziosi, *Review: Rheological properties of biological materials*, Comptes Rendus Physique, **10**, 790-811 (2009).

[72] A.A. Alsayed, *Physics of Open Fractures: Reconsidering Tissue Viability, Contamination Risk and Importance of Wound Debridement*, Journal of Applied Mathematics and Physics, **9**, 176-182 (2021).

[73] Z.H. Stachurski, *Mechanical behavior of materials*, (2009)

[74] M.F: Ashby, *Physical modelling of materials problems*, Material Science and Technology, **8**, 102-111 (1992).

[75] J. Alcaraz, L. Buscemi, M. Grabulosa, X. Trepat, B. Fabry, R. Farre, D. Navajas, *Microrheology of human lung epithelial cells measured by atomic force microscopy*, Biophysical Journal, **84** (2003).

[76] G. Bilodeau, *Regular pyramid punch problem*, Journal of Applied Mechanics, **59**, 519-523 (1992).

[77] R.E. Mahaffy, C.K. Shih, F.C. MacKintosh, J. Kas, *Scanning probe-based frequency-dependent microrheology of polymer gels and biological cells*, Physics Review Letters, **85**, 880-883 (2000).

[78] M. Radmacher, M. Fritz, C.M. Kacher, J.P. Cleveland, P.K. Hansma, *Measuring the viscoelastic properties of human platelets with the atomic force microscopy*, Biophysical Journal, **70**, 556-567 (1996).

[79] D.T.N. Chen, Q. Wen, P.A. Janmey, J.C. Crocker, A.G. Yodh, *Rheology of soft materials*, Annual review of condensed matter physics, **1**, 301-322 (2010).

[80] T. Osswald, N. Rudolph, *Polymer Rheology*, Carl Hanser Verlag GmbH and Co. KG, 1-24 (2014).

[81] K. Joyner, S. Yang, G.A. Duncan, *Microrheology for biomaterial design*, APL Bioengineering, **4**, (2020).

[82] H.A. Barnes, J.F. Hutton, K. Walters, *An introduction to rheology*, Elsevier, **3** (1989).

[83] J.M. Dealy, K.F. Wissbrun,*Introduction to rheology. In Melt Rheology and Its Role in Plastics Processing*, Springer, Dordrecht, 1-41 (1999)

[84] W.N. Findley, J.S. Lai, K. Onaran, *Creep and Relaxation of Nonlinear Viscoelastic Materials*, North-Holland Publ. Comp., Oxford (1976).

[85] P.J. Cullen, C.P. O'Donnell, M. Houska, *Rotational rheometry using complex geometries - a review*, Journal of Texture Studies, **34**, 1-20 (2003).

[86] Malvern Instruments White Paper, *A basic introduction to rheology*, (2016).

[87] J. Lemaitre, *Introduction to elasticity and viscoelastcity*, Handbook of Materials Behavior Models, Academic Press, 71-74 (2001)

[88] C.T. Lim, E. H. Zhou, S. T. Quek, *Mechancial models for living cells - A review*, J. Biomech., **39**, 195-216 (2006).

[89] G. Du, A. Ravetto, Q. Fang, J.M.J. den Toonder, *Cell types can be distinguished by measuring their viscoelastic recovery times using a micro-fluidic device*, Biomedical Microdevices, **13**, 29-40 (2011).

[90] M.N. Starodubtseva, *Mechanical properties of cells and ageing*, Ageing Research Review, **10**, 16-25 (2011).

[91] M.A. Tsai, D.A. Hammer, *Rheology of rat basophilic leukemia cells*, Annals of Biomedical Engineering, **25**, 62-68 (1997).

[92] G.T. Charras, J.C. Yarrow, M.A. Horton, L. Mahadevan, T.J. Mitchison, *Non-equilibration of hydrostatic pressure in blebbing cells*, Nature, **435**, 365-369 (2005).

[93] G.T. Charras, T.J. Mitchison, L. Mahadevan, *Animal cell hydraulics*, Journal of Cell Science, **122**, 3233-3241 (2009).

[94] D.E. Ingber, *Tensegrity: The architectural basis of cellular mechanotransduction*, Annual Review of Physiology, **59**, 575-599 (1997).

[95] S. Chien, L.A. Sung, M.M. Lee, R. Skalak, *Red cell membrane elasticity as determined by flow channel technique*, Biorheology, **29**, 467-478 (1992).

[96] A. Pena, M.D. Bolton, J.D. Pickard, *Cellular poroelasticity: A theoretical model for soft tissue mechanics*, Poromechanics, 475-480 (1998).

[97] P.L. Chandran, V.H. Barocas, *Microstructural mechanics of collagen gels in confined compression: Poroelasticity, viscoelasticity and collapse*, Journal of Biomechanical Engineering-Transactions of the Asme, **126**, 152-166 (2004).

[98] M.A. Tsai, D.A. Hammer, *Rheology of rat basophilic leukemia cells*, Annals of Biomediacl Engineering, **25**, 62-68 (1997).

[99] G. Lenormand, J.J. Fredberg, *Deformability, dynamics, and remodeling of cytoskeleton of the adherent living cell*, Biorheology, **43**, 1-30 (2006).

[100] P. Sollich, *Rheological constitutive equation for a model of soft glassy materials*, Physical Reviews, **58** (1998).

[101] B. Fabry, G.N. Maksym, J.P. Butler, M. Glogauer, D. Navajas, J.J. Fredberg, *Scaling the microrheology of living cells*, Physical Review Letters, **87** (2001).

[102] D. Stamenovic, N. Rosenblatt, M. Montoya-Zavala, B.D. Matthews, S. Hu, B. Suki, N. Wang, D.E. Ingber, *Rheological behavior of living cells is timescale-dependent*,Biophysical Journal, **93**, 39-41 (2007).

[103] G. Binnig, C.F. Quate, C. Gerber, *Atomic Force Microscopy*, Physical Review Letters, **56**, 930-933 (1986).

[104] D.J. Beebe, G.A. Mensing, G.M. Walker, *Physics and applications if microfluidics in biology*, Annual Review of Biomedical Engineering, **4**, 261-286 (2002).

[105] M.J. Lang, P.M. Fordyce, S.M. Block, *Combined optical trapping and single-molecule fluorescence*, Journal of Biology, **2** (2003).

[106] A.R. Bausch, W. Mueller, E. Sackmann, *Measurement of local viscoelasticity and forces in living cells by magnetic tweezers*, **76** (1999).

[107] D. Wirtz, *Particle-tracking microrheology of living cells: principles and applications*, Annual Review in Biophysics, **38**, 301-326 (2009).

[108] R.M. Hochmuth, *Micropipette aspiration of living cells*, Journal of Biomechanics, **33**, 15-22 (2000).

[109] M. Lekka, K. Gnanachandran, A. Kubiak, T. Zielinski, J. Zemla, *Traction force microscopy - Measuring the forces exerted by cells*, Micron, **150** (2021).

[110] M. Radmacher, *Studying the mechanics of cellular processes by atomic force microscopy*, Cell mechanics, **83**, 347-372 (2007).

[111] M. Lekka, P. Laidler, D. Gil, J. Lekki, Z. Stachura, A.Z. Hrynkiewicz, *Elasticity of normal and cancerous human bladder cells studied by scanning force microscopy*, European Biophysical Journal, **28**, 312-316 (1999).

[112] J. R. Ramos, J. Pabijan, R. Garcia and M. Lekka, *The softening of human bladder cancer cells happens at an early stage of the malignancy process*, Beilstein Journal of Nanotechnology, **5**, 447-457 (2014).

[113] E. Canetta, A. Riches, E. Borger, S. Harrington, K. Dholakia, A.K. Adya, *Discrimination of bladder cancer cells from normal urothelial cells with high specificity and sensitivity: Combined application of atomic force microscopy and modulated Raman spectroscopy*, Acta Biomaterialia, **10**, 2043-2055 (2014).

[114] M.Lekka, J. Pabijan, B. Orzechowska, *Morphological and mechanical stability of bladder cancer cells in response to substrate rigidity*, Biochimica et Biophysica Acta - General subjects, **1863**, 1006-1014 (2019).

[115] A.N. Ketene, E.M. Schmelza, P.C. Roberts, M. Agah, *The effects of cancer progression on the viscoelasticity of ovarian cell cytosketon structures*, Nanomedicine, **8**, 93-102 (2012).

[116] E. Evans, D. Berk, A. Leung, *Detachment of agglutinin-bonded red blood cells. I. Forces to rapture molecular-point attachments*, Biophysical Journal, **59**, 838-848 (1991).

[117] F. Guilak, W.R. Jones, H.P. Ting-Beall, G.M. Lee, *The deformation behavior and mechanical properties of chondrocytes in articular cartilage*, Osteoarthritis and Cartilage, **7**, 59-70 (1999).

[118] F. Merenda, J. Rohner, E. Lamothe, P. Pascoal, J.M. Fournier, R.P. Salathè, *Micro-optics for optical trapping in microfluidics*, Optical Trapping and Optical Micromanipulation, **4** (2007).

[119] W.R. Trickey, T. P. Vail, F. Guilak, *The role of the cytoskeleton in the viscoelastic properties of human articular chondrocytes*, Journal of Orthopedic Research, **22**, 131-139 (2004).

[120] H.J. Butt, M. Jaschke, *Calculation of thermal noise in atomic force microscopy*, Nanotechnology, **6** (1995)

[121] H.J. Butt, B. Cappella, M. Kappl, *Force measurements with the atomic force microscope: Technique, interpretation and applications*, Surface Science Reports, **59**, 1-152 (2005).

[122] H. Ghaednia, X. Wang, S. Saha, Y. Xu, A. Sharma, R.L. Jackson, *A Review of Elastic-Plastic Contact Mechanics*, Applied Mechanics Review, **69** (2017).

[123] H. Hertz, *On the contact of elastic solids*, Miscellaneous Papers, Chapter V, 146-162 (1896).

[124] H. Schillers et al., *Standardized Nanomechanical Atomic Force Microscopy Procedure (SNAP) for Measuring Soft and Biological Samples*, Scientific Reports, **7** (2017).

[125] J. Zemla, J. Bobrowska, A. Kubiak, T. Zielinski, J. Pabijan, K. Pogoda, P. Bobrowski, M. Lekka, *Indenting soft samples (hydrogels and cells) with cantilevers possessing various shapes of probing tip*, European Biophysics Journal, **49**, 485-495 (2020).

[126] M. Lekka, D. Gil, K. Pogoda, J. Dulin´ska-Litewka, R. Jach, J. Gostek, O. Klymenko, S. Prauzner-Bechcicki, Z. Stachura, J. Wiltowska-Zuber, K. Okon´d, P. Laidler, *Cancer cell detection in tissue sections using AFM*, Archives of Biochemistry and Biophysics, **518**, 151-156 (2012).

[127] Y.M. Efremov, T. Okajima, A. Raman, *Measuring viscoelasticity of soft biological samples using atomic force microsocpy*, Soft Matter, **16** (2020).

[128] Y. Abidine, V.M. Laurent, R. Michel, A. Duperray, C. Verdier, *Local mechanical properties of bladder cancer cells measured by AFM as a signature of metastatic potential*, The European Physical Journal - Plus, **130** (2015).

[129] Y. Abidine, A. Giannetti, J. Revilloud, V.M. Laurent, C. Verdier, *Viscoelastic Properties in Cancer: From Cells to Spheroids*, Cells, **10** (2021).

[130] M. Berardi, K. Bielawski, N. Rijnveld, G. Gruca, H. Aardema, L. V. Tol, G. Wuite, B. I. Akca, *Optical interferometry based micropipette aspiration provides real-time sub-nanometer spatial resolution*, Communications Biology, **4** (2021).

[131] E. H. Zhou, S. T. Quek, C. T. Lim, *Power-law rheology analysis of cells undergoing micropipette aspiration*, Biomechanics and Modeling in Mechanobiology, **9**, 563-572 (2010) .

[132] G. R. Plaza, T. Q. Uyeda, Z. Mirzaei, C. A. Simmons, *A study of the influence of actin-binding proteins using linear analyses of cell deformability*, Soft Matter, **11**, 5435-5446 (2015).

[133] H. Yamaguchi, J. Condeelis, *Regulation of the actin cytoskeleton in cancer cell migration and invasion*, Biochimica et Biophysuca Acta, **5** (2007).

[134] G. Weder, M. Hendriks-Balk, R. Smajda, D. Rimoldi, M. Liley, H. Heinzelmann, A. Meister, A. Mariotti, *Increased plasticity of the stiffness of melanoma cells correlates with their acquisition of metastatic properties*, Nanomedicine: Nanotechnology, Biology and Medicine, **10** (2014).

[135] R.K. Jain, J.D. Martin, T. Stylianopoulos, *The role of mechanical forces in tumor growth and therapy*, Annual Review of Biomedical Engineering, **16**, 321-346 (2014).

[136] G.F. Giancotti, *Deregulation of cell signaling in cancer*, FEBS Letters, **16** (2014).

[137] A.J. Ridley, M.A. Schwartz, K. Burridge, R.A. Firtel, M.H. Ginsberg, G. Borisy, J.T. Parsons, A.R. Horwitz, *Cell Migration: Integrating Signals from Front to Back*, Science, **302** (2003).

[138] A.M. Shannon, D.J. Bouchier-Hayes, C.M. Condron, D. Toomey, *Tumour hypoxia, chemotherapeutic resistance and hypoxia-related therapies*, Cancer Treatment Review, **29**, 297-307 (2003).

[139] C. Bernardo, C. Costa, C. Palmeira, R. Pinto-Leite, P. Oliveira, R. Freitas, F. Amado, L.L. Santos, *What we have learned from urinary bladder cancer models*, Journal of Cancer Metastasis and Treatment, **2**, 51-58 (2016).

[140] F.Rico, P. Roca-Cusachs, N. Gavara, R. Farrè, M. Rotger, D. Navajas, *Probing mechanical properties of living cells by atomic force microsocpy with blunted pyramidal cantilever tips*, Physical Review E, **72** (2005).

[141] E. Finot, A. Passian, T. Thundat, *Measurement of mechanical properties of cantilever shaped materials*, Sensors, **26**, 3497-3541 (2008).

[142] M.Lekka, K. Pogoda, J. Gostek, O. Klymenko, S. Prauzner-Bechcicki, J. Wiltowska-Zuber, J. Jaczewska, J. Lekki, Z. Stachura, *Cancer cell recognition-mechanical phenotype*, Micron, **43**, 1259-1266 (2012).

[143] C. Bonnas, J. Chou, Z. Werb, *Remodelling the extracellular matrix in development and disease*, Nature Reviews Molecular Cell Biology, **15**, 786-801 (2014).

[144] K.Gnanachandran, S. Kedracka-Krok, J. Pabijan, M. Lekka, *Discriminating bladder cancer cells through rheological mechanomarkers at cell and spheroid levels*, Journal of Biomechanics, **144** (2022).

[145] M.Lekka, *Discrimination Between Normal and Cancerous Cells Using AFM*, BioNanoScience, **6** (2016).

[146] A. Kubiak, M. Chighizola, C. Schulte, N. Bryniarska, J. Wesolowska, M. Pudelek, M. Lasota, D. Ryszawy, A. Basta-Kaim, P. Laidler, A. Podestà, M. Lekka, *Stiffening of DU145 prostate cancer cells driven by actin filaments-microtubule crosstalk conferring resistance to microtubule-targeting drugs*, Nanoscale, **12** (2021).

[147] T.L. Nguyen, E.R. Polanco, A.N. Patananan, T.A. Zangle, M.A. Teitell, *Cell viscoelasticity is linked to fluctuations in cell biomass distributions*, Scientific Reports, **10**, 7403 (2020)

[148] J. Rother, H. Nöding, I. Mey, A. Janshoff, *Atomic force microscopy-based microrheology reveals significant differences in the viscoelastic response between malign and benign cell lines*, Open Biology, **4** (2014).

[149] L.M. Rebelo, J.S. De Sousa, J. Mendes Filho, M. Radmacher, *Comparison of the viscoelastic properties of cells from different kidney cancer phenotypes measured with atomic force microscopy*, Nanotechnology, **24** (2013).

[150] A. Weber, J. Iturri, R. Benitez, J.L. Toca-Herrera, *Measuring biomaterials mechancis with atomic force microscopy. Influence of the loading rate*

and applied force (pyramidal tips), Microscopy research and technique, **82** (2019).

[151] Y.M. efremov, A.A. Dokrunova, D.V. Bagrov, K.S. Kudryashova, O.S. Sokolova, V. Shaitan, *The effects of confluency on cell mechanical properties*, Journal of Biomechanics, **46**, 1081-1087 (2013).

[152] S.Nawaz, P. Sanchez, K. Bodensiek, S. Li, M. simons, I.A.T. Schaap, *Cell visco-elasticity measured with AFM and optical Trapping at sub-micrometer deformations*, Plos One, **7** (2012).

[153] Y.M. Efremov, W.H. Wang, S.D. Hardy, E.L. Geahlen, A. Raman, *Measuring nanoscale viscoelastic parameters of cells directly from AFM force-displacement curves*, Scientific Reports, **7** (2017).

[154] M. Lekka, P. Laidler, J. J. Ignacak, M. Labd, J. Lekki, H. Struszczyk, Z. Stachura and A. Z. Hrynkiewicz, *The effect of chitosan on stiffness and glycolytic activity of human bladder cells*, Biochimica et Biophysica Acta - Molecular Cell Research, **1540**, 127-136 (2001).

[155] B. Sousa, J. Pereira, J. Paredes, *The Crosstalk Between Cell Adhesion and Cancer Metabolism*, International Journal of Molecular Science, **20** (2019).

[156] I. Smyrek, B. Mathew, S.C. Fischer, S. M. Lissek, S. Becker, E.H.K. Stelzer, *E-cadherin, actin, microtubules and FAK dominate different spheroid formation phases and important elements of tissue integrity*, Biology Open, **8** (2019).

[157] M. Lekka, D. Gil, W. Dabros, J. Jaczewska, A.J. Kulik, J. Lekki, Z. Stachura, J. Stachura, P. Laidler, *Characterization of N-cadherin unbinding properties in non-malignant (HCV29) and malignant (T24) bladder cells*, Journal of Molecular Recognition, **24**, 833-842 (2011).

[158] A.A. van der Wurff, S.J. Vermeulen, E.P. van der Linden, M.M. Mareel, F.T. Bosman, J.W. Arends, *Patterns of alpha- and beta-catenin and E-cadherin expression in colorectal adenomas and carcinomas*, The Journal of Pathology, **182**, 325-330 (1997).

[159] A.S. Nunes, A.S. Barros, E.C. Costa, A.F. Moreira, I.J. Correia, *3D tumor spheroids as in vitro models to mimic in vivo human solid tumors resistance to therapeutic drugs*, Biotechnology and Bioengineering, **116**, 206-226 (2019).

[160] Y. Li, X. Yang, L.J. Su, T.W. Flaig, *Pazopanib synergizes with docetaxel in the treatment of bladder cancer cells*, Urology, **78**, 7-13 (2011).

[161] F. Fabbri, S. Carloni, G. Brigliadori, W. Zoli, R. Lapalombella, M. Marini, *Sequential events of apoptosis involving docetaxel, a microtubule-interfering agent: A cytometric study*, BMC Cell Biology, **7**, 1-14 (2006).

[162] J.M. Northcott, I.S. Dean, J.K. Mouw, V.M. Weaver, *Feeling stress: The mechanics of cancer progression and aggression*, Frontiers in Cell and Development Biology, **6** (2018).

[163] J.M. Tse, G. Cheng, J.A. Tyrell, S.A. Wilcox-Adelman, Y. Boucher, R.K. Jain, L.L. Munn, *Mechanical compression drives cancer cells toward invasive phenotype*, PNAS U.S.A., **109**, 911-916 (2012).

[164] R.M. Megè, *Molecular basis for fluidization of cancer cells*, Nature Materials, **18**, 1147-1148 (2019).

[165] S. Grosser, J. Lippoldt, L. Oswald, M. Merkel, D.M. Sussman, F. Renner, P. Gottheil, E.W. Morawetz, T. Fuhs, X. Xie, S. Pawlizak, A.W. Fritsch, B. Wolf, L.C. Horn, S. Briest, B. Aktas, M.L. Manning, J.A. Kas, *Cell and Nucleues Shape an an Indicator of Tissue Fluidity in Carcinoma*, Physics Review X, **11** (2021).

[166] A. Rigato, A. Miyagi, S. Scheuring, F. Rico, *High-frequency microrheology reveals cytoskeleton dynamics in living cells*, Nature Physiscs, **13**, 771-775 (2017).

[167] C. Jùnior, M. Narciso, E. Marhuenda, I. Almendros, R. Farrè, D. Navajas, J. Otero, N. Gavara, *Baseline Stiffness Modulates the Non-Linear Response to Stretch of the Extracellular Matrix in Pulmonary Fibrosis*, International Joournal of Molecular Sciences, **23** (2021).

[168] V. Vyas, M. Solomon, G.G.M. D'Souza, B.D. Huey, *Nanomechanical Analysis of Extracellular Matrix and Cells in Multicellular Spheroids*, Cellular and Molecular Bioengineering, **12**, 203-214 (2019).

[169] G. Dechristè, J. Fehrenbach, E. Griseti, V. Lobjois, *Viscoelastic modeling of the fusion of multicellular tumor spheroids in growth phase*, Journal of Theoretical Biology, **454**, 102-109 (2018).

[170] M. Dolega, G. Zurlo, M. Le Goff, M. Greda, C. Verdier, J.F. Joanny, G. Cappello, P. Recho, *Mechanical behavior of multi-cellular spheroids under osmotic compression*, Journal of the Mechanics and Physics of Solids, **147** (2021).

[171] A. Giannetti, J. Revilloud, C. Verdier, *Mechanical properties of 3D tumor spheroids measured by AFM*, Computer Methods in Biomechanics and Biomedical Engineering, **23**, 125-127 (2020).

[172] D. Tsvirkun, J. Revilloud, A. Giannetti, C. Verdier, *The intriguing role of collagen on the rheology of cancer cell spheroids*, Journal of Biomechanics, **141** (2022).

[173] R.E. Hurst, C.D. Kamat, K.D. Kyker, D.E. Green, M.A. Ihnat, *A novel multidrug resistance phenotype of bladder tumor cells grown on Matrigel or SIS gel*, Cancer Letters, **217**, 171-180 (2005).

[174] J.A. Moibi, A.L. Mak, B. sun, R.B. Moore, *Urothelial cancer cell response to combination therapy of gemcitabine and TRAIL*, International Journal of Oncology, **39**, 61-71 (2011).

[175] A.M. Al-Abd, J.H. Lee, S.Y. Kim, N. Kun, H.J. Kuh, *Novel application of multicellular layers culture for in situ evaluation of cytotoxicity and penetration of paclitaxel*, Cancer Science, **99**, 423-431 (2008).

[176] P. Laidler, D. Gil, A. Pituch-Noworolska, D. Ciolczyk, D. Ksiazek, M. Przybylo, A. Litynska, *Expression of β1-integrins and N-cadherin in bladder cancer and melanoma cell lines*, Acta biochimica polonica, **47**, 1159-1170 (2000).

[177] C. Ringuette Goulet, G. Bernard, S. Chabaud, A. Couture, A. Langlois, B. Neveu, F. Pouliot, S. Bolduc, *Tissue-engineered human 3D model of bladder cancer for invasion study and drug discovery*, Biomaterial, **145**, 233-21 (2017).

[178] K. Guevorkian, M.J. Colbert, M. Durth, S. Dufour, F. Brochard-Wyart, *Aspiration of biological viscoelastic drops*, Physics Review Letters, **104** (2010).

[179] K. Guevorkian, D. Gonzalez-Rodriguez, C. Carlier, s. Dufour, F. Brochard-Wyart, *Mechanosensitive shivering of model tissues under controlled aspiration*, PNAS, **108**, 13387-13392 (2011).

[180] N. Baker, L.B. Boyette, R.S. Tuan, *Characterization of bone marrow-derived mesenchymal stem cells in aging*, Bone, **70**, 37-47 (2015).

[181] T.K. Berdyyeva, C.D. Woodworth, I. Sokolov, *Human epithelial cells increase their rigidity with ageing in vitro: Direct measurements*, Physics in Medicine and Biology, **50**, 81-92 (2005).

[182] S.C. Lieber, N. Aubry, J. Pain, G. Diaz, S.J. Kim, S.F. Vatner, *Aging increases stiffness of cardiac myocytes measured by atomic force microscopy nanoindentation*, American Journal of Physiology-Heart and Circulatory Physiology, **287**, 645-651 (2004).

[183] I. Dulinska-Molak, M. Pasilowska, K. Pogoda, M. Lewandowska, I. Eris, M.Lekka, *Age-related changes in the mechanical properties of human fibroblasts and its prospective reversal after anti-wrinkle tripeptide treatment*, International Journal of Peptide Research and Therapeutics, **20**, 77-85 (2014).

[184] C. Schulze, F. Wetzel, T. Kueper, A. Malsen, G. Muhr, s. Jaspers, T. Blatt, K.P. Wittern, H. Wenck, J.A. Kas, *Stiffening of human skin fibroblasts with age*, Biophysical Journal, **99**, 2434-2442 (2010).

[185] M.Zimmermann, C. Box, S.A. Eccles, *Two-dimensional vs. three-dimensional in vitro tumor migration and invasion assays*, Methods in Molecular Biology, **986**, 227-252 (2013).

[186] S.D. Baker, M. Zhao, C.K. Lee, J. Verweij, Y. Zabelina, J.R. Brahmer, A.C. Wolff, A. Sparreboom, M.A. Carducci, *Comparative pharmacokinetics of weekly and every-three-weeks docetaxel*, Cancer Research, **10**, 1976-1983 (2004).

[187] A.S. Mikhail, S. Eetezadi, C. Allen, *Multicellular Tumor Spheroids for Evaluation of Cytotoxicity and Tumor Growth Inhibitory Effects of Nanomedicines In Vitro: A Comparison of Docetaxel-Loaded Block Copolymer Micelles and Taxoter*, PlosOne, **8** (2013).

[188] A.H. Kyle, L.A. Huxham, D.M. Yeoman, A.I. Minchinton, *Limited tissue penetration of taxanes: a mechanism for resistance in solid tumors*, Clinical Cancer Research, **13**, 2804-2810 (2007).

[189] A. Kubiak, T. Zielinski, J. Pabijan, M. Lekka, *Nanomechanics in monitoring the effectiveness of drugs targeting the cancer cell cytoskeleton*, International Journal of Molecular Sciences, **21**, 1-15 (2020).

[190] O. Trèdan, C.M. Galmarini, K. Patel, I.F. Tannock, *Drug resistance and the solid tumor microenvironment*, Journal of the National Cancer Institute, **99**, 1441-1454 (2007).

[191] I.F. Tannock, C.M. Lee, J.K. Tunggal, D.D.M. Cowan, M.J. Egorin, *Limited penetration of anticancer drugs through tumor tissue: a potential cause of resistance of solid tumors to chemotherapy*, Clinical Cancer Research, **8**, 878-884 (2002).

[192] J.R. Masters, P.J. Hepburn, L. Walker, W.J. Highman, L.K. Trejdosiewicz, S. Povey, M. Parkar, B.T. Hill, P.R. Riddle, L.M. Franks, *Tissue culture model of transitional cell carcinoma: characterization of twenty-two human urothelial cell lines*, Cancer Research, **46**, 3630-3636 (1986).

List of Figures

The End